The Astrophysical Journal, 835:153 (37pp), 2017 February 1
doi:10.3847/1538-4357/835/2/153

Galaxy Environment in the 3D-*HST* Fields: Witnessing the Onset of Satellite Quenching at $z \sim 1$–2

M. Fossati[1,2], D. J. Wilman[1,2], J. T. Mendel[1,2], R. P. Saglia[1,2], A. Galametz[1,2], A. Beifiori[1,2], R. Bender[1,2], J. C. C. Chan[1,2], M. Fabricius[2], K. Bandara[2], G. B. Brammer[3], R. Davies[2], N. M. Förster Schreiber[2], R. Genzel[2,4,5], W. Hartley[6], S. K. Kulkarni[2], P. Lang[2], I. G. Momcheva[6], E. J. Nelson[2,7], R. Skelton[8], L. J. Tacconi[2], K. Tadaki[2], H. Übler[2], P. G. van Dokkum[7], E. Wisnioski[2], K. E. Whitaker[9,11], E. Wuyts[2], and S. Wuyts[10]

[1] Universitäts-Sternwarte München, Scheinerstrasse 1, D-81679 München, Germany; mfossati@mpe.mpg.de
[2] Max-Planck-Institut für Extraterrestriche Physik, Giessenbachstrasse, D-85748 Garching, Germany
[3] Space Telescope Science Institute, 3700 San Martin Drive, Baltimore, MD 21218, USA
[4] Department of Physics, Le Conte Hall, University of California, Berkeley, CA 94720, USA
[5] Department of Astronomy, Hearst Field Annex, University of California, Berkeley, CA 94720, USA
[6] Department of Physics & Astronomy, University College London, Gower Street, London, WC1E 6BT, UK
[7] Astronomy Department, Yale University, New Haven, CT 06511, USA
[8] South African Astronomical Observatory, P.O. Box 9, Observatory, Cape Town, 7935, South Africa
[9] Department of Astronomy, University of Massachusetts, Amherst, MA 01003, USA
[10] Department of Physics, University of Bath, Claverton Down, Bath, BA2 7AY, UK
Received 2016 September 5; revised 2016 November 16; accepted 2016 November 18; published 2017 January 24

Abstract

We make publicly available a catalog of calibrated environmental measures for galaxies in the five 3D-*Hubble Space Telescope* (*HST*)/CANDELS deep fields. Leveraging the spectroscopic and grism redshifts from the 3D-*HST* survey, multiwavelength photometry from CANDELS, and wider field public data for edge corrections, we derive densities in fixed apertures to characterize the environment of galaxies brighter than $JH_{140} < 24$ mag in the redshift range $0.5 < z < 3.0$. By linking observed galaxies to a mock sample, selected to reproduce the 3D-*HST* sample selection and redshift accuracy, each 3D-*HST* galaxy is assigned a probability density function of the host halo mass, and a probability that it is a central or a satellite galaxy. The same procedure is applied to a $z = 0$ sample selected from Sloan Digital Sky Survey. We compute the fraction of passive central and satellite galaxies as a function of stellar and halo mass, and redshift, and then derive the fraction of galaxies that were quenched by environment specific processes. Using the mock sample, we estimate that the timescale for satellite quenching is $t_{\rm quench} \sim 2$–5 Gyr; it is longer at lower stellar mass or lower redshift, but remarkably independent of halo mass. This indicates that, in the range of environments commonly found within the 3D-*HST* sample ($M_h \lesssim 10^{14}\,M_\odot$), satellites are quenched by exhaustion of their gas reservoir in the absence of cosmological accretion. We find that the quenching times can be separated into a delay phase, during which satellite galaxies behave similarly to centrals at fixed stellar mass, and a phase where the star formation rate drops rapidly ($\tau_f \sim 0.4$–0.6 Gyr), as shown previously at $z = 0$. We conclude that this scenario requires satellite galaxies to retain a large reservoir of multi-phase gas upon accretion, even at high redshift, and that this gas sustains star formation for the long quenching times observed.

Key words: galaxies: evolution – galaxies: star formation – galaxies: statistics – methods: statistical

1. Introduction

It has long been known that galaxies are shaped by the environment in which they reside. Works by, for example, Oemler (1974), Dressler (1980), and Balogh et al. (1997) showed that galaxies in high-density environments are preferentially red and early-type, compared to those in lower density regions. The more recent advent of large scale photometric and spectroscopic surveys confirmed with large statistics those early findings (Balogh et al. 2004; Kauffmann et al. 2004; Baldry et al. 2006). Meanwhile, space and ground-based missions have probed the geometry of our universe. Those observations coupled to cosmological models have built the solid Lambda cold dark matter (ΛCDM) framework (White & Rees 1978; Perlmutter et al. 1999), in which lower mass halos are the building blocks of more massive structures. One of the major tasks for modern studies of galaxy formation is therefore to understand how and when galaxy evolution is driven by internal processes or the evolving environment that each galaxy experiences during its lifetime. While internal mechanisms, including ejective feedback from supernovae or active galactic nuclei, are deemed responsible for suppressing star formation in all galaxies (Silk & Rees 1998; Hopkins et al. 2008), a galaxy can also directly interact with its environment when falling into a massive, gas- and galaxy-rich structure such as a galaxy cluster.

At low redshift detailed studies of poster child objects (Yagi et al. 2010; Fossati et al. 2012, 2016; Merluzzi et al. 2013; Fumagalli et al. 2014; Boselli et al. 2016), coupled with state-of-the-art models and simulations (Mastropietro et al. 2005; Kapferer et al. 2009; Tonnesen & Bryan 2010), have started to explore the rich physics governing those processes (e.g., Boselli & Gavazzi 2006, 2014; Blanton & Moustakas 2009, for reviews). Broadly speaking, they can be grouped into two classes. The first of them includes gravitational interactions between cluster or group members (Merritt 1983), or with the potential well of the halo as a whole (Byrd & Valtonen 1990), or their combined effect known as “galaxy harassment” (Moore

---

[11] Hubble Fellow.

et al. 1998). The second class includes hydrodynamical interactions between galaxies and the hot and dense gas that permeates massive halos. This class includes the rapid stripping of the cold gas via ram pressure as the galaxy passes through the hot gas medium (Gunn & Gott 1972). Ram pressure stripping is known to effectively and rapidly suppress star formation in cluster galaxies in the local universe (Solanes et al. 2001; Vollmer et al. 2001; Gavazzi et al. 2010; Boselli et al. 2008, 2014b; Gavazzi et al. 2013).

Less directly influencing the galaxy's current star formation, the multi-phase medium (e.g., warm, hot gas) associated to the galaxy (known as the "reservoir") should be easier to strip than the cold gas. Even easier, the filamentary accretion onto the galaxy from the surrounding cosmic web will be truncated as the galaxy is enveloped within the hot gas of a more massive halo (White & Frenk 1991). Both of these processes will suppress ongoing accretion onto the cold gas disk of the galaxy and lead to a more gradual suppression of star formation, variously labeled "strangulation" or "starvation" (e.g., Larson et al. 1980; Balogh et al. 1997). These processes are complicated in nature, and the exact details of their efficiency and dynamics are still poorly understood. The situation is even more complicated when several of these processes are found to act together (Gavazzi et al. 2001; Vollmer et al. 2005).

A different approach to disentangle the role of environment from the secular evolution is to study large samples of galaxies and correlate their properties (e.g., star formation activity) to internal properties (e.g., stellar mass) and environment. In the local universe, the advent of the Sloan Digital Sky Survey (SDSS) has revolutionized the field of large statistical studies and allowed for the effects of the environment on the galaxy population as a whole to be studied (Kauffmann et al. 2004; Baldry et al. 2006; Peng et al. 2010, 2012; Wetzel et al. 2012, 2013; Hirschmann et al. 2014). One of the main results is that environmental quenching is a separable process that acts on top of the internal processes that regulate the star formation activity of galaxies. A crucial parameter to understand the collective effect of the several environmental processes is the timescale over which the star formation activity is quenched. Several authors took advantage of excellent statistics to estimate the average timescale for environmental quenching, accounting for internal quenching processes, and found that in the low redshift universe this is generally long (~5–7 Gyr; McGee et al. 2009; De Lucia et al. 2012; Wetzel et al. 2013; Hirschmann et al. 2014), while possibly shorter in clusters of galaxies (~2–5 Gyr; Haines et al. 2015; Paccagnella et al. 2016) .

At higher redshift, the situation is made more complex due to the more limited availability of spectroscopic redshifts, which are paramount to depict an accurate picture of the environment. In the last decade, several ground-based redshift surveys started to address this issue (Wilman et al. 2005; Cooper et al. 2006). By exploiting the multiplexing of spectroscopic instruments at 8–10 meter class telescopes (e.g., VIMOS and GMOS, Lilly et al. 2007; Kurk et al. 2013; Balogh et al. 2014), these works showed that the environment plays a role in quenching the star formation activity of galaxies accreted onto massive halos (satellite galaxies) up to $z \sim 1$ (Muzzin et al. 2012; Quadri et al. 2012; Knobel et al. 2013; Kovač et al. 2014; Balogh et al. 2016), although the samples are limited to massive galaxies or a small number of objects.

Low-resolution space-based slitless spectroscopy is revolutionising this field, providing deep and highly complete spectroscopic samples. The largest of these efforts is the 3D-*Hubble Space Telescope* (*HST*) survey (Brammer et al. 2012) which, by combining a large area, deep grism observations, and a wealth of ancillary photometric data, provides accurate redshifts to $\Delta z/(1+z) \sim 0.003$ (Bezanson et al. 2016) for a large sample of objects down to low stellar masses ($\sim 10^9\,M_\odot$ and $\sim 10^{10}\,M_\odot$ at $z \sim 1$ and $z \sim 2$, respectively). The public release of their spectroscopic observations (Momcheva et al. 2016), in synergy with deep photometric observations (Skelton et al. 2014), has opened the way to an accurate quantification and calibration of the environment over the redshift range $z \sim 0.5$–3.

Another source of uncertainty in the interpretation of correlations of galaxy properties with environment is the inhomogeneity of methods used for different surveys (e.g., Haas et al. 2012; Muldrew et al. 2012; Etherington & Thomas 2015) and the lack of calibration of important parameters such as halo mass. In Fossati et al. (2015), we studied how to link a purely observational parameter space to physical quantities (e.g., halo mass, central/satellite status) by analyzing a stellar mass limited sample extracted from semi-analytic models of galaxy formation. To do so, we computed a projected density field in the simulation box, and we tested different definitions of density at different redshift accuracy. Our method is Bayesian in nature (galaxies have well-defined observational parameters, while the calibration into physical parameters is probabilistic). This approach is best suited to statistical studies where the application of selection functions and observational uncertainties can be fully taken into account.

In this paper, we extend this method to the 3D-*HST* survey by building up an environment catalog, which we make available to the community with this work.[12] We then explore the efficiency and timescales for quenching of satellite galaxies over cosmic time ($z \sim 0$–2) by combining the 3D-*HST* data at high redshift with SDSS data in the local universe in a homogeneous way. We also address the long-standing issue of impurity and contamination of the calibrated parameters (the fact that the observations do not perfectly constrain the halo mass of the parent halo for each galaxy or its central/satellite status) by recovering the "pure" trends using the mock sample as a benchmark.

The paper is structured as follows. In Section 2, we introduce the 3D-*HST* data set. In Section 3, we derive the local density for 3D-*HST* galaxies, including accurate edge corrections. Section 4 presents the range of environments in the 3D-*HST* area and how they compare to known galaxy structures from the literature. In Section 5, we introduce the mock galaxy sample and how we calibrate it to match the 3D-*HST* sample. We then link models and observations in Section 6, and assign physical quantities to observed galaxies. In Section 7, we study the quenching of satellite galaxies at $0 < z < 2.5$, and derive quenching efficiency and timescales. Lastly, we discuss the physical implications of our findings in Section 8 and summarize our work in Section 9.

All magnitudes are given in the AB system (Oke 1974), and we assume a flat ΛCDM universe with $\Omega_M = 0.3$, $\Omega_\Lambda = 0.7$, and $H_0 = 70\ \mathrm{km\,s^{-1}\,Mpc^{-1}}$, unless otherwise specified.

---

[12] http://dx.doi.org/10.5281/zenodo.168056

Throughout the paper, we use the notation $\log(x)$ for the base 10 logarithm of x.

2. The Observational Sample

In this work we aim at a quantification and calibration of the local environment for galaxies in the five CANDELS/3D-*HST* fields (Grogin et al. 2011; Koekemoer et al. 2011; Brammer et al. 2012)—namely, COSMOS, GOODS-S, GOODS-N, AEGIS, and UDS. The synergy of these two surveys represents the largest effort to obtain deep space-based near-infrared photometry and spectroscopy in those fields. For a description of the observations and reduction techniques, we refer the reader to Skelton et al. (2014) and Momcheva et al. (2016) for the photometry and spectroscopy, respectively. The CANDELS observations provide *HST*/WFC3 near-infrared imaging in the F125W and F160W filters (J_{125} and H_{160} hereafter) for all the fields, while 3D-*HST* followed up a large fraction of this area with the F140W filter (JH_{140} hereafter) and the WFC3/G141 grism for slitless spectroscopy. The novelty of this approach is to obtain low resolution ($R \sim 100$) spectroscopy for all the objects in the field. Taking advantage of the low background of the *HST* telescope, it is possible to reach a depth similar to traditional slit spectroscopy from 10 m class telescopes on Earth. Hereafter, we use the term "3D-*HST*" sample to refer to the combination of CANDELS and all the other space- and ground-based imaging data sets presented in Skelton et al. (2014), plus the grism spectroscopy of the 3D-*HST* program.

The 3D-*HST* photometric catalog (Skelton et al. 2014) used H_{160} or JH_{140} as detection bands, and its depth varies from field to field and across the same field due to the observing strategy of CANDELS. However, even in the shallowest portions of each field, the 90% depth confidence level is $H_{160} \sim 25$ mag. Beyond this magnitude limit, the star/galaxy classification (which is a key parameter for the environment quantification) becomes uncertain.

The 3D-*HST* spectroscopic release (Momcheva et al. 2016) provides reduced and extracted spectra down to[13] $JH_{\rm IR} = 26$ mag. The spectra are passed through the EAZY template fitting code (Brammer et al. 2008), along with the extensive ground- and space-based multiwavelength photometry. This results in "grism" redshifts, which are more accurate than photometric redshifts thanks to the wealth of stellar continuum and emission line features present in the spectra. However, only objects brighter than $JH_{\rm IR} = 24$ mag have been visually inspected, and have a `use_grism` flag that describes if the grism spectrum is used to compute the redshift. Incomplete masking of contaminating flux from nearby sources in the direction of the grism dispersion, residuals from spectra of bright stars, and corrupted photometric measurements can lead to this flag being set to 0 ("bad").

We include in the present analysis all galaxies brighter than $JH_{140} = 24$ mag, therefore limiting our footprint to the regions covered by grism and JH_{140} observations. We limit the redshift range to $0.5 < z < 3.0$. The lower limit roughly corresponds to the redshift, where the Hα line enters the grism coverage and the upper limit is chosen such that the number density of objects above the magnitude cut allows a reliable estimate of the environment. It also allows follow-up studies targeting the rest-frame optical features from ground-based facilities in the J, H, and K bands (e.g., KMOS, Sharples et al. 2013 and MOSFIRE, McLean et al. 2012).

We exclude stars by requiring `star_flag` to be 0 or 2 (galaxies or uncertain classification). We do not use the `use_phot` flag because it is too conservative for our goals. Indeed this flag requires a minimum of two exposures in the F125W and F160W filters, the object not being close to bright stars. The quantification of environment requires a catalog that is as complete as possible, even at the expense of more uncertain photometry (and photo-z) for the objects that do not meet those cuts. Nonetheless a $JH_{140} = 24$ mag cut allows a reliable star/galaxy separation for 99% of the objects and is at least 1 mag brighter than the minimum depth of the mosaics, thus alleviating the negative effects of nearby stars on faint sources. The final sample is made of 18,745 galaxies.

As a result of the analysis in Momcheva et al. (2016), each galaxy is assigned a "best" redshift. This is

1. A spectroscopic redshift from a ladder of sources, as described later.
2. A grism redshift if there is no spectroscopic redshift and `use_grism = 1`.
3. A pure photometric redshift if there is no spectroscopic redshift and `use_grism = 0`.

A `zbest_type` flag is assigned to each galaxy based on the conditions listed. The best redshift is the quantity used to compute the environment for each galaxy in the 3D-*HST* fields.

Spectroscopic redshifts are taken from the compilation of Skelton et al. (2014), which we complement with newer data. For the COSMOS field we include the final data release of the zCOSMOS bright survey (Lilly et al. 2007). We find 253 new sources, with reliable redshifts in the 3D-*HST*/COSMOS footprint mainly at $z < 1$. In COSMOS and GOODS-S, we include 95 objects from the DR1 (Tasca et al. 2016) of the VIMOS Ultra Deep Survey (VUDS; Le Fèvre et al. 2015). This survey mainly targets galaxies at $z > 2$, therefore complementing zCOSMOS. We include 105 redshifts from the MOSFIRE Deep Evolution Field Survey (MOSDEF; Kriek et al. 2015), which provides deep rest-frame optical spectra of galaxies selected from 3D-*HST*. For the UDS field, we also include 164 redshifts from VIMOS spectroscopy in a narrow slice of redshift ($0.6 < z < 0.7$; A. Galametz et al. 2016, in preparation) Lastly, we include 376 and 33 secure spectroscopic redshifts from KMOS$^{\rm 3D}$ (Wisnioski et al. 2015) and VIRIAL (Mendel et al. 2015), respectively. Those large surveys use the multiplexing capability of the integral field spectrometer KMOS on the ESO Very Large Telescope to follow-up 3D-*HST* selected objects. The former is a mass selected survey of emission line galaxies at $0.7 < z < 2.7$, while the latter observed passive massive galaxies at $1.5 < z < 2.0$.

In the selected sample, 20% of the galaxies have a spectroscopic redshift, 64% have a grism redshift, and only 16% have a pure photometric redshift. In the next section, we explore the accuracy of the grism and photometric redshifts as a function of the galaxy brightness and the signal-to-noise ratio (S/N) of emission lines in the spectra.

Stellar masses and stellar population parameters are estimated using the FAST code (Kriek et al. 2009), coupled with Bruzual & Charlot (2003) stellar population synthesis models. These models use a Chabrier (2003) initial mass

---

[13] The 3D-*HST* spectroscopic catalog is based on $JH_{\rm IR} = J_{125} + JH_{140} + H_{160}$ magnitudes. We therefore quote limits in this band when referring to their catalog. However, in this paper the sample selection is performed in JH_{140} to ensure that the footprint of our sample is entirely covered by G141 grism observations and direct imaging in F140W.

function (IMF) and solar metallicity. The best redshift is used for each galaxy, together with the available space- and ground-based photometry. The star formation history is parameterized by an exponentially declining function, and the Calzetti et al. (2000) dust attenuation law is adopted.

2.1. Redshift Accuracy

A careful quantification of the grism and photometric redshift accuracy is paramount for a good calibration of the environmental statistics into physically motivated halo masses. In Section 6, we will show how these masses are obtained from mock catalogs selected to match the number density and redshift uncertainty of 3D-*HST* galaxies.

The low-resolution spectra cover different spectral features as a function of galaxy properties and redshift. The most prominent features are emission lines, which are however limited to star-forming objects. On the other hand, stellar continuum features (Balmer break, absorption lines) are present in the spectra of all galaxies with an S/N that depends on the galaxy magnitude. Because all those features contribute to the redshift fitting procedure, we explore their impact on the redshift accuracy in bins of S/N of the strongest emission line in the spectrum and JH_{140} total magnitude. Given the limited spectral coverage of the G141 grism, it is common to find only one prominent emission line feature in the spectrum (Momcheva et al. 2016); this justifies our approach of using the S/N of the strongest line. We define the redshift accuracy ($\sigma_{v,\rm acc}$) as half the separation of the 16th and 84th confidence levels obtained from the probability density function (PDF) of grism redshifts, as derived from the EAZY template fitting procedure. In the case of fits obtained without including the spectral information, it becomes a pure photometric redshift uncertainty. A comparison of grism redshifts to spectroscopic redshifts shows that $\sim$800 km s^{-1} should be added to the formal uncertainty on the grism redshifts to obtain a scatter in $\Delta z/\sigma(z)$, with a 1σ width of unity. This "intrinsic grism" uncertainty can arise from morphological effects–that is, the light-weighted centroid of the gas emission can be offset from that of the stars (see Momcheva et al. 2016; Nelson et al. 2016). In this analysis, we added the intrinsic uncertainty of the grism data in quadrature to the formal uncertainty from the fitting process.

Figure 1 shows $\sigma_{v,\rm acc}$ for bins of emission line S/N and JH_{140} magnitude. The bottom right panel (f) shows the accuracy of photometric redshifts for the same sources, highlighting the significant improvement on the redshift quality when the spectra are included. From the top panels of Figure 1, it is clear how an emission line detection narrows the redshift PDF to the intrinsic uncertainty, irrespective of the stellar continuum features. At S/N, where the emission line becomes less dominant, we start to witness a magnitude dependence of the redshift accuracy. Brighter galaxies have better continuum detections and therefore a more accurate redshift. Even when there is no line detection (panel (e)), the typical redshift uncertainties are a factor 2 or 3 lower than pure photometric redshifts. The inclusion of the spectra helps the determination of the redshifts, even when the spectra are apparently featureless. The grism redshift accuracy is comparable to the pure photometric redshift accuracy only for the faintest objects ($JH_{140} > 23$ mag), with no emission line detection ($S/N < 2$), a population which accounts for $\sim$10% of our grism sample.

As a final note of caution, we highlight that whenever the information in the spectra is limited, the final grism redshift accuracy depends largely on the photometric data, whose availability depends on the field. Indeed, COSMOS and GOODS-S have been extensively observed with narrow or medium band filters (Taniguchi et al. 2007; Cardamone et al. 2010; Whitaker et al. 2011), resulting in better photometric redshifts compared to the other fields. However, as shown in Section 6, these field-to-field variations have negligible effects on our calibration of halo mass.

3. Quantification of the Environment

There are many ways to describe the environment in which a galaxy lives (e.g., Haas et al. 2012; Muldrew et al. 2012; Etherington & Thomas 2015). In this work, we apply to observational data the method we explored and calibrated in Fossati et al. (2015) and based on the work of Wilman et al. (2010). We use the number density of neighboring galaxies within fixed cylindrical apertures, because it is more sensitive to high overdensities, less biased by the viewing angle, more robust across cosmic times, and easier to physically interpret and calibrate than the *N*th nearest neighbor methods (Shattow et al. 2013).

3.1. Density

We consider all 3D-*HST* galaxies selected in Section 2 to be part both of the primary (galaxies for which the density is computed) and neighbor samples. We calculate the projected density $\Sigma_{r_{\rm ap}}$ in a combination of circular apertures centered on the primary galaxies with radii $r_{\rm ap}$. The apertures range from 0.25 to 1.00 Mpc in order to cover from intra-halo to super-halo scales.

For a given annulus defined by $r_{\rm ap}$, the projected density is given by

$$\Sigma_{r_{\rm ap}} = \frac{w_{r_{\rm ap}}}{\pi \times r_{\rm ap}^2}, \tag{1}$$

where $w_{r_{\rm ap}}$ is the sum of the weights of galaxies in the neighbor sample, falling at a projected distance on the sky $r < r_{\rm ap}$ from the primary galaxy and within a relative rest-frame velocity $\pm dv$. For the 3D-*HST* galaxies with a grism or spectroscopic redshift, the weights are set to unity (non-weighted sum), while for galaxies with pure photometric redshifts, we apply a statistical correction for the less accurate redshifts as described in Section 3.2. The primary galaxy is not included in the sum; therefore isolated galaxies have $\Sigma = 0$.

We set the velocity cut at $dv = 1500$ km s^{-1}. This value is deemed appropriate for surveys with complete spectroscopic redshift coverage (Muldrew et al. 2012) and for 3D-*HST*, given the quality of grism redshifts shown in Figure 1. A small value of dv avoids the peaks in the environmental density to be smoothed by interlopers in projection along the redshift axis. On the other hand, if only less accurate redshifts are available, a larger cut must be used to collect all the signal from overdense regions, which is artificially dispersed along the redshift axis (Etherington & Thomas 2015; Fossati et al. 2015).

Because the mean number density changes continuously with redshift, it is not possible to compare the local density (Σ) across time. Instead we define a relative overdensity δ, which is

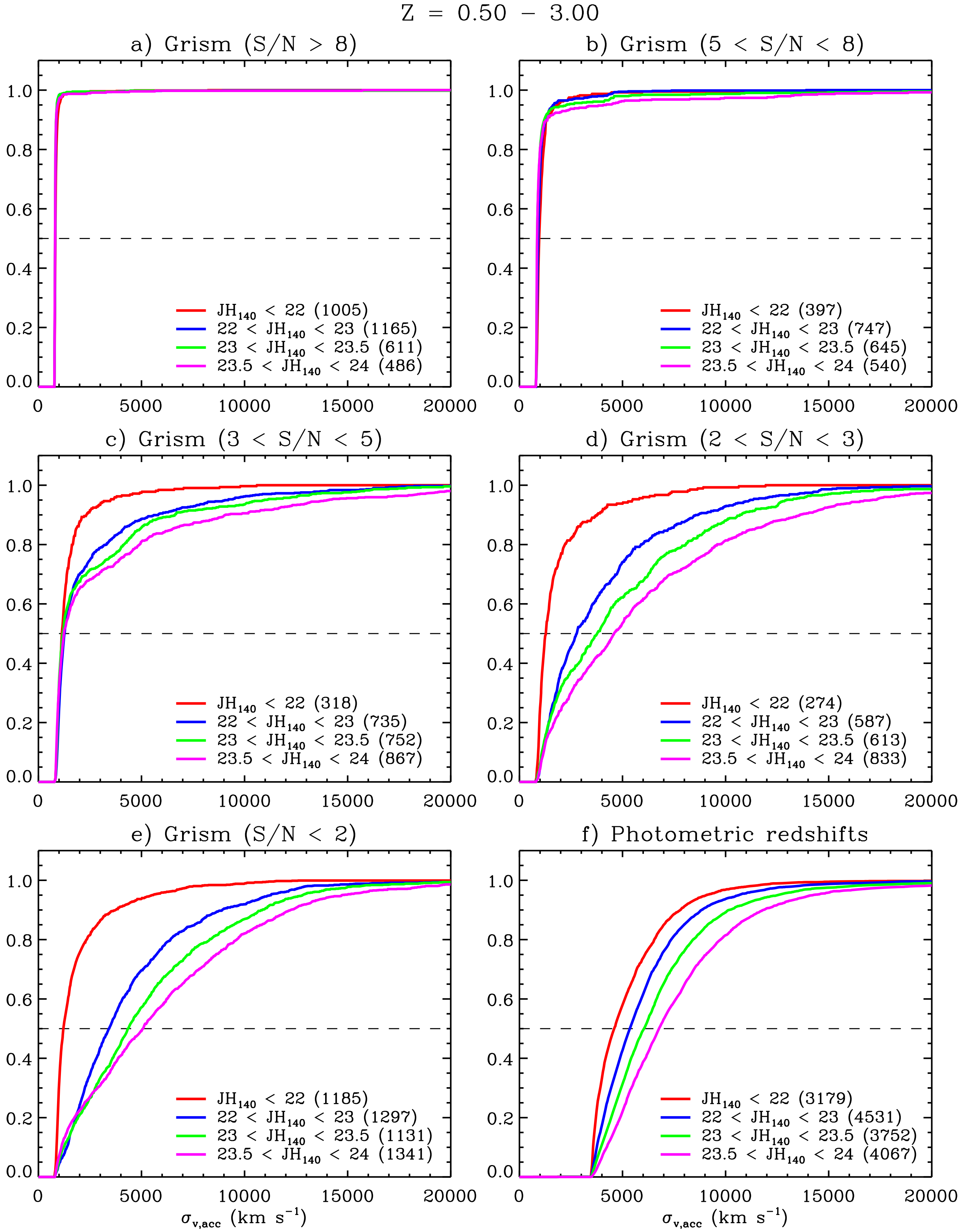

Figure 1. Cumulative distributions of the redshift accuracy ($\sigma_{v,\mathrm{acc}}$ in km s^{-1}) for galaxies at $0.5 < z < 3.0$ and $JH_{140} < 24$ mag. Panels from (a) to (e) are for grism redshifts in bins of S/N of the strongest emission line in the spectra. In each panel the different lines are for different bins of JH_{140} total magnitude. The panel (f) is for pure photometric redshifts (including galaxies that have grism redshifts).

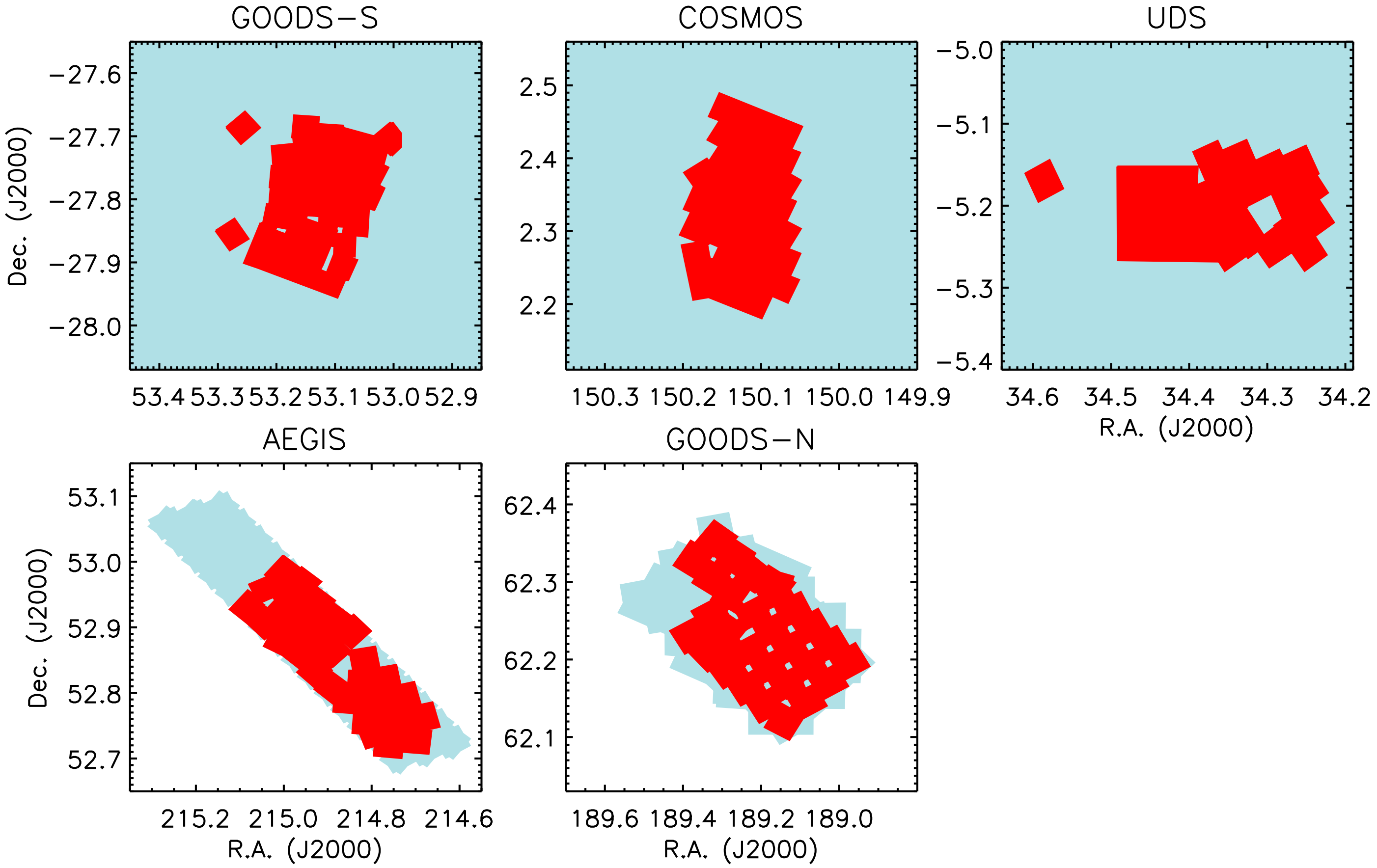

Figure 2. Footprints of the 3D-*HST* grism observations (red areas) in the five fields studied in this work and of the extended area catalogs (blue areas) used for the edge corrections. White areas have no photometric coverage.

given by

$$\delta r_{\rm ap} = \frac{\Sigma_{r_{\rm ap}} - \Sigma_{\rm mean}(z)}{\Sigma_{\rm mean}(z)}, \tag{2}$$

where $\Sigma_{\rm mean}(z)$ is the average surface density of galaxies at a given redshift. This is obtained by computing the volume density of galaxies (per Mpc^3) in the whole survey and parameterizing the redshift dependence with a third degree polynomial. This value is multiplied by the depth of the cylindrical aperture at redshift z to obtain the surface density $\Sigma_{\rm mean}(z)$. Throughout the paper, we will mainly use the overdensity in terms of the logarithmic density contrast defined as $\log(1 + \delta r_{\rm ap})$.

3.2. Edge Corrections

The calculation of the environment of primary galaxies at the edges of the 3D-*HST* footprint (see Figure 2, red areas) suffers from incomplete coverage of neighbors that results in an underestimated density in the considered aperture. In large scale surveys (e.g., SDSS, Wilman et al. 2010), it is common practice to remove galaxies too close to the edges of the observed field. In the case of deep fields, however, the observed area is relatively small, and the removal of such galaxies would reduce total number of objects significantly. One possible solution is to normalize the densities by the area of the circular aperture, which is within the survey footprint in Equation (1). Although this is a simple choice, it assumes a constant density field and neglects possible overdense structures just beyond the observed field. A more accurate solution consists of building up galaxy catalogs for a more extended area than 3D-*HST* and then using galaxies within these areas as “pure neighbors” for the environment of the primary 3D-*HST* galaxies. Given the amount of publicly available data, this is possible in GOODS-S, COSMOS, and UDS (see Figure 2, blue areas). In Appendix A we describe the data, depth, and redshift quality of the catalogs we built in those fields. Here we present the edge correction method we developed and how it was tuned to perform the edge corrections in the other two fields, GOODS-N and AEGIS.

3.2.1. Edge Correction Method for GOODS-S, COSMOS, and UDS

The availability of spectroscopic redshifts in the extended area catalogs is limited (from ∼5% in COSMOS and UDS to ∼15% in GOODS-S). We thus need to deal with the limited accuracy of photometric redshifts for the galaxies in those fields. The photo-z accuracy, which varies from field to field and depends on the redshift, brightness, and color of the objects (Bezanson et al. 2016), is such that most of the sources which are part of the same halo in real space would not be counted as neighbors of a primary galaxy, simply due to the redshift uncertainty. Fossati et al. (2015) show that increasing the depth of the velocity window would recover most of the real neighbors but at the expense of a larger fraction of interlopers (galaxies which are not physically associated to the primary). Thus we exploit a different method here. We assume that galaxies that are at small angular separation and whose redshifts are consistent within the uncertainties are, with a

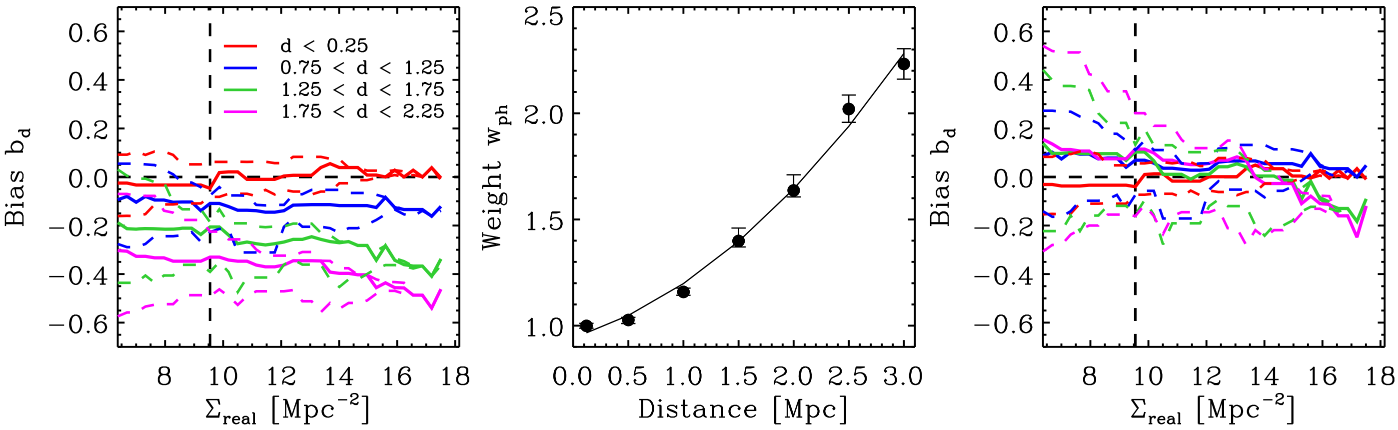

Figure 3. Left panel: median bias b_d in the density field introduced when photo-*z* are replaced with spectroscopic redshifts of sources at $d < 0.25$ Mpc (red), $d \sim 1.0$ Mpc (blue), $d \sim 1.5$ Mpc (green), and $d \sim 2.0$ Mpc (magenta). Dashed lines mark the 10th–90th percentiles of the distributions. The vertical dashed line marks the density above which the bias is computed and converted into a weight. Middle panel: median weight as a function of the distance of the neighbor with a spectroscopic (or grism) redshift. The solid line is the best fit quadratic polynomial we use for the statistical correction (see Equation (4)). Right panel: median bias b_d after the statistical correction, color coded as in the left panel. The median values are consistent with no bias for all the distance bins.

high probability, physically associated (e.g., Kovač et al. 2010; Cucciati et al. 2014). If one of them has a secure spectroscopic redshift, we assign this to the others.

Our method works as follows:

1. For each galaxy with a photometric redshift, we select all neighbors with a redshift within $dv_{\rm phot} = \pm 10.000$ km s^{-1}. This value is chosen to recover most of the real neighbors, given the average photo-*z* uncertainties.
2. Among those neighbors, we select the closest (in spatial coordinates) that has a secure spectroscopic (or grism) redshift. Here we assume grism redshifts to have a negligible uncertainty compared to photo-*z*.
3. We replace the photo-*z* of the galaxy of interest with this spec-*z* (or grism-*z*). Since the statistical validity of the assumption of physical association depends on the distance of the neighbor, for increasing distances we underestimate the true clustering. We correct for the bias by assigning a weight w_{ph} to each galaxy.

The weight is evaluated on a training sample made of galaxies in 3D-*HST* with $JH_{140} < 23$ mag. For each galaxy in the three fields, we compute the "real" density ($\Sigma_{\rm real}$ in a 0.75 Mpc radius and $dv = \pm 1500$ km s^{-1}) using spec-*z* or grism-*z* from 3D-*HST*. We then take for each galaxy its photometric redshift, and follow the procedure described previously, but instead of choosing the closest neighbor with a secure redshift, we select a random neighbor in different bins of projected sky distance (from 0 to 3 Mpc in bins of 0.5 Mpc width). Then we compute densities, with each of these distance replacements separately and the fractional bias (b_d) as

$$b_d = \frac{\Sigma_d - \Sigma_{\rm real}}{\Sigma_{\rm real}}, \tag{3}$$

where the *d* subscript denotes the replacement with a spec-*z* of a galaxy found at distance *d*. By using the 3D-*HST* data, we make sure that there are always a large number of neighbors with a secure redshift, and we repeat this procedure a thousand times in order to uniformly sample the neighbors. Figure 3, left panel, shows b_d as a function of the real density in four bins of *d*. Clearly, the larger *d* is, the more underestimated the real density will be, due to a decreasing fraction of correct redshift assignments.

We then derive the median weight $w_{ph,d} = {\rm med}((b_d + 1)^{-1})$, where the median is computed among all galaxies that have $\Sigma_{\rm real} > 9.5$ Mpc^{-2} (see the vertical dashed line in Figure 3, left panel). The density dependence of b_d is negligible at these densities; therefore, by avoiding underdense regions (where the uncertainty on b_d is large), we obtain a robust determination of $w_{ph,d}$. Figure 3, middle panel, shows $w_{ph,d}$ versus *d*, which we fit with a quadratic relation, obtaining

$$w_{ph,d} = 9.66 \times 10^{-2} \times d^2 + 0.155 \times d + 0.946, \tag{4}$$

with the additional constraint that $w_{ph,d} \geqslant 1$, which corresponds to $w_{ph,d} = 1$ for $d < 0.29$ Mpc. We tested that this relation, although obtained combining all fields, holds within the uncertainties when each field is considered separately. Lastly we show in Figure 3, right panel, how the systematic bias is removed when the weight is applied to all neighbors when computing the density. This is consistent with no bias within the uncertainties for all the distance bins.

3.2.2. Edge Correction Method for GOODS-N and AEGIS

The GOODS-N and AEGIS fields do not have deep and extended near-infrared public catalogs that can be used to derive the edge corrections as presented previously. As shown in Figure 2 (light blue shaded areas), the 3D-*HST*/CANDELS footprint slightly extends beyond the area covered by G141 grism observations (the main requirement for our primary sample). Therefore the 3D-*HST*/CANDELS catalog itself can be used to perform edge corrections. We derive JH_{140} magnitudes from the J_{125} magnitudes using a linear function derived from the five 3D-*HST* fields ($JH_{140} = 1.000 \times J_{125} - 0.295$). We then use 3D-*HST* photometric redshifts (or spec-*z*, where available) and apply the method described in Section 3.2.1.

However, the 3D-*HST*/CANDELS photometric catalogs do not extend enough beyond the primary sample area to ensure the apertures used to compute the density are entirely covered by the photometric catalog footprint. For this reason, we compute the densities using the area of the circular aperture within the photometric catalog. We test this method by comparing the density ($\Sigma_{\rm real}$) in a 0.75 Mpc aperture measured

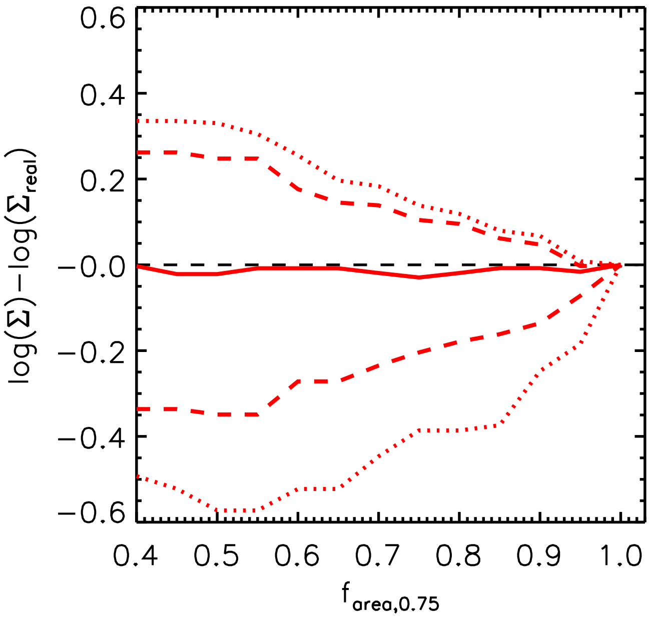

Figure 4. Logarithmic offset between the density ($\Sigma_{\rm real}$) in a 0.75 Mpc aperture measured using the extended catalogs for COSMOS, GOODS-S, UDS, and the density (Σ) measured using the fraction of the aperture in the 3D-*HST* footprint ($f_{\rm area,0.75}$) as a function of the latter quantity. The solid line is the median, while dashed and dotted lines mark the 1σ and 2σ confidence intervals, respectively. The offset between the two methods is zero, with a scatter that increases with decreasing fraction of the aperture in the 3D-*HST* footprint.

using the extended catalogs for COSMOS, GOODS-S, UDS, and the density (Σ) measured correcting for the fraction of the aperture ($f_{\rm area,0.75}$) in the 3D-*HST*/CANDELS footprint. The result is shown in Figure 4. We note that although the median (red solid line) is consistent with no bias, the area correction introduces a scatter (dotted and dashed lines), which increases by decreasing the fraction of the aperture in the footprint.

In conclusion, the environment catalog released with this work includes all the primary galaxies in the five 3D-*HST* fields. The structure of the catalog is described in Appendix E. However, in the rest of this work, we only include galaxies for which $f_{\rm area,0.75} > 0.9$ for the GOODS-N and AEGIS fields. The total number of objects in the primary 3D-*HST* sample with a robust determination of the environmental density is therefore reduced to 17,397 (93% of the original sample).

4. Overdensities in the 3D-*HST* Deep Fields

In order to explore correlations of galaxy evolution with environment, we need to make sure the 3D-*HST* fields span a wide range of galaxy (over)densities, and use known structures for a "sanity check" of our density estimates. Figures 5–8 and 9 present the primary sample of 3D-*HST* galaxies in the five fields color coded by their overdensity in the 0.75 Mpc aperture in different redshift slices. This aperture corresponds to the typical virial radius of massive halos ($M_h > 10^{13.5}\,M_\odot$) in the redshift range under study. The range of density probed is wide and spans from isolated galaxies to objects for which the local number of neighbors is up to ten times larger than the mean at that redshift, reaching the regime of clusters or massive groups.

In each figure, we overplot the position and extent of X-ray extended emission from the hot intragroup (and intracluster) medium that fills massive halos. The exquisite depth of X-ray data in the deep fields (Finoguenov et al. 2007, 2010, 2015; Erfanianfar et al. 2013) allows the detection of the hot gas from halos down to $M_h \sim 10^{13}\,M_\odot$. We find a very satisfactory agreement between our overdensities and the X-ray emission position. Indeed, most of the X-ray groups are coincident with large overdensities in our maps. On the other hand, not all the overdense structures identified in our work are detected in the X-ray. We speculate this is mainly due to the presence of more than one massive structure along the line of sight, or that low mass groups may not yet be virialized. Lastly, we note that the redshift of the X-ray emission is assigned based on the photometric or spectroscopic information available at the epoch of the publication of the catalog; these data might not have been as accurate as the density field reconstruction performed in this work. Our analysis therefore has the potential to spectroscopically confirm more X-ray groups and improve the quality of previous redshift assignments.

Several other works have also analyzed, with different techniques, the presence of overdense structures in deep fields. We overplot on Figure 5 the position of overdensities found in the GOODS-S field by Salimbeni et al. (2009). These have been derived from the GOODS-MUSIC catalog using a smoothed 3D density searching algorithm. These data have 15% spectroscopic redshifts and photometric redshifts for the remaining fraction. Because the smoothing technique is less able to constrain the size of the structure, we plot circles with an arbitrary radius. The structures within the 3D-*HST* footprint (except those at $z > 2$) are confirmed with our data to be at least a factor of 2–3 denser than the mean. The differences in samples and techniques hamper a more quantitative comparison. Our data confirm with a high degree of significance the detection of two well known super-structures, one at redshift $z = 0.73$ (Gilli et al. 2003; Adami et al. 2005; Trevese et al. 2007) and one at redshift $z = 1.61$, first detected by Kurk et al. (2009). The latter is made of five peaks in the photo-z map (which correspond to putative positions for the X-ray emission; see Table 1 in Finoguenov et al. 2015). The main structure is robustly recovered by our analysis, while the other substructures are only mild ($\log(1+\delta_{0.75}) \sim 0.5$) overdensities.

In the COSMOS field (see Figure 6), Scoville et al. (2007) applied an adaptive smoothing technique (similar to Salimbeni et al. 2009) to find large scale structures at $z < 1$. While their results do not constrain the size of the structure and are less sensitive to very compact overdensities, we do find that their detections in the 3D-*HST* footprint correspond to high overdensities in our work.

Similarly in the UDS field, we do detect a very massive cluster surrounded by filaments and less massive groups (upper left panel of Figure 7) at $z = 0.65$ (Galametz et al. 2016, in preparation). Another well known structure in this field is located at $z = 1.62$ (Papovich et al. 2010; Tanaka et al. 2010). Despite being only partially covered by the 3D-*HST* grism observations (isolated pointing on the left of the contiguous field), we do find it corresponds to a large overdensity of galaxies, thanks to our accurate edge corrections using UKIDSS UDS photometric data.

In summary, our reconstruction of the density field in the 3D-*HST* deep fields recovers the previously known massive structures across the full redshift range analyzed in this work.

5. The Model Galaxy Sample

The goal of this work is to understand the environment of galaxies in the context of a hierarchical universe. To reach this goal, we need to calibrate physically motivated quantities using

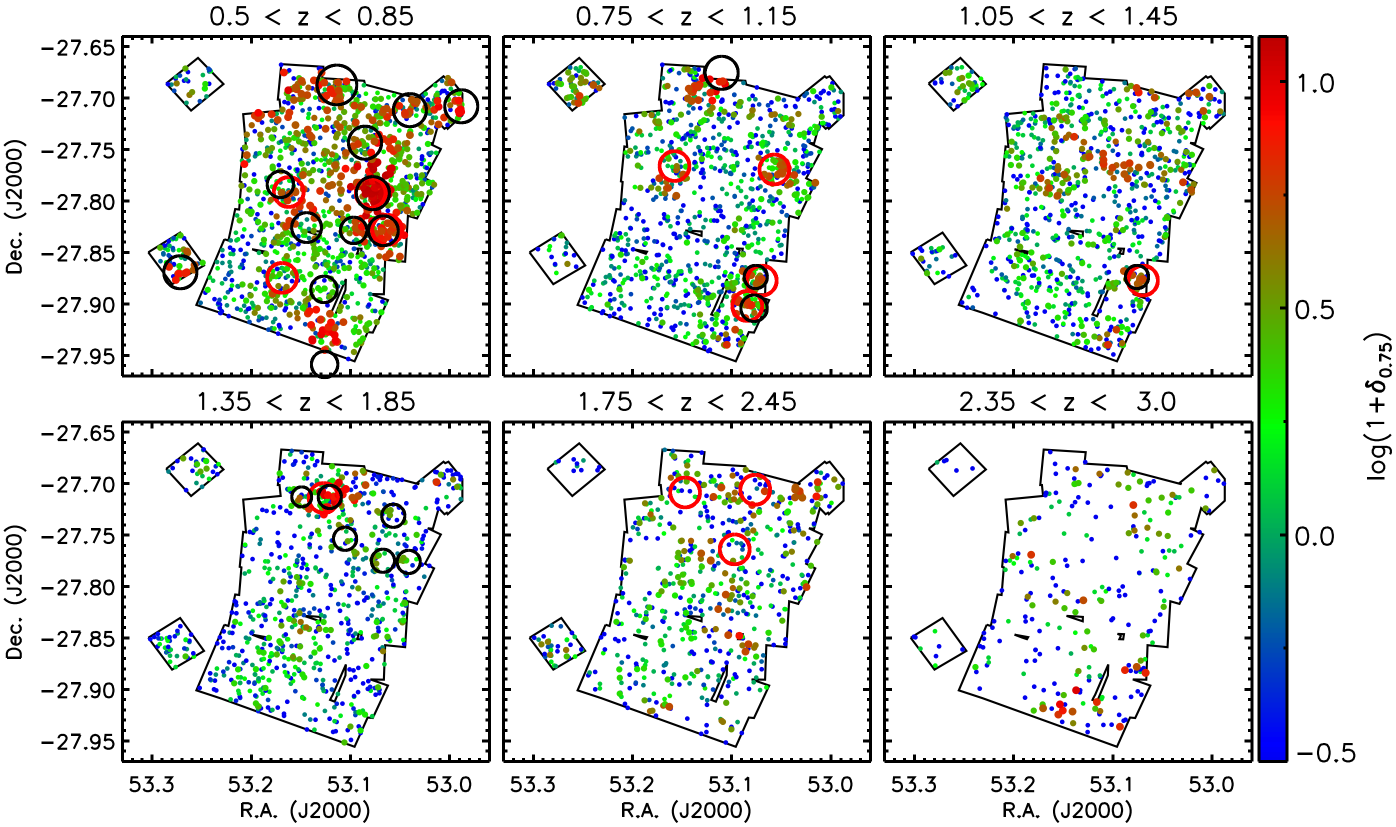

Figure 5. Gallery of the 3D-*HST* galaxies in the GOODS-S field in different redshift slices. Points are color coded by their overdensity in a 0.75 Mpc aperture. The size of the points also scales with overdensity. This figure demonstrates the large dynamic range in environments found in the CANDELS deep fields. Black circles mark the position of the X-ray extended emission from Finoguenov et al. (2015), and the size of the circle representing the extension of the emission (R_{200}). Red circles mark the position of galaxy overdensities from Salimbeni et al. (2009), who used a smoothed 3D density technique from the GOODS-MUSIC catalog to search for overdensities (the size of the circle is arbitrary and fixed).

observed metrics of environment by means of semi-analytic models (SAM) of galaxy formation. We make use of light cones from the latest release of the Munich model presented by Henriques et al. (2015). This model is based on the Millennium *N*-body simulation (Springel et al. 2005), which has a size of $500h^{-1}$ Mpc. The simulation outputs are scaled to cosmological initial conditions from the *Planck* mission (Planck Collaboration XVI; Planck Collaboration et al. 2014): $\sigma_8 = 0.829$, $H_0 = 67.3$ km s^{-1} Mpc^{-1}, $\Omega_\Lambda = 0.685$, $\Omega_M = 0.315$. Although these values are slightly different from those used in our observational sample, the differences in cosmological parameters have a much smaller effect on mock galaxy properties than the uncertainties in galaxy formation physics (Wang et al. 2008; Fontanot et al. 2012; Guo et al. 2013a).

This model includes prescriptions for gas cooling, size evolution, star formation, stellar and active galactic nuclei feedback, and metal enrichment, as described by, for example, Croton et al. (2006), De Lucia & Blaizot (2007), and Guo et al. (2011). The most significant updates concern the reincorporation timescales of galactic wind ejecta that, together with other tweaks in the free parameters, reproduce observational data on the abundance and color distributions of galaxies from $z = 0$ to $z = 3$ (Henriques et al. 2015). Our choice of this model is therefore driven by those new features that are critical for an accurate quantification of the environment.

We make use of the model in the form of 24 light cones, which are constructed by replicating the simulation box evaluated at multiple redshift snapshots. Before deriving the density for the light cones, as described in Section 3.1, we first match the magnitude selection and redshift accuracy of the 3D-*HST* survey.

5.1. Sample Selection

SAMs are based on *N*-body dark-matter-only simulations. Therefore (and opposite to observations), the galaxy stellar masses are accurate quantities, while observed magnitudes are uncertain and rely on radiative transfer and dust absorption recipes implemented in the models. On the other hand, magnitudes are direct observables in a survey (like 3D-*HST*) are therefore known with a high degree of accuracy.

To overcome these limitations and the fact that JH_{140} magnitudes are not given in Henriques et al. (2015) cones, we employ a method that generates observed magnitudes for SAM galaxies by using observational constraints from 3D-*HST*. Each model galaxy is defined by its stellar mass ($M_{*,\rm mod}$), $U - V$ rest-frame color ($(U - V)_{\rm mod}$), and redshift ($z_{\rm mod}$). Similarly, 3D-*HST* galaxies are defined by stellar mass ($M_{*,\rm obs}$), $U - V$ rest-frame color ($(U - V)_{\rm obs}$), redshift ($z_{\rm obs}$), and magnitude ($JH_{\rm obs}$). The method works as follows:

1. For each bin of stellar mass (0.25 dex wide) and redshift (0.1 wide), we select all the model and 3D-*HST* galaxies.
2. For each model galaxy in this bin, we rank the $(U - V)_{\rm mod}$ and we find the $(U - V)_{\rm obs}$ that corresponds to the same ranking.

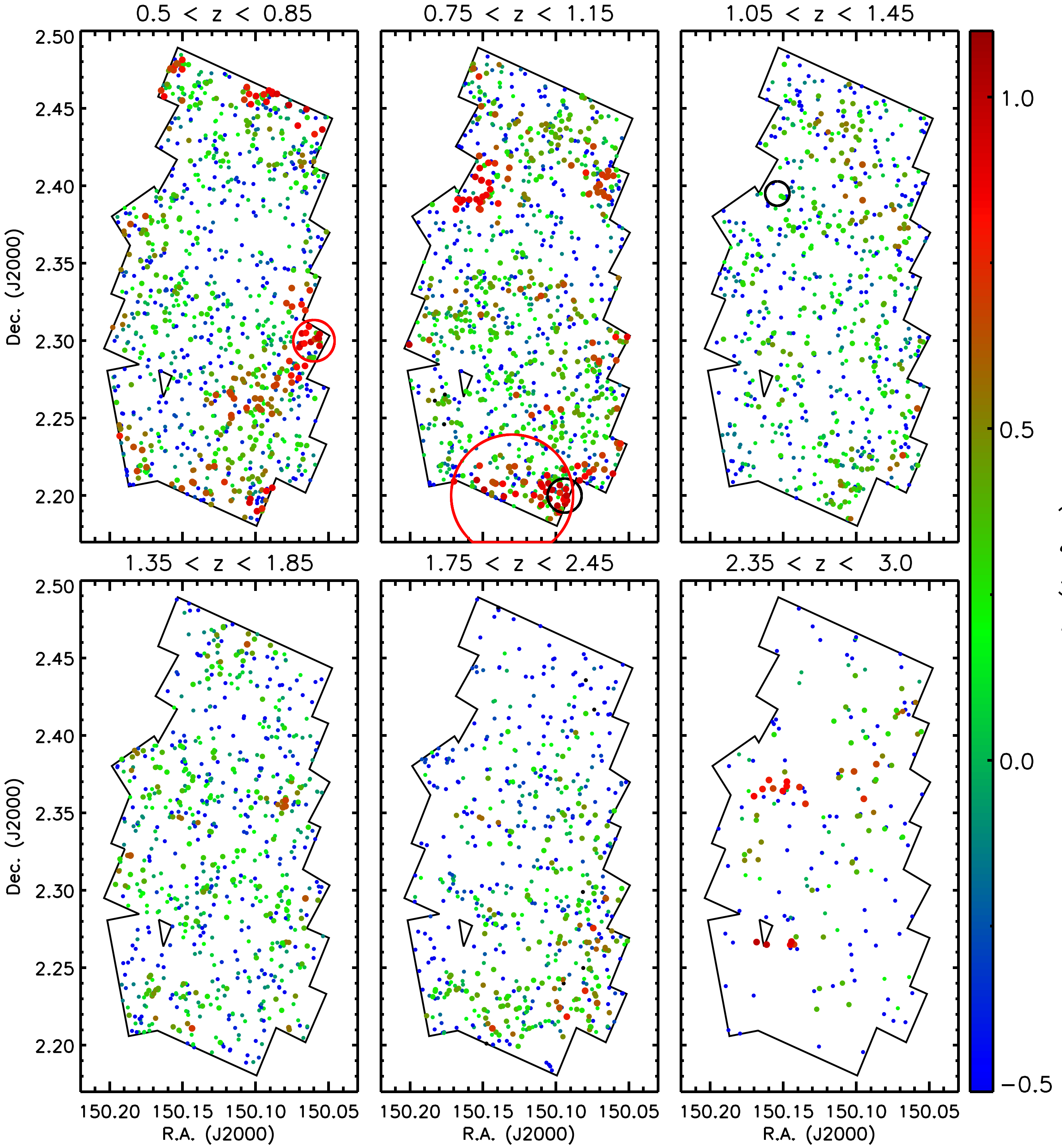

Figure 6. Same as Figure 5, but for the 3D-*HST* COSMOS field. The X-ray extended emission circles (black) are from Finoguenov et al. (2007), and galaxy density based large scale structures (red) are from Scoville et al. (2007), using pure photometric redshifts up to $z \sim 1$.

3. We assign to the model galaxy a randomly selected stellar mass-to-light ratio $(M_*/L_{JH})_{\rm obs}$ at $(U-V)_{\rm obs} \pm 0.05$, drawn from the distribution of 3D-*HST* galaxies in the stellar mass and redshift bin of the mock galaxy of interest.
4. From $(M_*/L_{JH})_{\rm obs}$, $M_{*,\rm mod}$, and $z_{\rm mod}$, we compute $JH_{\rm mod}$ for the model galaxy.

This method generates JH_{140} magnitudes for all the model galaxies down to $10^8\,M_\odot$. This is much deeper than the 3D-*HST* magnitude limit, even at the lower end of our redshift range. We then select model galaxies down to a $JH_{\rm mod,lim}$ magnitude that matches the total number density of the primary targets ($JH_{140} < 24$ mag) in the five 3D-*HST* fields to that in the 24 light cones. This protects us from stellar mass function

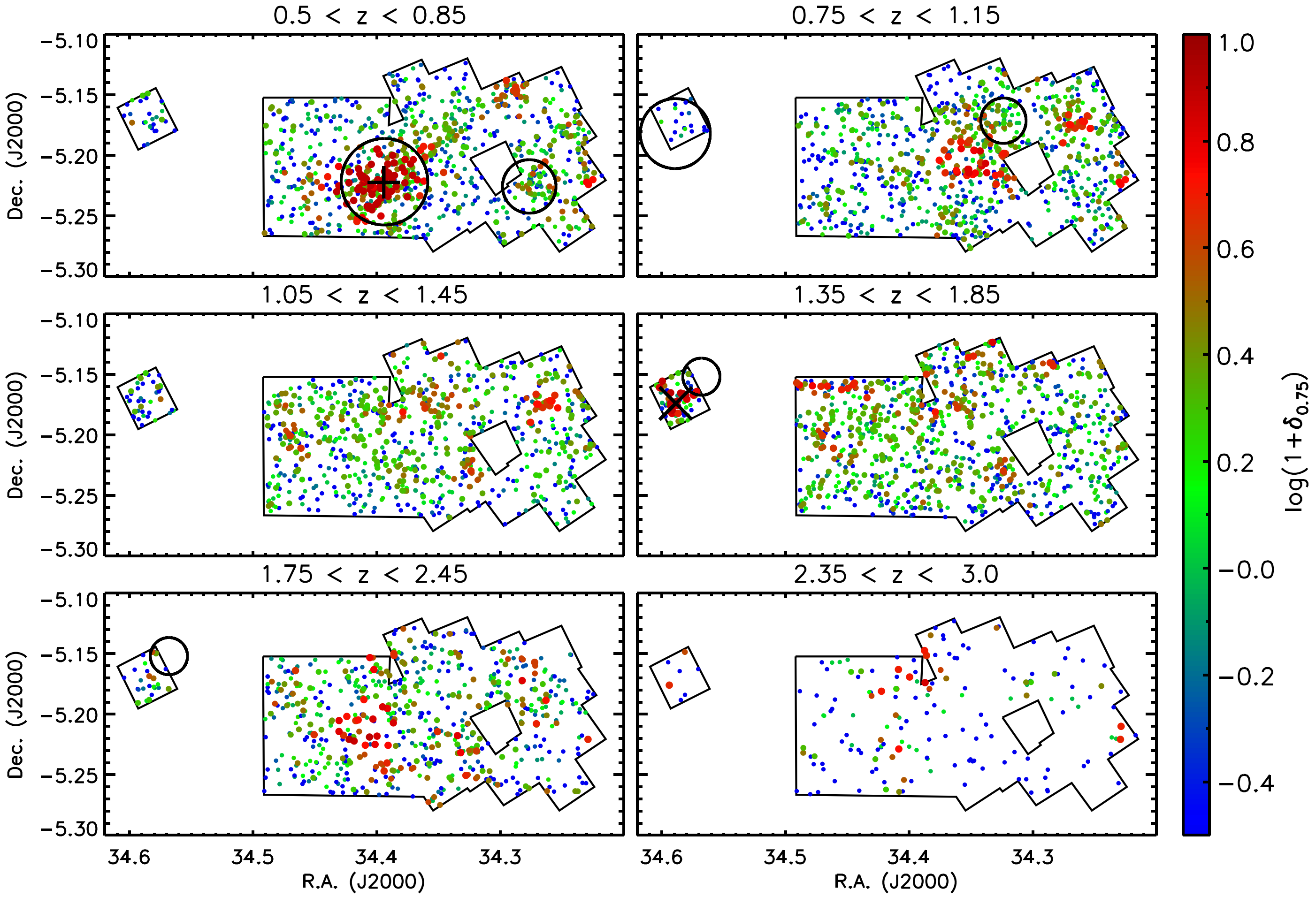

Figure 7. Same as Figure 5 but for the 3D-*HST* UDS field. The X-ray extended emission circles (black) are from Finoguenov et al. (2010). The black + and × symbols mark the center of known clusters at $z = 0.65$ (Geach et al. 2007; A. Galametz et al. 2016, in preparation) and $z = 1.62$ (Papovich et al. 2010; Tanaka et al. 2010), respectively.

mismatches between the models and the observations (although those differences are very small in Henriques et al. 2015). We employ a $JH_{\rm mod,lim} = 23.85$ mag, which is very close to 24 mag, further supporting the quality of the stellar mass functions in the models.

5.2. Matching the Redshift Accuracy

After the model sample is selected, the next goal is to assign to each galaxy a redshift accuracy that matches as closely as possible to the one in 3D-*HST*. To do so, we should not only assign the correct fraction of spec-z, grism-z, and photo-z as a function of observed magnitude but also assign an accuracy for the grism-z and photo-z as a function of physical properties, such that the final distributions resemble those in Figure 1. We showed in Section 2.1 that the grism redshift accuracy depends on the signal-to-noise ratio of the strongest emission line and the galaxy magnitude. For the latter, we use JH_{140} as derived previously, while the former quantity needs to be parameterized in terms of other quantities available in the models.

Figure 10, left panel, shows how the emission line S/N depends both on the line flux and the JH_{140} magnitude for galaxies with a measured line flux. For each galaxy, we take the flux (in units of erg cm^{-2} s^{-1}) of the strongest line and define the line magnitude as $m_{\rm line} = -2.5 \times \log(f_{\rm line})$. At fixed line flux, brighter galaxies have more continuum, thus decreasing the line S/N. This relation is well reproduced by the following parameterization:

$$\log({\rm S/N}) = -0.33 \times (2 \times m_{\rm line} - JH_{140}) + 19.85. \quad (5)$$

Figure 10, right panel, shows the line S/N obtained with this equation. The small differences between the two panels can be due to additional variables not taken into account (e.g., dust extinction or grism throughput). We tested (by perturbing the S/N assigned to each model galaxy) that a more accurate parameterization of this relation is not required for the purpose of this paper.

In order to obtain a synthetic line $({\rm S/N})_{\rm mod}$ for the model galaxies, we first convert the star formation rate (SFR) of the model galaxies into an Hα flux (or Hβ flux, where Hα is redshifted outside the grism wavelength range) by inverting the relation given in Kennicutt (1998a). We then obtain ${\rm S/N}_{\rm mod}$ from $m_{\rm line}$, and $JH_{\rm mod}$ using Equation (5). The rank in $({\rm S/N})_{\rm mod}$ (and not the absolute value) is then matched to that in S/N for the 3D-*HST* galaxies.

Lastly, we assign to each mock galaxy a random grism redshift accuracy such that the observed distributions shown in Figure 1 are reproduced for the mock sample. A photometric redshift accuracy is also generated using the same distributions (as a sole function of $JH_{\rm mod}$).

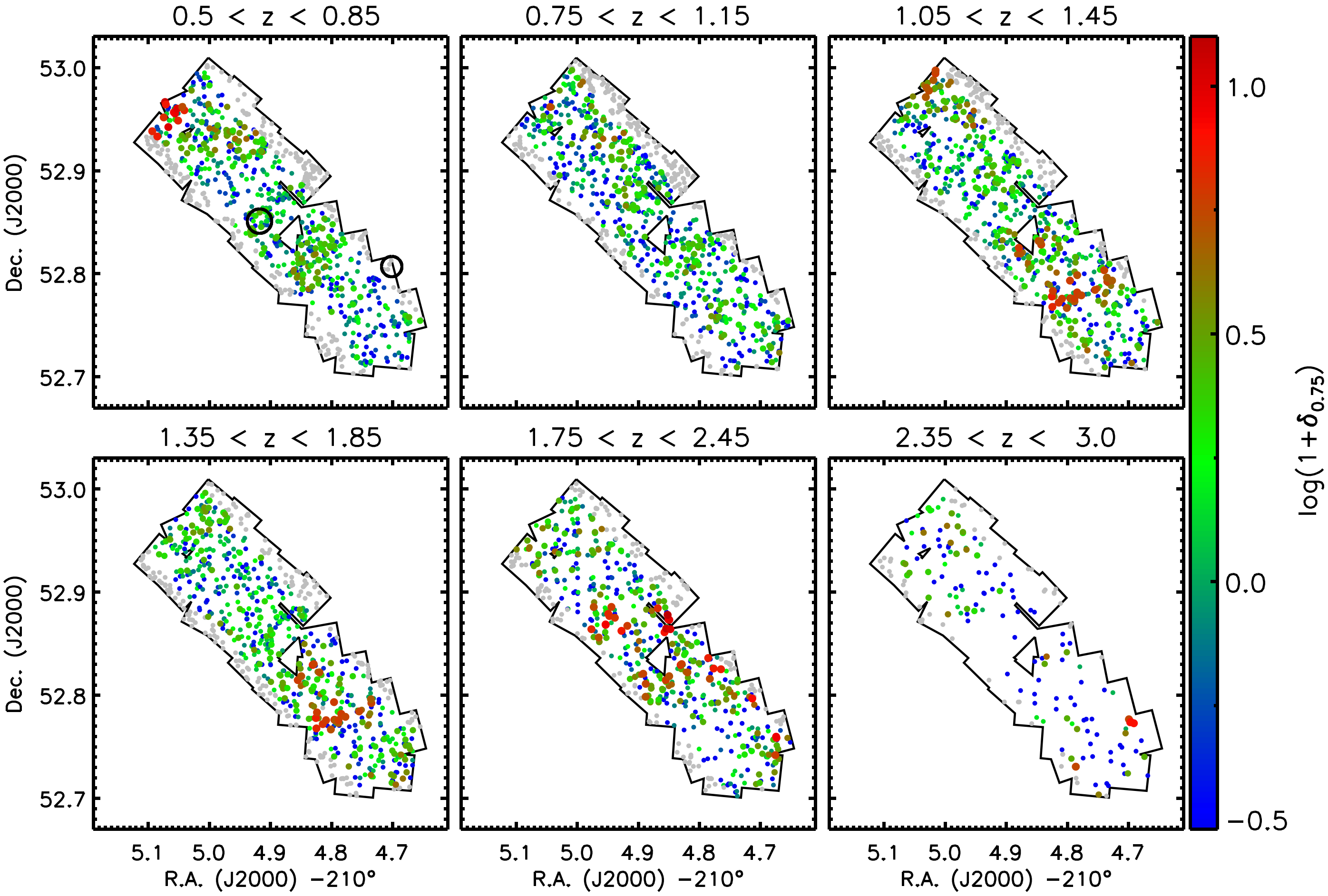

Figure 8. Same as Figure 5 but for the 3D-*HST* AEGIS field. The gray dots are for galaxies for which the aperture where the density is computed is within the photometric footprint by less than 90%. The X-ray extended emission circles (black) are from Erfanianfar et al. (2013).

Each model galaxy is then defined by three redshifts: a spectroscopic redshift, which is derived from the geometric redshift ($z_{\rm GEO}$) of the cones plus the peculiar velocity of the halo; a grism-like redshift, which is derived from the spec-z plus a random value drawn from a Gaussian distribution with sigma equal to the grism redshift accuracy derived previously; and a photometric redshift, which is derived like the previous but using the photometric redshift accuracy.

The last step in this procedure requires that for each galaxy only one of these three redshifts is selected to generate a "best" redshift. To do so, we work in bins of JH_{140} magnitude. For each bin of magnitude, the fraction of 3D-*HST* galaxies with spec-z, grism-z, and photo-z is computed. Then, in order of descending $({\rm S/N})_{\rm mod}$, the spec-z is taken for a number of galaxies, matching the fraction of galaxies with spec-z in the observational catalog; a grism-z is taken for an appropriate number of galaxies, and lastly a photo-z is taken for the galaxies with the lowest $({\rm S/N})_{\rm mod}$, which mimic line non-detections in the grism data. We stress that since the grism redshift accuracy is a function of $({\rm S/N})_{\rm mod}$, the quality of grism redshifts for objects with marginal line detections is preserved by this method.

Once a catalog of model galaxies is selected and their redshift accuracy matches the 3D-*HST* catalog, we compute the environment parameters as described in Section 3.1. The only minor difference is that, as the number of model galaxies is very large, we can remove objects closer than 1.0 Mpc from the edges of the cone to avoid edge biases.

6. Calibration of Physical Parameters

The local density of galaxies is not the only parameter that describes the environment in which a galaxy lives. Another important parameter is whether a galaxy is the dominant one within its dark matter halo (central), or if it orbits within a deeper potential well (satellite). The definition of centrals and satellites in the mock sample is obtained from the hierarchy of subhalos (the main units hosting a single galaxy). First, halos are detected using a friends-of-friends (FOF) algorithm with a linking length $b = 0.2$ (Springel et al. 2005). Then each halo is decomposed into subhalos running the algorithm SUBFIND (Springel et al. 2001), which determines the self-bound structures within the halo. As time goes by, the model follows subhalos after they are accreted onto larger structures. When two halos merge, the galaxy hosted in the more massive halo is considered the central, and the other becomes a satellite.

In this section, we describe how we use the mock catalog to assign a halo mass PDF and a probability of being central or satellite to 3D-*HST* galaxies. The method builds on the idea of finding all the galaxies in the mock light cones that match each 3D-*HST* galaxy in redshift, density, mass rank (described later), and stellar mass (within the observational uncertainties). The main advantage of using multiple parameters is to break

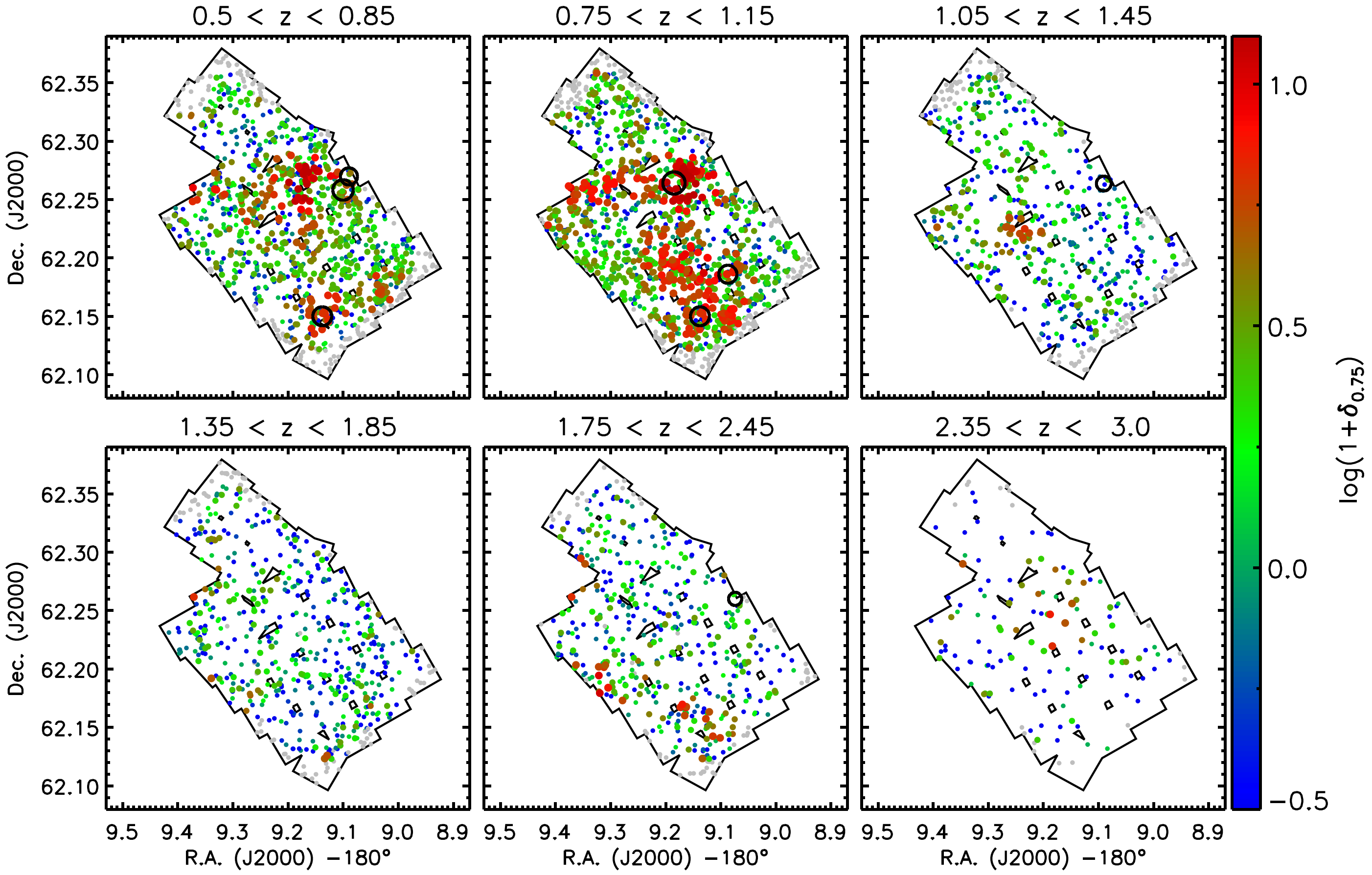

Figure 9. Same as Figure 5 but for the 3D-*HST* GOODS-N field. The gray dots are for galaxies for which the aperture where the density is computed is within the photometric footprint by less than 90%. The X-ray extended emission circles (black) are from A. Finoguenov (2016, private communication).

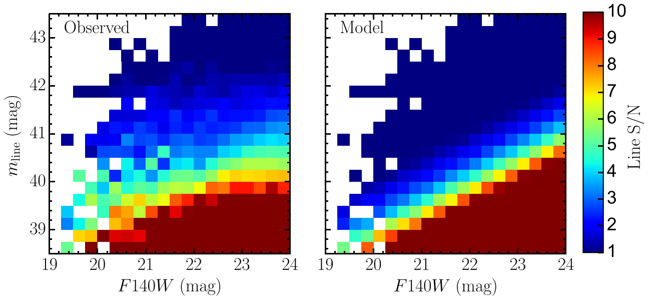

Figure 10. Left panel: emission line S/N for 3D-*HST* galaxies as a function of the JH_{140} magnitude and line magnitude. Right panel: emission line S/N obtained using the parameterization from Equation (5).

degeneracies that are otherwise dominant if only one parameter is used (e.g., to account for the role of stellar mass at low density, where halo mass depends more significantly on stellar mass than density; Fossati et al. 2015).

6.1. The Stellar Mass Rank in Fixed Apertures

Fossati et al. (2015) explored how the rank in stellar mass of a galaxy in an appropriate aperture can be a good discriminator of the central/satellite status for a galaxy. This method, which complements the one usually used in local large scale surveys of galaxies based on halo finder algorithms, is more effective with a sparser sampling of high redshift surveys.

We refer the reader to Fossati et al. (2015) for the details of how this method is calibrated. Here we recall that we define a galaxy to be central if it is the most massive (mass rank = 1) within an adaptive aperture that only depends on the stellar mass. Otherwise, if it is not the most massive (mass rank >1), it is classified as a satellite.

The adaptive aperture is motivated by the fact that, ideally, the aperture in which the mass rank is computed should be as similar as possible to the halo virial radius to maximize the completeness of the central/satellite separation and reduce the fraction of spurious classifications. Fossati et al. (2015) defined this aperture as a cylinder with radius

$$r_0 = 3 \times 10^{(\alpha \log M_* + \beta)}\ [\mathrm{Mpc}], \tag{6}$$

where M_* is the stellar mass, and $\alpha = 0.25$ and $\beta = -3.40$ are the parameters that describe the dependence of the virial radius with stellar mass. These values are calibrated using the models (see Fossati et al. 2015). We also limit the aperture between 0.35 and 1.00 Mpc. The lower limit is set to avoid small apertures that would result in low mass galaxies being assigned mass rank = 1 even if they are satellites of a large halo. The upper limit is approximately the radius of the largest halos in the redshift range under study. The adaptive aperture radius

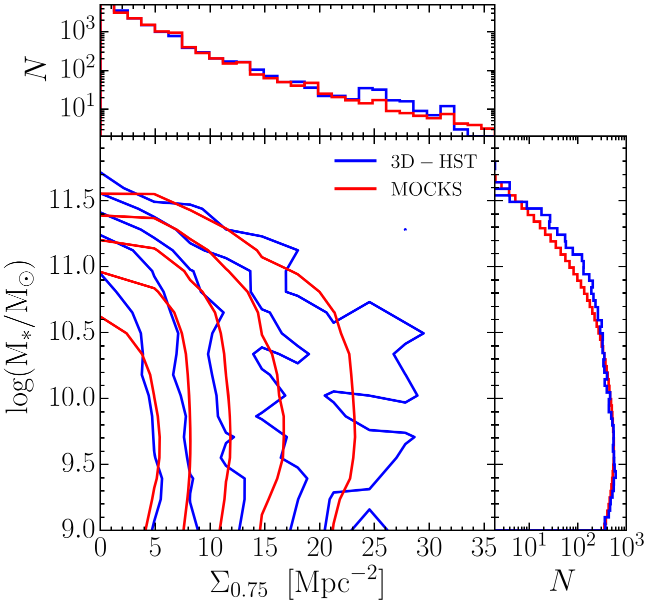

Figure 11. Main panel: bivariate distribution of density on the 0.75 Mpc scale and stellar mass for the 3D-*HST* sample (blue) and the mock sample (red). The mock contours have been scaled to account for the ratio of volumes between the light cones and the data. The contours are logarithmically spaced with the outermost contour at 4 objects per bin and the innermost at 300 objects per bin. Upper panels: marginalized distributions of density on the 0.75 Mpc scale for the 3D-*HST* and the mock samples. The counts refer to the 3D-*HST* sample, while the mock histogram has been normalized by the ratio of the volumes. Right panel: the same as previously noted but marginalized over the stellar mass.

(in Mpc) is therefore defined as

$$r = \begin{cases} 0.35 & \text{if } r_0 < 0.35 \\ r_0 & \text{if } 0.35 \leqslant r_0 \leqslant 1.00. \\ 1.00 & \text{if } r_0 > 1.00 \end{cases} \tag{7}$$

In this work, we have to consider the variable redshift accuracy of 3D-*HST* galaxies. Therefore fixing the depth of the cylinder to ±1500 km s^{-1} does not optimize the central versus satellite discrimination. We set the depth of the adaptive aperture cylinder (in km s^{-1}) to

$$dv = \begin{cases} 1500 & \text{if } \sigma_{v,\text{acc}} < 1500 \\ \sigma_{v,\text{acc}} & \text{if } 1500 \leqslant \sigma_{v,\text{acc}} \leqslant 7500 \\ 7500 & \text{if } \sigma_{v,\text{acc}} > 7500, \end{cases} \tag{8}$$

where $\sigma_{v,\text{acc}}$ is the redshift accuracy of the primary galaxy. By using the mock sample, we tested that this combination of upper and lower limits gives a pure yet sufficiently complete sample of central galaxies.

The simple classification of centrals and satellites based on mass rank only is subject to a variety of contaminating factors. For instance, in galaxy pairs or small groups (where the mass of the real central and satellites are very close), it is difficult to use the stellar mass to robustly define which galaxy is the central. On the other hand, in the infalling regions beyond the virial radius of massive clusters, many central galaxies would be classified as satellites, as analyzed in detail in Fossati et al. (2015). In this work, we go beyond the simple dichotomic definition that each galaxy is either central or satellite using the mass rank only. We combine multiple observables to derive a probability that each 3D-*HST* galaxy is central or satellite by matching observed galaxies to mock galaxies. This probabilistic approach naturally takes into account all sources of impurity and is of fundamental importance to separate the effects of mass and environment on the quenching of galaxies.

6.2. Matching Mock to Real Galaxies

In this section, we describe how we match individual 3D-*HST* galaxies to the mock sample to access physical quantities inaccessible from observations only. Our method heavily relies on the fact that the distributions of stellar mass and density (and their bivariate distribution) are well matched between the mocks and the observations across the full redshift range.

In the upper and right panels of Figure 11, we show the distributions of density and stellar mass respectively, while the main panel shows the 2D histogram of both quantities. The overall agreement is very satisfactory and relates the agreement of the observed stellar mass functions to that from Henriques et al. (2015), and to our careful selection of objects. The match of the density distributions also confirms that the redshift assignment for mock galaxies is accurate enough to reproduce the observed density distributions. A good match between models and observations is found for other apertures as well. In the future, it should be possible to improve our method by combining density information on several scales by means of machine learning algorithms.

To match observed galaxies to mock galaxies, we also require an estimate of the uncertainty on both the density and the stellar mass. For the stellar mass, we use $\sigma(\log(M_*)) = 0.15$ dex (Conroy et al. 2009; Gallazzi & Bell 2009; Mendel et al. 2014). For the density, the error budget is dominated by the redshift uncertainty of each galaxy and the fact that for a sample of galaxies with given JH_{140} and emission line S/N, the redshift accuracy has a distribution with non-zero width. This means that the redshift uncertainty of mock galaxies can only match the observational sample in a statistical sense. To test how the densities of individual galaxies are affected by the redshift uncertainty, we repeat 50 times the process of assigning a redshift to mock galaxies described in Section 5.2. We then compute the density for each of those samples independently and analyze the distribution of densities for each galaxy. We find that the distribution roughly follows a Poissonian distribution: $\sigma(\Sigma_{r_{\text{ap}}}) = \sqrt{w_{r_{\text{ap}}}}/(\pi \times r_{\text{ap}}^2)$. Based on this evidence, we match each 3D-*HST* galaxy to the mock galaxies within ±0.1 in redshift space and within $\pm\sigma(\log(M_*))$ and $\pm\sigma(\Sigma_{0.75})$ for the stellar mass and density on the 0.75 Mpc scale, respectively.

The local density is a quantity that depends on the redshift accuracy both of the primary galaxy and of the neighbors, which in turn depends on the emission line strength in the grism data and the galaxy brightness (see Section 2.1). As a result the density peaks are subject to different degrees of smoothing if the neighboring galaxies have a systematically poorer redshift accuracy in a given environment. Our mock catalog is a good representation of the observational sample only if the SFR (from which the synthetic line S/N is derived) and the stellar mass distributions as a function of environment are well reproduced by the SAM. Henriques et al. (2016) have shown that the H15 model is qualitatively able to recover the observed trends of passive fraction as a function of environment. By matching model galaxies with a redshift accuracy within ±2000 km s^{-1} to that of the observed galaxy, we introduce no bias in the halo mass distributions; for galaxies

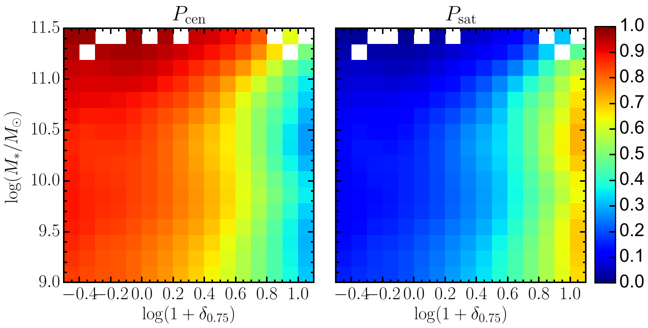

Figure 12. Average probability for a 3D-*HST* galaxy of being central ($P_{\rm cen}$, left panel) or satellite ($P_{\rm sat}$, right panel) in bins of density contrast in the 0.75 Mpc aperture and stellar mass. The trends are consistent with the analysis of mock galaxies, which shows a lower purity for the selection of centrals at high halo masses (large overdensities) and the opposite trend for satellites.

with less accurate redshifts, we simply obtain broader PDFs of halo mass.

Lastly, we restrict the match for the most massive galaxies (mass rank = 1) to the most massive mock galaxies. The rest of the population (mass rank >1) was matched to the same population in the mocks.

6.2.1. A Probabilistic Determination of Central versus Satellite Status

The central and satellite fractions of those matched mock galaxies are used to define a probability that the 3D-*HST* galaxy under consideration is central ($P_{\rm cen}$) or satellite ($P_{\rm sat}$):

$$P_{\rm cen} = \frac{N_{\rm matched\ cen}}{N_{\rm matched}}, \quad P_{\rm sat} = \frac{N_{\rm matched\ sat}}{N_{\rm matched}} = 1 - P_{\rm cen}. \tag{9}$$

Figure 12 shows the average values of those quantities in bins of logarithmic density contrast (see Section 3.1) in the 0.75 Mpc aperture and stellar mass for all the 3D-*HST* galaxies included in our sample. The average value of $P_{\rm cen}$ decreases with increasing density and decreasing stellar mass, and the opposite trend occurs for $P_{\rm sat}$. High mass halos (high-density regions) are indeed dominated by the satellite population, but objects with high stellar masses are more likely to be centrals. Galaxies in low density environments ($\log(1+\delta_{0.75}) < 0.2$) are almost entirely centrals. However, in the analysis performed in the next sections, we use the values of $P_{\rm cen}$ and $P_{\rm sat}$ computed for each galaxy instead of the average values. (Kovač et al. 2014 performs instead an average correction as a function of galaxy density.) This takes into full account possible second order dependencies on mass rank, redshift, or redshift accuracy.

We also examine how $P_{\rm sat}$ varies as a function of the distance from the center of overdense structures, such as massive groups or clusters of galaxies. To do so, we take the halos more massive than $10^{13.5}\ M_\odot$ in the mock light cones. We then select all galaxies in a redshift slice centered on the redshift of the central galaxy and within $\Delta z \leqslant \pm 0.01$ and compute their projected sky positions with respect to the central galaxy. We normalize their positions to the virial radius of the halo and remove the central galaxy.

Figure 13, top panel, shows the average value of $P_{\rm sat}$ as a function of normalized R.A. and Decl. offset from the center of the halos. The black solid circles mark $r_{\rm vir}$ and $2 \times r_{\rm vir}$. Figure 13, bottom panel, shows the average value of $P_{\rm sat}$ (black solid line) as a function of radial distance from the center of the halos. The red solid line shows the fraction of satellites in the same radial bins but using the mock definition of satellites.

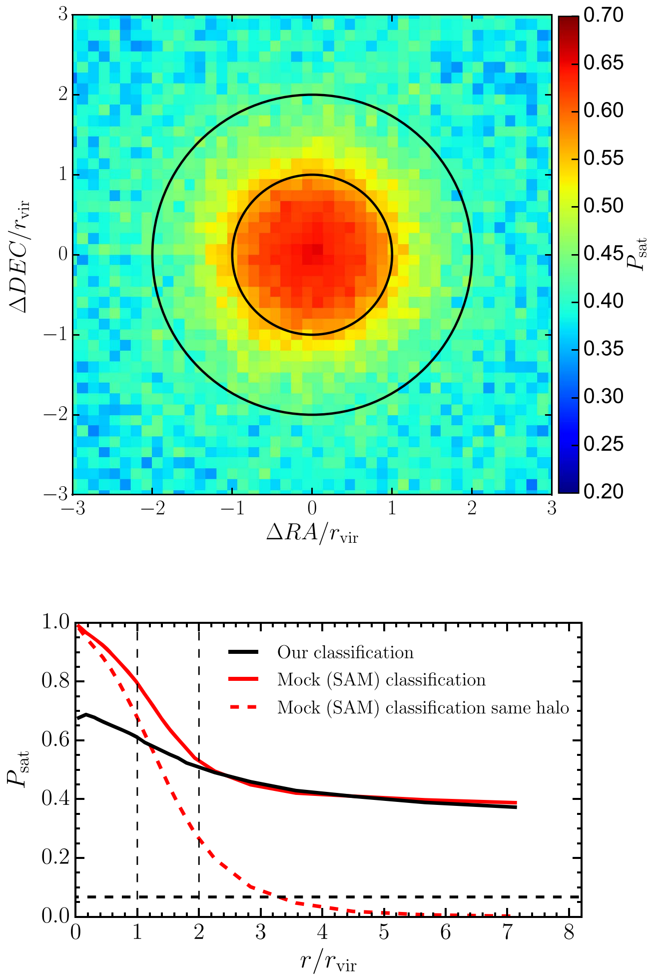

Figure 13. Top panel: average $P_{\rm sat}$ for mock galaxies as a function of normalized R.A. and Decl. offset from the center of halos more massive than $10^{13.5}\ M_\odot$. The black solid circles mark $r_{\rm vir}$ and $2 \times r_{\rm vir}$. Bottom panel: average $P_{\rm sat}$ for mock galaxies using our Bayesian definition (black solid line) or the SAM definition of satellites (red solid line) as a function of radial distance from the center of halos more massive than $10^{13.5}\ M_\odot$. The red dashed line shows the value of $P_{\rm sat}$ obtained from SAM satellites living in the same halo of the central galaxy. The plateau of $P_{\rm sat}$ at large radii is caused by the contribution of satellites from nearby halos. The vertical dashed lines mark $r_{\rm vir}$ and $2 \times r_{\rm vir}$. The horizontal dashed line is the value of $P_{\rm sat}$ for a stellar mass and redshift matched sample of galaxies living in average density environments.

Lastly, the red dashed line shows the value of $P_{\rm sat}$, including only SAM satellites living in the same halo of the central galaxy.

Our Bayesian definition tracks well the SAM definition of satellites as a function of halo mass. However, the real trend is smoothed due to both the transformation from real to redshift space, and the intrinsic uncertainty of our method to extract $P_{\rm sat}$ based on observational parameters. Moreover, $P_{\rm sat}$ only drops to 40% at $\sim 5 \times r_{\rm vir}$. This is caused by satellites from nearby halos, while the contribution from satellites belonging to the same halo becomes negligible at $\sim 3 \times r_{\rm vir}$. Indeed, massive structures are embedded in filaments and surrounded by groups that will eventually merge with the cluster. Therefore, even at large distances from the center, the density is higher than the mean density (at $\sim 5 \times r_{\rm vir}$ the density is ~ 4 times higher than the average density). As a reference we show in Figure 13, bottom panel, the value of $P_{\rm sat}$ for a stellar mass and redshift

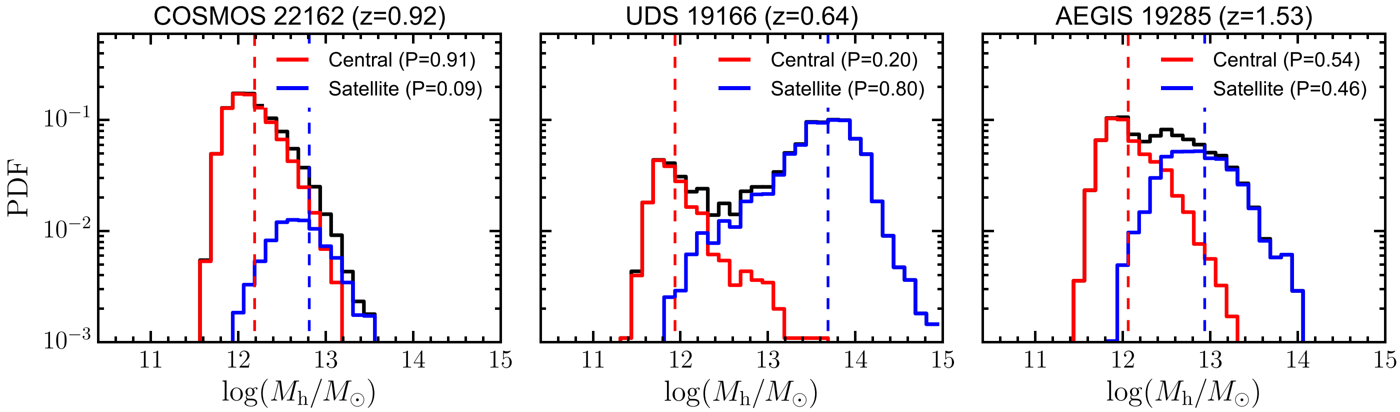

Figure 14. Example halo mass PDFs for three 3D-*HST* galaxies. The left panel shows a galaxy with a high probability of being a central, the middle panel one with a high probability of being a satellite, and the right panel an object with an almost equal probability of being a central or a satellite. The red and blue histograms show the halo mass probability given that the galaxy is a central ($P_{M_h|\mathrm{cen}}$) or a satellite ($P_{M_h|\mathrm{sat}}$), while the black histogram is the total halo mass PDF. The histograms are normalized such that the area under them gives P_{cen} and P_{sat}, respectively. The vertical dashed lines mark the median halo mass for a given type.

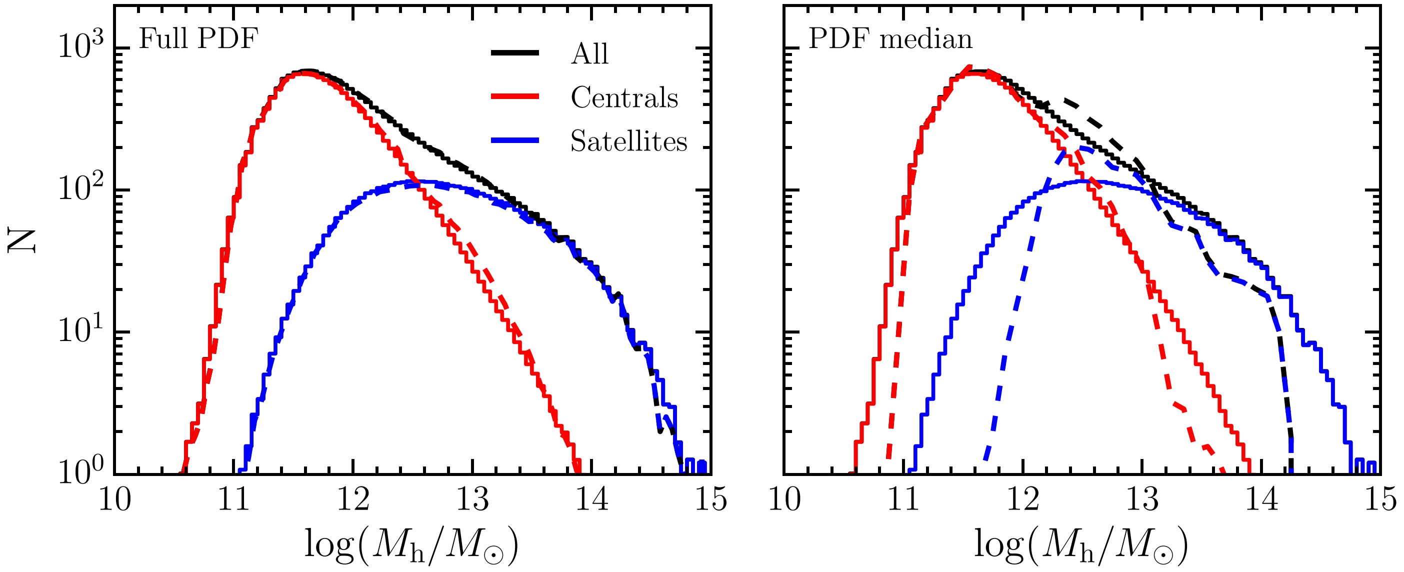

Figure 15. Comparison of the halo mass distributions for the mock galaxies (solid histograms) and 3D-*HST* galaxies (dashed lines). In the left panel the dashed lines are obtained by summing the full halo mass PDFs for centrals ($P_{M_h|\mathrm{cen}}$, red) and satellites ($P_{M_h|\mathrm{sat}}$, blue) weighted by P_{cen} and P_{sat} for each galaxy. In the right panel the dashed lines are obtained from the single value estimator (median value of the PDF given the type), weighted by the probability that a galaxy is of a given type. The black histograms and dashed lines are the sum of the colored values.

matched sample of galaxies living in average density environments ($0.8 < (1 + \delta_{0.75}) < 1.2$, horizontal dashed line).

6.2.2. The Halo Mass Calibration

Similarly, we use the halo masses of matched central and satellite model galaxies to generate the halo mass PDFs, given their type ($P_{M_h|\mathrm{cen}}$ and $P_{M_h|\mathrm{sat}}$, respectively). Figure 14 shows three examples of such PDFs for one object with high P_{cen}, one with high P_{sat}, and one object with an almost equal probability of being a central or a satellite. The vertical dashed lines mark the median halo mass for a given type. Although the total halo mass PDF can be double peaked (middle panel), the degeneracy between the two peaks is broken once the galaxy types are separated, making the median values well determined for each type independently.

6.3. Testing Calibrations

We test the halo mass calibration by comparing the halo mass distributions of the mock sample to the 3D-*HST* sample. In both panels of Figure 15, we plot the halo mass histograms for centrals and satellites of the entire mock sample. The number counts are scaled by the ratio of the volume between the 24 light cones and the five 3D-*HST* fields.

In the left panel of Figure 15 the dashed lines are the halo mass distributions of 3D-*HST* galaxies obtained by summing the full halo mass PDFs for centrals ($P_{M_h|\mathrm{cen}}$, red dashed) and satellites ($P_{M_h|\mathrm{sat}}$, blue dashed), weighted by P_{cen} and P_{sat} for each galaxy. The agreement with the mock sample distributions is remarkable. Although this is in principle expected because the halo mass PDFs for observed galaxies are generated from the mock sample, it should be noted that we perform the match in bins of redshift, redshift accuracy, stellar mass, density, and

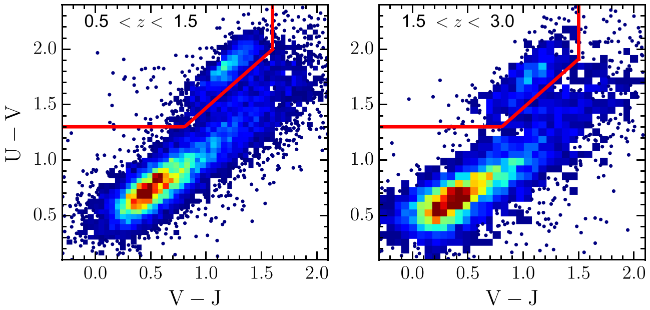

Figure 16. Rest-frame UVJ diagram for 3D-*HST* galaxies in two redshift bins. The color scale represents the density of points. Where the density is low, we plot individual galaxies. The solid red line indicates the adopted separation between passive galaxies and star-forming galaxies.

mass rank. The good agreement for the whole sample between the derived PDFs and the mock distributions (for centrals and satellites separately) should therefore be taken as evidence that our method has not introduced any bias in the final PDFs.

We take the median value of the halo mass PDFs, given that each galaxy is a central ($M_{h,50|\mathrm{cen}}$) or a satellite ($M_{h,50|\mathrm{sat}}$), as an estimate of the "best" halo mass, weighted by P_{cen} and P_{sat}. These values are shown in Figure 15, right panel. The agreement with the mock distributions is good. For central galaxies, the shape and extent of the distribution is well preserved. For satellite galaxies, the halo mass range is less extended than the one in the mocks; values above $10^{14.2}\,M_{\odot}$ and below $10^{12}\,M_{\odot}$ indeed only contribute through the tails of the PDFs, and therefore do not appear when the median of the PDFs are used.

In the next section, we make use of the full PDFs to derive constraints on the environmental quenching of satellite galaxies. However, the satisfactory agreement of single value estimates of halo mass with the mock distributions makes them a valuable and reliable estimate in science applications when the use of the full PDFs is not possible or feasible.

7. Constraining Environmental Quenching Processes At $z = 0.5$–2

In this section, we explore the role of environment in quenching the star formation activity of galaxies over $0.5 < z < 2$ using 3D-*HST* data. It was first proposed by Baldry et al. (2006) that the fraction of passive galaxies depends both on stellar mass and environment in a separable manner. Peng et al. (2010), using the SDSS and zCOSMOS surveys, extended the independence of those processes to $z \sim 1$. More recently, Peng et al. (2012) interpreted these trends in the local universe by suggesting that central galaxies are only subject to "mass quenching," while satellites suffer from the former plus an "environmental quenching." Kovač et al. (2014) similarly found that satellite galaxies are the main drivers of environmental quenching up to $z \sim 0.7$ using zCOSMOS data.

Here, we extend these analyses to higher redshift by exploring the dependence of the fraction of passive galaxies on stellar mass, halo mass, and central/satellite status in order to derive the efficiency and timescale of environmental quenching. In Appendix B, we show that we obtain consistent results using the observed galaxy density, as opposed to calibrated halo mass.

7.1. Passive Fractions

The populations of passive and star-forming galaxies are typically separated either by a specific star formation rate cut (e.g., Franx et al. 2008; Hirschmann et al. 2014; Fossati et al. 2015) or by a single color or color–color selection (e.g., Bell et al. 2004; Weiner et al. 2005; Whitaker et al. 2011; Mok et al. 2013; Muzzin et al. 2013). In this work, we use the latter method and select passive and star-forming galaxies based on their position in the rest-frame UVJ color–color diagram (Williams et al. 2009). Following Whitaker et al. (2011), passive galaxies are selected to have

$$(U - V) > 0.88 \times (V - J) + 0.59 \tag{10}$$

$$(U - V) > 1.3,\ (V - J) < 1.6\ [0.5 < z < 1.5] \tag{11}$$

$$(U - V) > 1.3,\ (V - J) < 1.5\ [1.5 < z < 2.0], \tag{12}$$

where the colors are rest-frame and are taken from Momcheva et al. (2016). Figure 16 shows the distribution of 3D-*HST* galaxies in the rest-frame UVJ color–color plane. The red solid line shows the adopted division between passive and star-forming galaxies.

The fractions of passive centrals and satellites in bins of M_* and M_h are computed as the fraction of passive objects in a given stellar mass bin, where each galaxy is weighted by its probability of being central or satellite and the probability of being in a given halo mass bin for its type. Algebraically,

$$f_{\mathrm{pass|ty}} = \frac{\sum_i \left(\delta_{\mathrm{pass,i}} \times \delta_{M_*,\mathrm{i}} \times P_{\mathrm{ty,i}} \times \int_{M_h} P_{M_h,i|ty}\, dM_h\right)}{\sum_i \left(\delta_{M_*,\mathrm{i}} \times P_{\mathrm{ty,i}} \times \int_{M_h} P_{M_h,i|ty}\, dM_h\right)}, \tag{13}$$

where ty refers to a given type (centrals or satellites), $\delta_{\mathrm{pass,i}}$ is 1 if a galaxy is UVJ passive and 0 otherwise, $\delta_{M_*,\mathrm{i}}$ is 1 if a galaxy is in the stellar mass bin and 0 otherwise, $P_{\mathrm{ty,i}}$ is the probability that a galaxy is of a given type (see Section 6.2.1), and $\int_{M_h} P_{M_h,i|ty}\, dM_h$ is the halo mass PDF given the type integrated over the halo mass bin limits (see Section 6.2.2).

The data points in Figure 17 show the passive fractions in two bins of halo mass (above and below $10^{13}\,M_{\odot}$) and in three independent redshift bins. The median (log) halo masses for satellites are 12.36, 13.53 at $z = 0.5$–0.8 for the lower and higher halo mass bin, respectively; 12.41, 13.44 at $z = 0.8$–1.2; and 12.43, 13.34 at $z = 1.2$–1.8.

The uncertainties on the data points cannot be easily evaluated assuming binomial statistics because the number of galaxies contributing to each point is not a priori known. Indeed, $P_{\mathrm{ty,i}}$ and $\int_{M_h} P_{M_h,i|ty}\, dM_h$ act as weights, and all galaxies with a stellar mass within the mass bin do contribute to the passive fraction. To assess the uncertainties, we use the mock light cones (where each mock galaxy has been assigned a P_{cen} and P_{sat} and halo mass PDFs, as if they were observed galaxies). In a given stellar mass bin we assign each model galaxy to be either passive or active, such that the fraction of passive galaxies matches the observed one. Then we randomly select a number of model galaxies equal to the number of observed galaxies in that bin, and we compute the passive fraction of this subsample using Equation (13). We repeat this procedure 50,000 times to derive the 1σ errorbars shown in Figure 17. This method accounts for uncertainties in the estimate of $P_{\mathrm{ty,i}}$ and $\int_{M_h} P_{M_h,i|ty}\, dM_h$, as well as cosmic variance.

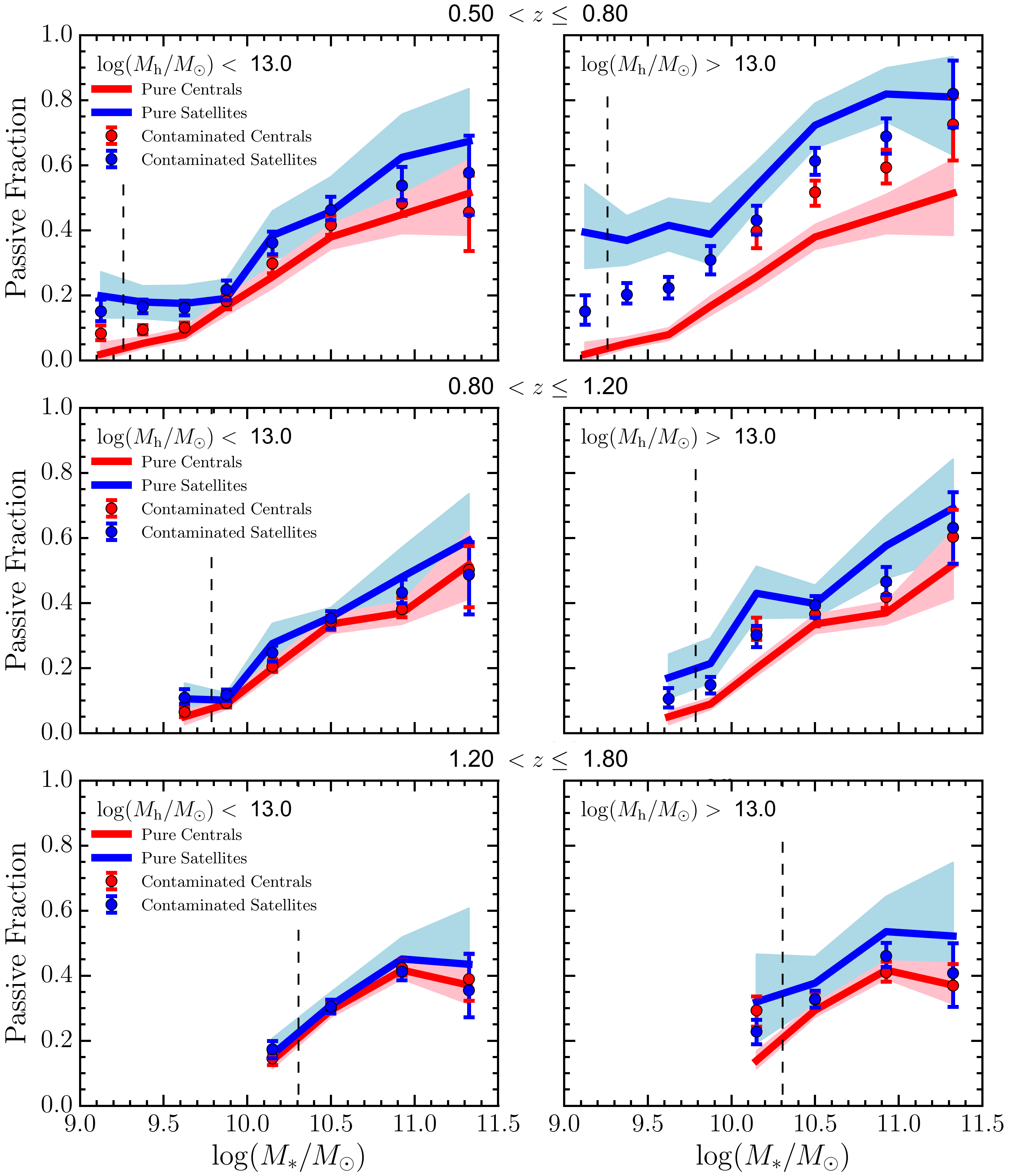

Figure 17. Passive fraction for central and satellite galaxies in bins of M_* and M_h in three independent redshift bins. The median (log) halo masses for satellites are 12.36, 13.53 at $z = 0.5$–0.8 for the lower and higher halo mass bin, respectively; 12.41, 13.44 at $z = 0.8$–1.2; and 12.43, 13.34 at $z = 1.2$–1.8. Data points show the observed passive fractions with uncertainties derived from Monte Carlo resampling of the mock sample. The thick red line is the passive fraction of a pure sample of central galaxies from the 3D-*HST* data set. The thick blue line represents our modeled "pure" passive fraction of satellites (see Section 7.2 for the details of the modeling process). In both cases the shaded regions show the 1σ confidence intervals. The vertical dashed line marks the stellar mass limit of the volume limited sample.

The vertical dashed lines, in Figure 17, mark the stellar mass completeness limit derived following Marchesini et al. (2009). In brief, we use the 3D-*HST* photometric catalog (down to $JH_{140} = 25$ mag), and we scale the stellar masses of the galaxies as if they were at the spectroscopic sample limit of $JH_{140} = 24$ mag (which defines the sample used in this work). The scatter of the points is indicative of the M/L variations in the population at a given redshift. We then take the upper 95th percentile of the distributions as a function of redshift as the stellar mass limit, which is approximately $\sim 10^{9.5}$ and $\sim 10^{10.5}$ for old and red galaxies at $z = 1$ and $z = 2$, respectively. Below this mass we limit the upper edge of the redshift slice such that all galaxies in the stellar mass bin are included in a mass complete sample. A stellar mass bin is included only if the covered volume is greater than one-third of the total volume of the redshift slice. This typically results in only one stellar mass bin below the completeness limit being included in the analysis.

In the highest halo mass bin of Figure 17 at $z = 0.5$–0.8, the satellite passive fraction (integrated over all galaxies) is higher than the central passive fraction, with a marginal significance. The same trend can be observed in the other halo mass and redshift bins, although the separation of the observed satellite and central passive fractions becomes more marginal.

In each redshift bin we also identify a sample of "pure" central galaxies ($P_{\rm cen} > 0.8$, irrespective of overdensity or halo mass), which provides a reference for the passive fraction of galaxies subject only to mass quenching. The passive fraction of this sample $f_{\rm pass|cen,pure}(M_*)$ of centrals (which has an average $P_{\rm cen} = 0.95$) is shown as the thick red line in both halo mass bins.

The separation of the observed satellite passive fraction from that of the pure sample of centrals is more significant (especially at $z < 1.2$). Indeed, the passive fractions derived using Equation (13) can be strongly affected by impurities in the central/satellite classification and by cross-talk between the two halo mass bins, given that each galaxy can contribute to both bins and types (see Equation (13)). Any contribution of central galaxies to the satellite passive fraction, and vice versa, will reduce the observed difference between the two populations with respect to the "pure," intrinsic difference.

7.2. Recovering the "Pure" Passive Fractions for Satellite Galaxies

In order to recover the "pure" passive fraction for satellite galaxies as a function of halo mass, we perform a parametric model fitting to our data set.

We start by parameterizing the probability of a satellite galaxy being passive independently in each stellar mass bin as a function of log halo mass, using a broken function characterized by a constant value ($P_{\rm pass,lo}$) below the lower break ($M_{\rm br,lo}$) and another constant value ($P_{\rm pass,hi}$) above the upper break ($M_{\rm br,hi}$). In between the breaks, the passive fraction increases linearly. Algebraically, this four-parameter function is defined as

$$P_{\rm pass|sat}(M_h) = \begin{cases} P_{\rm pass,lo} & \text{if } M_h \leqslant M_{\rm br,lo} \\ m \times \left(\log \frac{M_h}{M_{\rm br,lo}}\right) + P_{\rm pass,lo} & \text{if } M_{\rm br,lo} < M_h \leqslant M_{\rm br,hi}, \\ P_{\rm pass,hi} & \text{if } M_h > M_{\rm br,hi} \end{cases} \tag{14}$$

Table 1
Table of the Model Parameters

Parameter	Range	Nbins	Prior
$\log M_{\rm br,lo}$	11, 15	80	Uniform
$\log M_{\rm br,hi}$	11, 15	80	Uniform
$P_{\rm pass,hi}$	0.0, 1.0	100	Gaussian (if $P_{\rm pass,hi} \leqslant f_{\rm pass|cen,pure}$) Uniform (if $P_{\rm pass,hi} > f_{\rm pass|cen,pure}$)

where $m = (P_{\rm pass,hi} - P_{\rm pass,lo})/(\log(M_{\rm br,hi}) - \log(M_{\rm br,lo}))$.

This function is chosen to allow for a great degree of flexibility. We make the assumption that satellite galaxies are not subject to environmental quenching below $M_{\rm br,lo}$, and therefore treat $P_{\rm pass,lo}$ as a nuisance parameter of the model with a Gaussian prior centered on the observed passive fraction of pure centrals $f_{\rm pass|cen,pure}(M_*)$ and a sigma equal to its uncertainty. For $P_{\rm pass,hi}$, instead we assume a semi-Gaussian prior with the same center and sigma as given previously, but only extending below the observed passive fraction of central galaxies (which implies that satellites are affected by the same mass quenching as centrals). Above this value we assume a uniform prior. For the break masses we assume uniform priors. Table 1 summarizes the model parameters, their allowed range, and the number of bins, in which the range is divided to compute the posterior.

The probability that each 3D-*HST* galaxy, i, is passive is

$$P_{\rm pass,i} = P_{\rm cen,i} \times P_{\rm pass|cen} + P_{\rm sat,i} \times \int_{M_h} P_{M_h i|\rm sat} \times P_{\rm pass|sat}\, dM_h, \tag{15}$$

where $P_{\rm pass|sat}$ is from Equation (14) and $P_{\rm pass|cen} = f_{\rm pass|cen,pure}$.

The likelihood space that the star-forming or passive activity of 3D-*HST* galaxies in a stellar mass bin is reproduced by the model is computed as follows:

$$\mathcal{L} = \prod_i \begin{cases} P_{\rm pass,i} & \text{if } i \text{ is UVJ passive} \\ 1 - P_{\rm pass,i} & \text{if } i \text{ is not UVJ passive} \end{cases}. \tag{16}$$

We compute the posterior on a regular grid covering the parameter space. We then sample the posterior distribution, and we apply the model described in Equation (14) to obtain the median value of $P_{\rm pass|sat}$ and its 1σ uncertainty as a function of halo mass. Lastly, we assign the probability of being passive to mock satellites in each stellar mass bin according to their model halo mass, and we compute the average passive fraction in the two halo mass bins (above and below $10^{13} M_\odot$). This results in the thick blue ($f_{\rm pass|sat,pure}(M_*)$) lines with 1σ confidence intervals plotted as shaded regions in Figure 17. We illustrate in Appendix C an example of this procedure applied to a single redshift bin.

We verify that the separation seen in the pure passive fractions in Figure 17 is real. To do so we randomly shuffle the position in the UVJ diagram for galaxies in each stellar mass bin (irrespective of environmental properties) to break any correlation between passive fraction and environment. Then we compute the observed passive fractions of centrals and satellites, and for the pure sample of centrals, and we perform again the model fitting procedure.

At $0.5 < z < 0.8$ we find that the pure satellite passive fraction is inconsistent with the null hypothesis (no satellite quenching) at a $\gtrsim 2\sigma$ level in each stellar bin at high halo mass, and seven out of eight stellar mass bins at low halo mass. The combined probability of the null hypothesis is $P < 10^{-10}$ in either halo mass bin. The difference is smaller, but still very significant ($P \lesssim 10^{-5}$) at $0.8 < z < 1.2$. At $1.2 < z < 1.8$ the hypothesis of no satellite quenching is acceptable ($P \sim 0.4$) in the low halo mass bin, while it can be ruled out ($P \lesssim 10^{-5}$) at higher halo mass.

Van der Burg et al. (2013), Kovač et al. (2014), and Balogh et al. (2016) have found that the environment plays an important role in determining the star formation activity of satellites, at least up to $z \sim 1$. However, these works have only probed relatively massive halos ($M_h \gtrsim 10^{13}\,M_\odot$). The depth of the 3D-*HST* sample allows us, for the first time, to extend these results to higher redshift, to lower mass galaxies, and to lower mass halos.

7.3. Satellite Quenching Efficiency

In order to further understand the increased passive fractions for satellite galaxies, we compute the "conversion fractions" as first introduced by van den Bosch et al. (2008). This parameter, sometimes called the satellite quenching efficiency, quantifies the fraction of galaxies that had their star formation activity quenched by environment specific processes, since they accreted as satellites into a more massive halo (see also Hirschmann et al. 2014; Kovač et al. 2014; Balogh et al. 2016). It is defined as

$$f_{\mathrm{conv}}(M_*, M_h) = \frac{f_{\mathrm{pass|sat,pure}}(M_*, M_h) - f_{\mathrm{pass|cen,pure}}(M_*)}{1 - f_{\mathrm{pass|cen,pure}}(M_*)}, \tag{17}$$

where $f_{\mathrm{pass|sat,pure}}(M_*, M_h)$ and $f_{\mathrm{pass|cen,pure}}(M_*)$ are the corrected fractions of quenched centrals and satellites in a given bin of M_* and M_h, obtained as described previously.

In Equation (17) we compare the sample of centrals at the same redshift as the satellites. This builds on the assumption that the passive fraction of central galaxies only depends on stellar mass and that the effects of mass and environment are independent and separable. The conversion fraction then represents the fraction of satellites that are quenched due to environmental processes above what would happen if those galaxies would have evolved as centrals of their halos. A different approach would be to compare the passive fraction of satellites to that of centrals at the time of infall in order to measure the total fraction of satellites quenched since they were satellites (e.g., Wetzel et al. 2013; Hirschmann et al. 2014). However this measurement includes the contribution of mass-quenched satellite galaxies, which we instead remove under the assumption that the physical processes driving mass quenching do not vary in efficiency when a galaxy becomes a satellite.

We also caution the reader that Equation (17) has to be taken as a simplification of reality, as it does not take into account differential mass growth of centrals and satellites that can be caused by tidal phenomena in dense environments or different star formation histories.

Figure 18 shows the conversion fractions in the same bins of M_*, M_h, and redshift as presented in Figure 17. Previous results from galaxy groups and clusters from Knobel et al. (2013) and Balogh et al. (2016) are plotted in our higher halo mass bin (colored points with errorbars). We also add the conversion fractions from Kovač et al. (2014) obtained from zCOSMOS data as a function of local galaxy overdensity. We plot their overdensity bins above the mean overdensity in our higher halo mass bin and the others in our lower halo mass bin, following the overdensity to halo mass conversion given in Kovač et al. (2014). The agreement of our measurements with other works is remarkable, considering that different techniques to define the environment (density and central/satellite status) and passiveness are used in different works.

The satellite quenching efficiency tends to increase with increasing stellar mass and to decrease with increasing redshift at fixed stellar mass. In the lower halo mass bin, we note the presence of similar trends as at higher halo masses, although the uncertainties are larger due to the smaller number of satellites. In our probabilistic approach this is due to the lower P_{sat} in low density environments, as shown in Figure 12. Moreover, f_{conv} is poorly constrained at $M_* > 10^{11}\,M_\odot$, due to small number statistics of high mass satellites in the 3D-*HST* fields.

7.4. Quenching Timescales

A positive satellite conversion fraction can be interpreted in terms of a prematurely truncated star formation activity in satellite galaxies, compared to field centrals of similar stellar mass.

We define the quenching timescale (T_{quench}) as the average time elapsed from the first accretion of a galaxy as satellite to the epoch at which the galaxy becomes passive, and we estimate it by assuming that galaxies that have been satellites for longer times are more likely to be quenched (Balogh et al. 2000; McGee et al. 2009; Mok et al. 2014). Indeed, the quenching can be interpreted to happen a certain amount of time after satellite galaxies cease to accrete material (including gas) from the cosmic web (see Section 8).

In practice, we obtain quenching timescales from the distribution of T_{sat} for satellite galaxies, which we define as the time the galaxy has spent as a satellite of halos of any mass since its first infall (e.g., Hirschmann et al. 2014). For each bin of M_*, M_h, and redshift, we select all satellite galaxies in our mock light cones that define the distribution of T_{sat}. Then we select as the quenching timescale the percentile of this distribution that corresponds to $1 - f_{\mathrm{conv}}(M_*, M_h)$. This method builds on the assumption that the infall history of observed satellites is well reproduced by the SAM. Systematic uncertainties can arise in the analytic prescriptions used for the dynamical friction timescale of satellites whose parent halo has been tidally stripped in the *N*-body simulation below the minimum mass for its detection (the so-called orphan galaxies). When this time is too short, too many satellites merge with the central galaxy and are removed from the sample, and vice versa when the time is too long. De Lucia et al. (2010) explored the dynamical friction timescale in multiple SAMs, finding a wide range of timescales. However, a dramatically wrong dynamical friction recipe impacts the fraction of satellites, the stellar mass functions, and the density-mass bivariate distribution, which we found to be well matched between the mocks and the observations.

In principle low stellar mass galaxies ($M_* < 10^{10}\,M_\odot$) are more affected by the resolution limit of the simulation, and their derived quenching timescales might be subject to a larger uncertainty compared to galaxies of higher stellar mass. We verified that this is not the case by comparing the distribution of T_{sat} in two redshift snapshots ($z = 1.04$ and $z = 2.07$) of

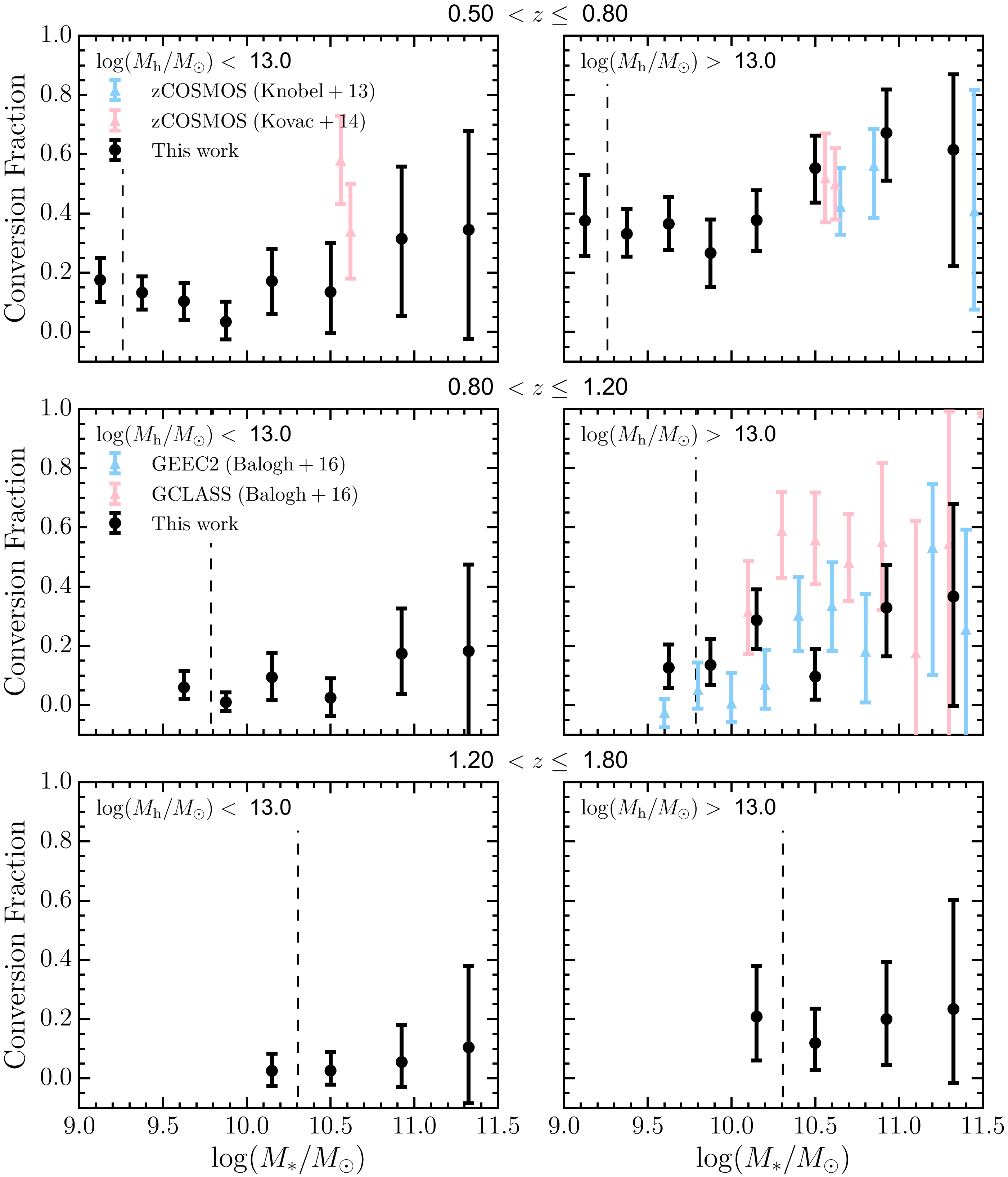

Figure 18. Conversion fractions for satellite galaxies in bins of M_* and M_h obtained from Equation (17) in three independent redshift bins. Black points are from this work and the 1σ errorbars are propagated from the uncertainties on the passive fractions using a Monte Carlo technique. Colored points are from previous studies in the same redshift range. We note a good agreement with our measurements, despite different passiveness criteria and environment estimates. The vertical dashed line marks the stellar mass limit of the volume limited sample.

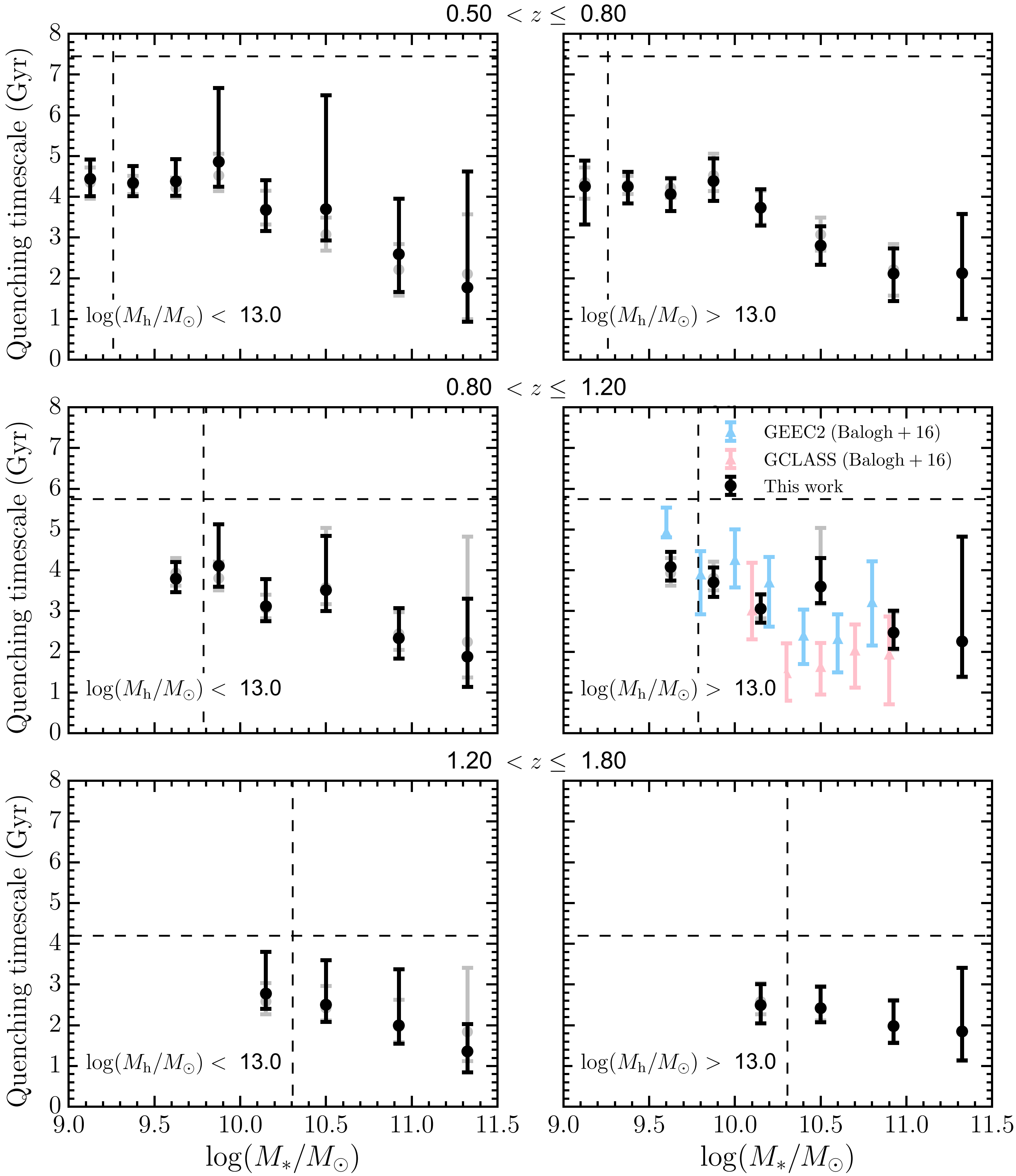

Figure 19. Quenching times for satellite galaxies in bins of M_* and M_h, obtained from the distributions of $T_{\rm sat}$ from the mock sample. Quenching times are obtained under the assumption that the galaxies that have been satellites the longest are those that have been environmentally quenched. Black points are from this work, while colored points are from previous studies in the same redshift and halo mass range. The gray points are obtained from our sample without separating the data set in two halo mass bins, and are therefore identical in the left and right panels. The vertical dashed line marks the stellar mass limit of the volume limited sample. The horizontal dashed line is the age of the universe at the central redshift of each bin.

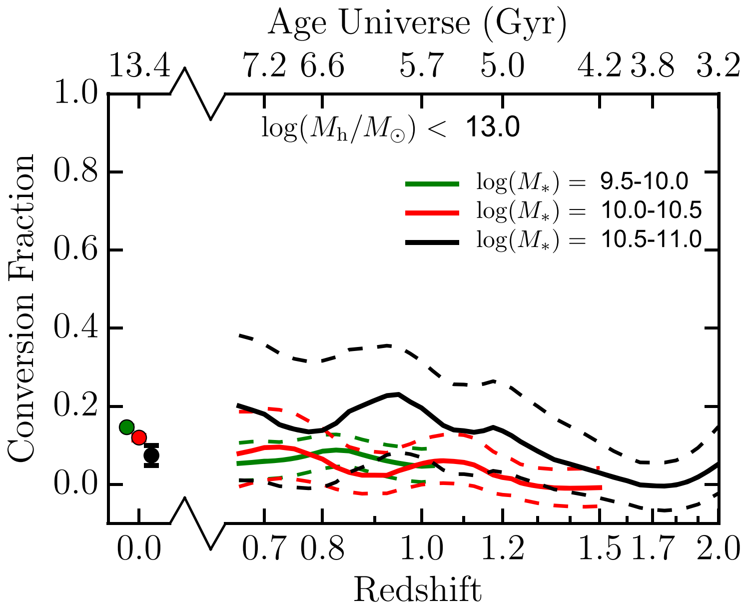

Figure 20. Conversion fractions for satellite galaxies as a function of redshift in bins of M_* and M_h (solid lines). Dashed lines mark the 1σ confidence levels. The horizontal error bar is the span of the redshift bins (for the 3D-*HST* sample), which is constant in $\Delta z/(1+z) = 0.2$, where Δz is the width of the redshift bin and z its center. Data points at $z = 0$ are from the SDSS sample and are offset along the x-axis for clarity if they overlap.

Henriques et al. (2015), built on the Millennium-I and the Millennium-II simulations. The latter is an N-body simulation started from the same initial conditions of the original Millennium run, but with a higher mass resolution at the expense of a smaller volume. The higher resolution means that the subhalos hosting low mass satellites galaxies, which can be tidally stripped, are explicitly tracked to lower mass and later times. While these are detected, the recipe for dynamical friction is not invoked. We obtain consistent quenching timescales for Millennium-I and Millennium-II based mock catalogs, and therefore we conclude that the analytical treatment of orphan galaxies does not bias our results.

Figure 19 shows our derived quenching timescales (black points) in the same bins of M_* and M_h and redshift, as presented in Figures 17 and 18. The observed trend of $f_{\rm conv}$ with stellar mass that is found in both redshift bins turns into a trend of $T_{\rm quench}$. Quenching timescales increase to lower stellar mass in all redshift and halo mass bins, mainly as a consequence of the decreasing conversion fraction. This parameter ranges from ∼4–5 Gyr for low mass galaxies to <2 Gyr for the most massive ones, and is in agreement with that found by Balogh et al. (2016).

Remarkably, the dependence of quenching timescale on halo mass is very weak. We overplot in each panel, as gray symbols, the quenching timescales obtained from our sample with the same procedure described previously but without separating the data in two halo mass bins. In most of the stellar mass bins we find a good agreement, within the uncertainties, between the black and the gray points.

The lack of a strong halo mass dependence is a consequence of the typically shorter time since infall for satellite galaxies in lower mass halos, which largely cancels the lower conversion fraction in low mass halos and suggests that the physical process responsible for the premature suppression of star formation in satellite galaxies (when the universe was half its present age) is largely independent of halo mass.

A mild redshift evolution is also seen when comparing the redshift bins: passive satellites at higher redshift are quenched on a shorter timescale. In the next section we will further explore the redshift evolution of the quenching timescales from $0 < z < 2$ by combining the 3D-*HST* sample with a local galaxy sample from SDSS.

7.5. Redshift Evolution of the Quenching Timescales

Figures 20 and 21 show the evolution of the conversion fraction and the quenching timescale from redshift 0 to 2. We now concentrate on three bins of stellar mass, each of 0.5 dex in width, and ranging from $10^{9.5}\,M_{\odot}$ to $10^{11}\,M_{\odot}$.

Given that $f_{\rm conv}$ (and consequently $T_{\rm quench}$) are poorly constrained at $M_* > 10^{11}\,M_{\odot}$ due to the low number statistics of massive satellites, we exclude more massive galaxies from these plots. Similarly, galaxies at $M_* < 10^{9.5}\,M_{\odot}$ are only included in the mass limited sample at the lowest end of the redshift range under study; therefore the redshift evolution of $f_{\rm conv}$ and $T_{\rm quench}$ cannot be derived for those low mass galaxies. A stellar mass bin appears in Figures 20 and 21 only if the stellar mass range above the mass limit is more than half of the entire stellar mass extent of the bin.

The values (solid lines) and their associated uncertainties (dashed lines) are obtained by performing the procedure described in the previous sections in overlapping redshift bins, defined such that $\Delta z/(1+z) = 0.2$, where Δz is the width of the redshift bin and z its center. This means we span larger volumes at higher redshift, modulating the decrease in sample density (Malmquist bias) and retaining sufficient sample statistics. It is also close to a constant bin in cosmic time. The x-axis of both figures is scaled such that the width of the redshift bins is constant and is shown as the horizontal error bar. We include only galaxies in a stellar mass complete sample for each redshift bin. In addition to the 3D-*HST* based constraints, we add constraints at $z = 0$, obtained using the same method to ensure homogeneity. The observational sample

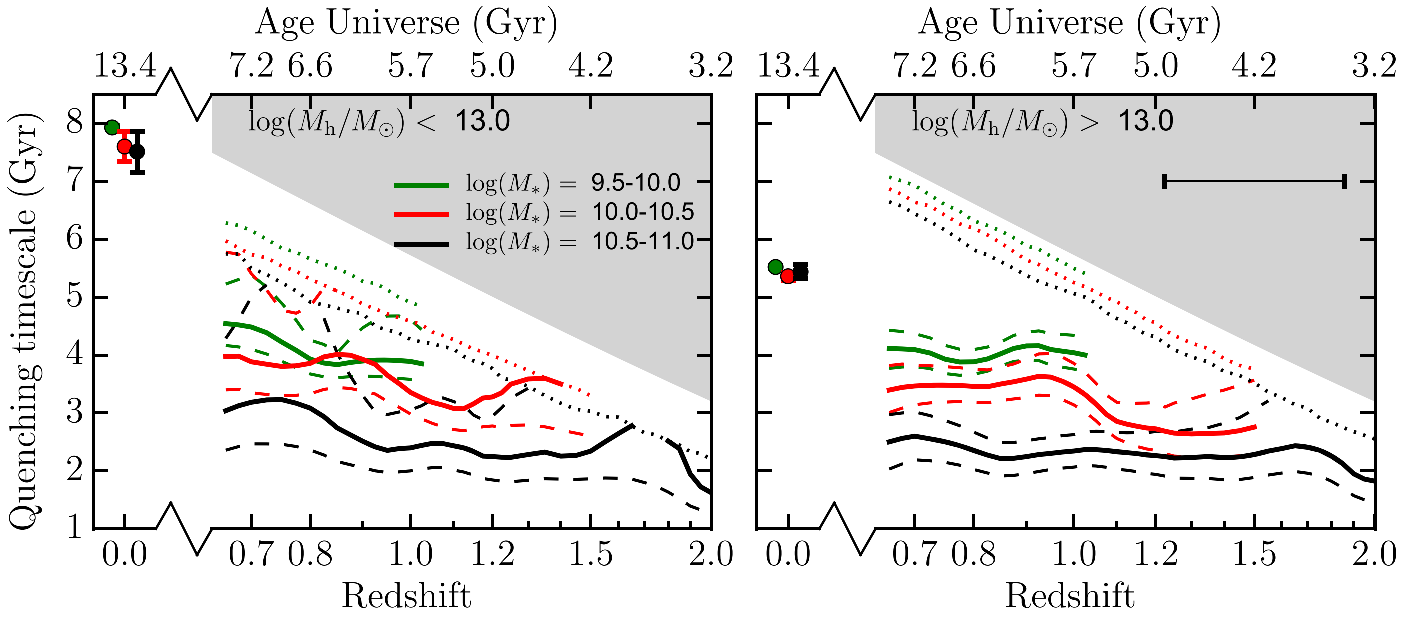

Figure 21. Quenching timescales for satellite galaxies as a function of redshift in bins of M_* and M_h (solid lines) for the 3D-*HST* sample. Dashed lines mark the 1σ confidence levels. The horizontal error bar is the span of the redshift bins (for the 3D-*HST* sample), which is constant in $\Delta z/(1+z) = 0.2$, where Δz is the width of the redshift bin and z its center. Data points at $z = 0$ are from the SDSS sample. The area where T_quench is larger than the Hubble time is shaded in gray. Dotted lines are obtained from the 99th percentile of T_sat in the mock sample and represent the look-back time at which the first 1% of the satellite population at a given redshift was accreted onto more massive halos as satellites. We define this limit as the maximum value of T_quench that would produce a meaningful environmentally quenched satellite population at any given redshift.

is drawn from SDSS and the mock sample from the redshift zero snapshot of the Henriques et al. (2015) model. We describe the details of how those data sets are processed in Appendix D. For this sample, we restrict to stellar masses above $10^{9.5}\ M_\odot$ to avoid including low mass galaxies with large V_max corrections.

The evolution of f_conv as seen in Figure 18 is now clearly visible over the large redshift range probed by 3D-*HST*. The fraction of environmentally quenched satellite galaxies is a function of M_h, M_*, and redshift. At fixed redshift, f_conv is higher for higher mass galaxies, and at fixed stellar mass it is higher in more massive halos. More notably, the redshift evolution follows a decreasing trend with increasing redshift such that at $z \sim 1.5$ the excess of quenching of satellite galaxies becomes more marginal (at least for massive galaxies) as first predicted by McGee et al. (2009) using halo accretion models. Several observational works reached a similar conclusion. Kodama et al. (2004), De Lucia et al. (2007), Rudnick et al. (2009), and Raichoor & Andreon (2012) found a significant build-up of the faint end of the red sequence (of passive galaxies) in cluster environments from $z \sim 1$ toward lower redshift. This implies an increase in the fraction of quenched satellites, with decreasing redshift for low mass galaxies. Recently, Darvish et al. (2016) found that the environmental quenching efficiency tends to zero at $z > 1$, although their analysis is only based on local overdensity and does not separate centrals and satellites. With the 3D-*HST* data set we cannot rule out that satellite quenching is still efficient for lower mass satellites at $z > 1.5$; deeper samples are required to robustly assess the satellite quenching efficiency at $z \sim 1.5$–2.0.

Moving to the present day universe (SDSS data) does not significantly affect the fraction of environmentally quenched satellites, despite the age of the universe nearly doubling compared to the lowest redshift probed by the 3D-*HST* sample.

The redshift dependence of the quenching timescale originates from the combination of the evolution of f_conv and the distributions of infall times for satellite galaxies. The redshift evolution of f_conv in the high halo mass bin is well matched by the halo assembly history (at lower redshift they have been satellites on average for more time), and therefore T_quench is mostly independent of redshift. However, for lower mass galaxies a mild redshift evolution of T_quench might be present. However the slope is much shallower than the ageing of the universe. For this reason, going to higher redshift, T_quench approaches the Hubble time and the satellite quenching efficiency decreases.

Despite the large uncertainty on the quenching times at low halo mass, their redshift evolution appears to be largely independent of halo mass. This means that the halo mass dependence of the conversion fractions may be mostly driven by an increase in the time spent as satellites in more massive halos. At $z = 0$ a more significant difference is found between the quenching times in the two halo mass bins. In the next section we discuss which mechanism can produce these observational signatures.

8. Discussion

There is a growing consensus that the evolution of central galaxies is regulated by the balance between cosmological accretion, star formation, and gas ejection processes in a so-called equilibrium growth model (e.g., Lilly et al. 2013). The reservoir of cold gas in each galaxy is replenished by accretion, and will fuel star formation. As the rate of cosmological accretion is correlated with the mass of the halo, this regulates mass growth via star formation. As a result the eventual stellar mass is also tightly correlated with halo mass, driving a tight relation between star formation rate and stellar mass for normal star-forming galaxies (the main sequence, MS, of star-forming galaxies; e.g., Noeske et al. 2007).

When galaxies fall into a more massive halo, the accretion of new gas from the cosmic web is expected to cease; such gas will instead be accreted (and shock heated) when it reaches the parent halo (White & Frenk 1991). More recently, Dekel & Birnboim (2006) estimate that this process occurs at a minimum halo mass $M_h \sim 10^{12}\,M_{\odot}$, which is largely independent of redshift. This roughly corresponds to the minimum halo mass at which satellites are detected in the 3D-*HST* survey (see Figure 15).

8.1. Identification of the Main Mechanism

There are several additional ways in which a satellite galaxy's gas and stellar content can be modified through interaction with its environment, including stripping of the hot or cold gas, and tidal interactions among galaxies or with the halo potential itself. An important combined effect is to remove (partially or completely) the gas reservoir leading to the quenching of star formation. However, as pointed out by McGee et al. (2014) and Balogh et al. (2016), it might not be necessary to invoke these mechanisms of environmental quenching to be effective. The high SFR typical of galaxies at high redshift, combined with outflows, can lead to exhaustion of the gas reservoir in the absence of cosmological accretion.

Our approach to link the conversion fractions to the distributions of time spent as satellite is based on the assumption that a galaxy starts to experience satellite specific processes at the time of its first infall into a larger halo and, in particular, that the cosmological accretion is shut off at that time.

We now examine whether a pure exhaustion of the gas reservoir can explain the quenching times we observe, or whether additional gas-removal mechanisms are required. First we appeal to the similarity of quenching times in the two halo mass bins shown in Figure 21 to support the pure gas exhaustion scenario. Other than at $z = 0$, the derived quenching times are indeed consistent within the uncertainties; therefore the main quenching mechanism has to be largely independent of halo mass.

Ram pressure stripping is often invoked as the main quenching mechanism for satellite galaxies in low redshift clusters (e.g., Poggianti et al. 2004; Gavazzi et al. 2013; Boselli et al. 2014b). Its efficiency is a function of the intracluster medium (ICM) density and the velocity of galaxies in the halo. More massive halos have a denser ICM, and satellites move faster through it, which exerts a stronger dynamical pressure on the gas leading to faster stripping (and shorter quenching times) in more massive halos (Vollmer et al. 2001; Roediger & Hensler 2005). Our 3D-*HST* data set does not extend to the extreme high mass end of the halo mass function, in which ram pressure effects have been clearly observed (e.g., Sun et al. 2007; Yagi et al. 2010; Merluzzi et al. 2013; Kenney et al. 2015; Fossati et al. 2016), and so the lack of significantly shorter quenching times in the higher halo mass bin is consistent with the lack of stripping, and indeed of any strong halo-mass-dependent gas-stripping process. However, Balogh et al. (2016) find a small halo mass dependence of the quenching times comparing their GEEC2 group sample ($M_h \sim 10^{13.5}\,M_{\odot}$) to the GCLASS cluster sample ($M_h > 10^{14}\,M_{\odot}$). These evidences might indicate that dynamical stripping can play a minor role in more massive halos even at $z \sim 1$.

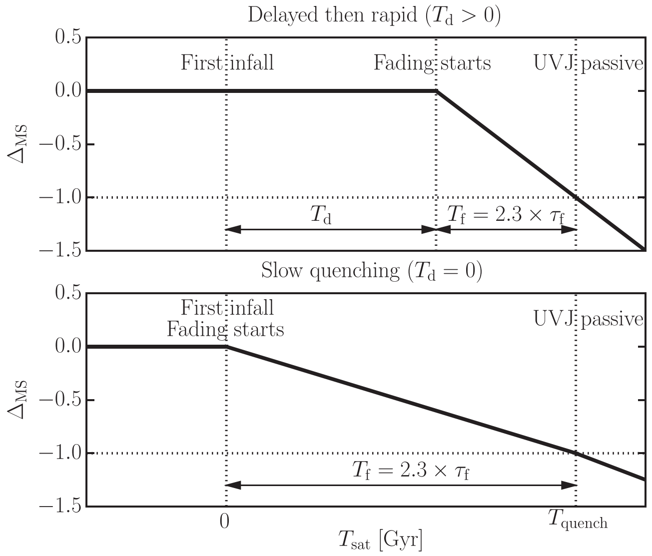

Figure 22. Schematic diagram of the evolution of the MS offset for two toy models of satellite quenching as a function of the time spent as a satellite. In both cases, satellite quenching starts at the time of first infall for a galaxy at the main sequence mid-line value, which becomes UVJ passive after $T_{\rm quench}$. In the "delayed then rapid" model (top panel) the satellite galaxies evolve on the main sequence for a delay time $T_{\rm d}$. Then their SFR drops exponentially with a characteristic timescale τ_f. In the "slow quenching" model (bottom panel), $T_{\rm d} = 0$ and the galaxy follows a slow(-er) exponential decline of the SFR immediately after its first infall into a more massive halo.

At $z = 0$ instead, thanks to the large area covered by the SDSS data set, a number of very massive halos are included in the higher halo mass bin. This combined with the presence of hot and dense ICM in massive halos in the local universe might be sufficient to explain the shorter quenching times in the high halo mass bin. Haines et al. (2015) and Paccagnella et al. (2016) found quenching timescales that are possibly shorter in massive clusters of galaxies (∼2–5 Gyr). Even shorter quenching times are found by Boselli et al. (2016) in the densest region of the Virgo cluster. However, a quantitative comparison is hampered by the different definitions of the quenching timescale.

8.2. Delayed then Rapid or Continuous Slow Quenching?

Having ruled out gaseous stripping as the main driver of satellite quenching in the range of halo mass commonly probed by our samples ($M_h \lesssim 10^{14}\,M_{\odot}$), we now concentrate on how the gas exhaustion scenario can explain the observed values of $T_{\rm quench}$.

To explain the quenching times at $z = 0$, Wetzel et al. (2013) presented a model dubbed the "delayed then rapid" quenching scenario, shown in the top panel of Figure 22. This model assumes that $T_{\rm quench}$ can be divided into two phases. During the first phase, usually called the "delay time" (T_d), the star formation activity of satellites on average follows the MS of central galaxies. After this phase, the star formation rate drops rapidly, and satellite galaxies become passive on a short timescale, called the "fading time." Wetzel et al. (2013) estimated an exponential fading with a characteristic timescale

$\tau_f \sim 0.3$–0.8 Gyr that depends on stellar mass at $z = 0$. At $z \sim 1$, Mok et al. (2014), Muzzin et al. (2014), and Balogh et al. (2016) estimated the fading time to be $\tau_f \sim 0.4$–0.9 Gyr, by identifying a "transition" population of galaxies likely to be transitioning from a star-forming to a passive phase. These values suggest little redshift evolution of the fading timescale with cosmic time.

McGee et al. (2014) developed a physical interpretation of this model. These authors assumed that the long delay times are only possible if the satellite galaxy has maintained a multi-phase reservoir that can cool onto the galaxy and replenish the star-forming gas (typically molecular) at roughly the same rate as the gas is lost to star formation (and potentially outflows). A constant molecular gas reservoir produces a nearly constant SFR according to the Kennicutt–Schmidt relation (Schmidt 1959; Kennicutt 1998b). Then the eventual depletion of this cold gas results in the rapid fading phase.

An alternative scenario would be that satellite galaxies retain only their molecular gas reservoirs after infall. In this case, if we assume a constant efficiency for star formation, we should expect a star formation history that immediately departs from the MS, declining exponentially as the molecular gas is exhausted (the "slow quenching" model shown in the bottom panel of Figure 22). By using our data, we directly test those two toy models.

We use the star formation rates ($\mathrm{SFR}(M_*, z)$) for 3D-*HST* galaxies presented in the Momcheva et al. (2016) catalog. By limiting to galaxies in the redshift range $0.5 < z < 1.5$, stellar mass range $9.5 < \log(M_*) < 11$, and a maximum offset below the main sequence of 0.5 dex, we make sure that the SFR estimates are reliable and, for 91% of the objects, are obtained from *Spitzer* 24 μm observations combined with a UV monochromatic luminosity to take into account both dust obscured and unobscured star formation. For the remaining 9%, SFR estimates are from an SED fitting procedure (see Whitaker et al. 2014; Momcheva et al. 2016).

There is growing evidence of curvature in the MS, which becomes shallower at higher stellar mass. Whitaker et al. (2014), Gavazzi et al. (2015), and Erfanianfar et al. (2016) interpreted this as a decline in star formation efficiency caused by the growth of bulges or bars in massive galaxies. To study the effects of environment above the internal processes driving the star formation efficiency at fixed stellar mass, we convert the SFR into an offset from this curved MS: $\Delta_{\mathrm{MS,obs}} = \log(\mathrm{SFR}(M_*, z)/\mathrm{SFR}_{\mathrm{MS}}(M_*, z)$, using the Wisnioski et al. (2015) parameterization of the MS from Whitaker et al. (2014).

In order to test the two models we again resort to the mock sample. For each central galaxy in the mocks we assign a random offset from the main sequence obtained from a pure sample ($P_{\mathrm{cen}} > 0.8$) of observed centrals: $\Delta_{\mathrm{MS,cen}}$. For satellite galaxies, instead, their Δ_{MS} is a function of their time spent as satellites (T_{sat}) as follows:

$$\Delta_{\mathrm{MS}} = \begin{cases} < -1 & \text{if } T_{\mathrm{sat}} > T_{\mathrm{quench}} \\ \Delta_{\mathrm{MS,cen}} & \text{if } T_{\mathrm{sat}} \leqslant T_{\mathrm{d}} \\ \Delta_{\mathrm{MS,cen}} + \log(e^{-(T_{\mathrm{sat}} - T_{\mathrm{d}})/\tau_f}) & \text{if } T_{\mathrm{sat}} > T_{\mathrm{d}} \end{cases}, \quad (18)$$

where T_{quench} and T_{d} are the total quenching time and the delay time, respectively, and τ_f is the characteristic timescale of the exponential fading phase. The latter is computed for each galaxy independently such that the SFR drops 1 dex below the MS[14] in ($T_{\mathrm{quench}} - T_{\mathrm{d}}$) Gyr. As we already computed T_{quench}, the only free parameter remaining in this family of models is T_{d}. We define the "slow quenching" model for $T_{\mathrm{d}} = 0$, and "delayed then rapid" for those where $0 < T_{\mathrm{d}} < T_{\mathrm{quench}}$.

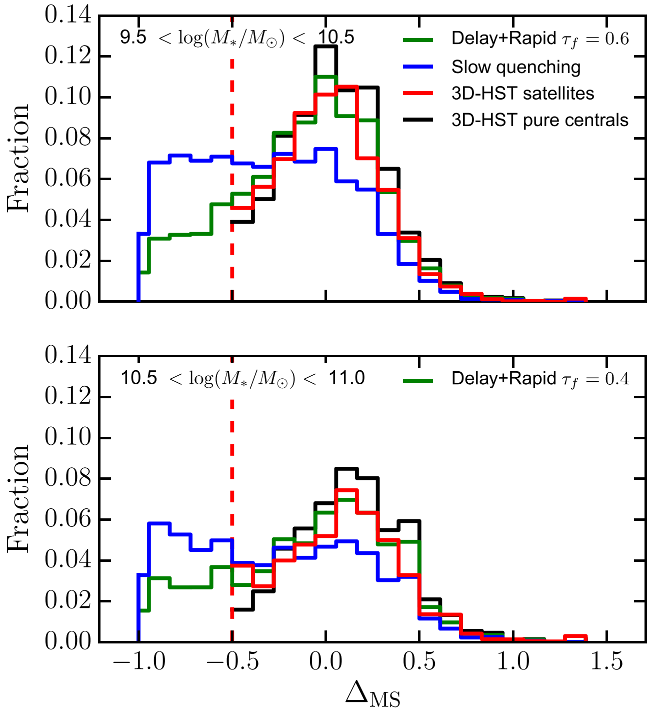

Figure 23. Logarithmic offset from the main sequence (Δ_{MS}) in two stellar mass bins for 3D-*HST* observed satellites at $0.5 < z < 1.5$ (red histogram) and for mock galaxies, in the same redshift range, assuming a "slow quenching" (blue histogram), or a "delayed then rapid" (green histogram) scenario (see text for the details of those two toy models). The histograms are normalized to the total number of 3D-*HST* satellites (including UVJ passive galaxies). The main sequence offset of a pure sample of observed central galaxies (black histogram) is shown for comparison. The red vertical dashed line is the limit below the main sequence at which SFR estimates for observed galaxies are based predominantly on accurate IR+UV measurements accounting for obscured and unobscured star formation.

Figure 23 shows the distributions of Δ_{MS} for 3D-*HST* satellites in two stellar mass bins, obtained as usual by weighting all galaxies by P_{sat}, and for the two models obtained from the mock sample in the same way. The histograms are normalized to the total number of 3D-*HST* satellites in the same stellar mass bin (including UVJ passive galaxies). We stress that this comparison is meaningful because our models include the cross-talk between centrals and satellites.

In the "delayed then rapid" scenario, the value of the delay time that best reproduces the observed data is $T_{\mathrm{d}} = T_{\mathrm{quench}} - 1.4(0.9)$ Gyr for the $10^{9.5}$–$10^{10.5}$ ($10^{10.5}$–10^{11}) stellar mass bins, respectively. This means the average satellite fades with an *e*-folding timescale of $\tau_{\mathrm{f}} = 0.6(0.4)$ Gyr. Our values are consistent with those from Wetzel et al. (2013) at $z = 0$ and other independent estimates at high-z. Tal et al. (2014) performed a statistical identification of central and satellite galaxies in the UltraVISTA and 3D-*HST* fields and found that the onset of satellite quenching occurs 1.5–2 Gyr later than that of central galaxies at fixed number density.

---

[14] This is the value that defines the typical division between UVJ star-forming and passive objects.

These values are in good agreement with the delay times estimated in our work.

Conversely the "slow quenching" model predicts too many galaxies below the main sequence, but which are not UVJ passive ("transition" galaxies). The fraction of 3D-*HST* satellites for which $\Delta_{\rm MS} > -0.5$ is 65% (46%), which compares to 67% (47%) for the "delayed then rapid" model; instead it drops to 52% (39%) for the "slow quenching" model.

We tested that the distributions of $\Delta_{\rm MS}$ and the estimated fading times are not biased by inaccurate UV+IR SFR for AGN candidates in the sample. Because the CANDELS fields have uniform coverage of deep *Spitzer*/IRAC observations, we remove the sources selected by the IRAC color–color criteria presented in Donley et al. (2012). We find that neither the $\Delta_{\rm MS}$ distributions nor the fading time estimates change appreciably.

In conclusion the fading of the star formation activity must be a relatively rapid phenomenon that follows a long phase where satellite galaxies have an SFR which is indistinguishable from that of centrals. This is further supported by the evidence that the passive and star-forming populations are well separated in color and SFR, and that the "green valley" in between them is sparsely populated across different environments (Gavazzi et al. 2010; Boselli et al. 2014b; Mok et al. 2014; Schawinski et al. 2014).

8.3. The Gas Content of Satellite Galaxies

Finally, we discuss the implications of the quenching times on the gas content of satellites at the time of infall. Because satellite galaxies are not thought to accrete gas after infall, their continued star formation occurs at the expense of gas previously bound to the galaxy.

As previously discussed, McGee et al. (2014) explain the fading phase by the depletion of molecular gas. The depletion time of molecular gas ($T_{\rm depl,\,H_2}$) has been derived by several authors (Saintonge et al. 2011; Tacconi et al. 2013; Boselli et al. 2014a; Genzel et al. 2015). There is general consensus that this timescale (which is an *e*-folding time) is ~1.5 Gyr at $z = 0$ and is ~0.75 Gyr at $z = 1$. Moreover, it is independent of stellar mass. In this framework we might expect fading times shorter than (or similar to) $T_{\rm depl,\,H_2}$, where shorter fading times are possible where a fraction of the gas is lost to outflows. Our fading times are indeed somewhat shorter than the molecular gas depletion times, consistent with this picture, but with a mass dependence that suggests a mass-dependent outflow rate.

In Figure 24 we show the ratio of the delay time to the fading time as a function of redshift in bins of stellar mass. Assuming that the fading phase is driven by depletion of molecular gas (in absence of further replenishment), this ratio informs us about the relative time spent refuelling the galaxy to keep it on the MS (from a gas reservoir initially in a warmer phase) to the time spent depleting the molecular gas. We note that the delay time is estimated via the quenching time (which is a function of stellar mass and redshift), while the fading time is computed only for two stellar mass bins at $0.5 < z < 1.5$, with $z = 0$ fading timescales taken from Wetzel et al. (2013). Errors in Figure 24 propagate only the errors on the total quenching time.

For all stellar mass bins, this ratio is above unity, which we interpret to mean that gas in a non-molecular phase is required to supply fuel for star formation, and this gas is likely to exceed the molecular gas in mass. The longer delay times at $z = 0$ suggest that a smaller fraction of the gas mass is in molecular form. This model also implies that a significant fraction of the final stellar mass of satellite galaxies is built up during the satellite phase.

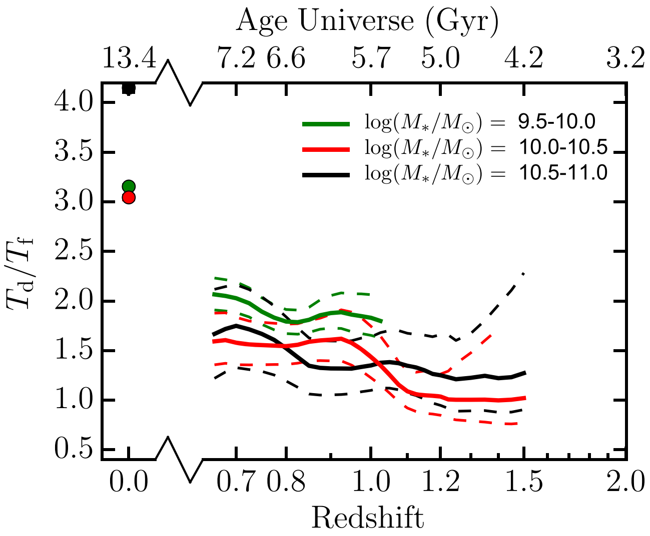

Figure 24. Ratio of the delay time ($T_{\rm d}$) to the fading time ($T_{\rm f}$) as a function of redshift in bins of stellar mass. The values of $T_{\rm f}$ at $z > 0.5$ are derived in Section 8.2, while those at $z = 0$ are taken from Wetzel et al. (2013). The uncertainties on the ratio propagate only the errors on the total quenching time.

A multi-phase gas reservoir is observed in the local universe in the form of ionized, atomic, and molecular hydrogen. Atomic hydrogen cools, replenishing the molecular gas reservoir that is depleted by star formation. In the local universe, using the scaling relations derived from the *Herschel* Reference Sample (Boselli et al. 2014a), the observed mass of atomic hydrogen is found to be two to three times larger than the amount of molecular hydrogen for our most massive stellar mass bin. This ratio increases to ~8 for the lower mass objects, although with a large uncertainty. These numbers are consistent with the picture that much, if not all, of the reservoir required to maintain the satellite on the MS during the delay phase at $z \sim 0$ can be (initially) in an atomic phase. It is also plausible that much of the gas reservoir bound to higher redshift galaxies is contained in a non-molecular form, and that this can be retained and used for star formation when the galaxies become satellites.

Assuming that outflows are not only active during the fading phase but rather during the entire quenching time, the mass in the multi-phase gas reservoir needs to be even larger, although it is not straightforward to constrain by how much.

In conclusion, our work supports a "delayed then rapid" quenching scenario for satellite galaxies, regulated by star formation, depletion, and cooling of a multi-phase gas reservoir.

9. Conclusions

In this work, we have characterized the environment of galaxies in the 3D-*HST* survey at $z = 0.5$–3.0. We used the projected density within fixed apertures, coupled with a newly developed method for edge corrections, to obtain a definitive measurement of the environment in five well studied deep fields: GOODS-S, COSMOS, UDS, AEGIS, and GOODS-N. Using a recent semi-analytic model of galaxy formation, we have assigned physical quantities describing the properties of dark matter halos to observed galaxies. Our results can be summarized as follows:

1. The 3D-*HST* deep fields host galaxies in a wide range of environments, from underdense regions to relatively massive clusters. This large variety is accurately quantified thanks to a homogeneous coverage of high quality redshifts provided by the 3D-*HST* grism observations.
2. As described in Fossati et al. (2015), a calibration of density into physically motivated quantities (e.g., halo mass, central/satellite status) requires a mock catalog tailored to match the properties of the 3D-*HST* survey. We developed such a catalog and performed a careful match to the observational sample. As a result each 3D-*HST* galaxy is assigned a probability that it is a central or satellite galaxy with an associated probability distribution function of halo mass for each type. This Bayesian approach naturally takes into account sources of contamination in the matching process. We publicly release our calibrated environment catalog to the community.
3. The 3D-*HST* sample provides us with a unique data set to study the processes governing environmental quenching from $z\sim2$ to the present day over a wide range of halo mass. As no galaxy has a perfectly defined environment, a Bayesian analysis including forward modeling of the mock catalog allows us to recover "pure" passive fractions of central and satellite populations. We also estimated robust and realistic uncertainties through a Monte Carlo error propagation scheme that takes into account the use of probabilistic quantities.
4. By computing conversion fractions (i.e., the excess of quenched satellite galaxies compared to central galaxies at the same epoch and stellar mass; van den Bosch et al. 2008), we find that satellite galaxies are efficiently environmentally quenched in halos of any mass up to $z\sim1.2$–1.5. Above these redshifts, the fraction of passive satellites is roughly consistent with that of central galaxies.
5. Under the assumption that the earliest satellites to be accreted become passive first, we derive environmental quenching timescales. These are long (∼2–5 Gyr at $z\sim0.7$–1.5; 5–7 Gyr at $z=0$) and longer at lower stellar mass. As they become comparable to the Hubble time by $z\sim1.5$, effective environmental quenching of satellites is not possible at earlier times. More remarkably, their halo mass dependence is negligible. By assuming that cosmological accretion stops when a galaxy becomes a satellite, we were able to interpret these evidences in a "gas exhaustion" scenario (i.e., the "overconsumption" model of McGee et al. 2014), where quenching happens because satellite galaxies eventually run out of their fuel which sustains further star formation.
6. We tested two toy models of satellite quenching: the "delayed then rapid" quenching scenario proposed by Wetzel et al. (2013) and a continuous "slow quenching" from the time of first infall. By comparing the observed SFR distribution for 3D-*HST* satellites to the predictions of these toy models, we found that the scenario that best reproduces the data at $z\sim0.5$–1.5 is "delayed then rapid." Consistent with the results of Wetzel et al. (2013) at $z=0$, we find that the fading of the star formation activity is a relatively rapid phenomenon ($\tau_{\rm f}\sim0.4$–0.6 Gyr, lower at higher mass) that follows a long phase where satellite galaxies have an SFR that is indistinguishable from that of centrals.
7. By linking the fading to the depletion of molecular gas, we conclude that the "delayed then rapid" scenario is best explained, even at high redshift, by the presence of a significant multi-phase reservoir that can cool onto the galaxy and replenish the star-forming gas at roughly the same rate as the gas is turned into stars.

This analysis of satellite quenching is only one of many possible analyses that can be performed with the environmental catalog built in this work. In the future, the advent of the *James Webb Space Telescope, WFIRST*, and *Euclid* space missions, as well as highly multiplexed spectroscopic instruments from the ground (e.g., *MOONS* at VLT; *PFS* at *Subaru*), will provide excellent redshift estimates for fainter objects over a much larger area, to which similar techniques to calibrate environment can be applied. This in combination with deeper scaling relations for the atomic and molecular gas components from the *Square Kilometer Array* and *ALMA* will revolutionize measurements to constrain how galaxies evolve and quench as a function of their environment.

It is a pleasure to extend our thanks to Nikhil Arora for his help in a preliminary examination of the local SDSS data; to Alessandro Boselli, Gabriella de Lucia, Sean McGee, Greg Rudnick, and Andrew Wetzel for useful discussion; to Michael Balogh and Alexis Finoguenov for providing catalogs in useful format; and to Stefano Zibetti and Tamás Budavári for their work in helping derive densities for the SDSS sample, as presented in Wilman et al. (2010) and Phleps et al. (2014). We thank the anonymous referee for his/her comments that improved the quality of the manuscript.

M.F. and D.J.W. acknowledge the support of the Deutsche Forschungsgemeinschaft via Projects WI 3871/1-1, and WI 3871/1-2. J.C.C.C. acknowledges the support of the Deutsche Zentrum für Luft- und Raumfahrt (DLR) via Project ID 50OR1513. K.E.W. gratefully acknowledges support by NASA through Hubble Fellowship grant #HF2-51368 awarded by the Space Telescope Science Institute, which is operated by the Association of Universities for Research in Astronomy, Inc., for NASA.

This work is based on observations taken by the 3D-*HST* Treasury Program (GO 12177 and 12328) with the NASA/ESA *HST*, which is operated by the Association of Universities for Research in Astronomy, Inc., under NASA contract NAS5-26555.

This work is based on observations made with ESO Telescopes at the La Silla or Paranal Observatories under programme ID(s) 175.A-0839(B), 175.A-0839(D), 175.A-0839(I), 175.A-0839(J), 175.A-0839(H), 175.A-0839(F), 092.A-0091, 093.A-0079, 093.A-0187, 094.A-0217, 094.A-0287, 095.A-0047, 095.A-0109, 096.A-0093, and 096.A-0025.

The MOSDEF data were obtained at the W.M. Keck Observatory, which is operated as a scientific partnership among the California Institute of Technology, the University of California, and the National Aeronautics and Space Administration. The observatory was made possible by the generous financial support of the W.M. Keck Foundation. We recognize and acknowledge the very significant cultural role and reverence that the summit of Maunakea has always had within the indigenous Hawaiian community. We are most fortunate to have the opportunity to conduct observations from this mountain.

We acknowledge all the teams and observatories that provided data sets included in the photometric and spectroscopic catalogs used in this work.

Funding for SDSS-III has been provided by the Alfred P. Sloan Foundation, the participating institutions, the National Science Foundation, and the U.S. Department of Energy Office of Science. The SDSS-III website is http://www.sdss3.org/.

SDSS-III is managed by the Astrophysical Research Consortium for the Participating Institutions of the SDSS-III Collaboration, including the University of Arizona, the Brazilian Participation Group, Brookhaven National Laboratory, Carnegie Mellon University, University of Florida, the French Participation Group, the German Participation Group, Harvard University, the Instituto de Astrofisica de Canarias, the Michigan State/Notre Dame/JINA Participation Group, Johns Hopkins University, Lawrence Berkeley National Laboratory, Max Planck Institute for Astrophysics, Max Planck Institute for Extraterrestrial Physics, New Mexico State University, New York University, Ohio State University, Pennsylvania State University, University of Portsmouth, Princeton University, the Spanish Participation Group, University of Tokyo, University of Utah, Vanderbilt University, University of Virginia, University of Washington, and Yale University.

Appendix A
Extended Catalogs for Edge Corrections in the GOODS-S, COSMOS, and UDS Fields

A.1. GOODS-S

The GOODS-S field is part of a larger field known as the Extended *Chandra* Deep Field South (ECDFS, Lehmer et al. 2005). This field has been covered by the Multiwavelength Survey by Yale-Chile (MUSYC, Gawiser et al. 2006) in 32 broad and medium bands from the optical to the medium infrared wavelengths. The broadband data originate from various sources (Arnouts et al. 2001; Moy et al. 2003; Taylor et al. 2009), and a consistent reduction and analysis is performed by the MUSYC team (Cardamone et al. 2010). The source extraction is performed on a deep combined image of three optical filters (*BVR*) and reaches a depth of ∼25.5 mag. Stars are removed from the catalog by using the `star_flag` parameter.

In order to select galaxies in a consistent way as for 3D-*HST*, we need deep observations in a filter with a central wavelength as close as possible to that of WFC3/F140W (1.4 μm). However, the near-infrared observations from MUSYC are shallow and only reach a depth of $J = 22.4$ mag. We therefore match the MUSYC catalog with the Taiwan ECDFS Near-Infrared Survey (TENIS; Hsieh et al. 2012). This survey provides deep *J* and *K* images of the ECDFS area, with limiting magnitudes of 24.5 and 23.9, respectively. Hereafter, where sky coordinates matching between different catalogs are required, we select the closest match within a 1 arcsec radius. The comparison of *J* band magnitudes from the two surveys for sources above the sensitivity limit of the MUSYC data shows a remarkable agreement. We then match the MUSYC and 3D-*HST*/GOODS-S catalog, again by sky coordinates. Using the galaxies that are present in both surveys, we fit a linear function between JH_{140} and $J_{\rm TENIS}$ magnitudes. Given the significant overlap between the filters, we neglect color terms in the fit. The best bisector fit (Isobe et al. 1990) is $JH_{140} = 0.99 \times J_{\rm TENIS} + 0.22$. Then we use this function to generate JH_{140} magnitudes for all objects in the MUSYC+TENIS catalog.

We evaluate the depth of the resulting catalog by inspecting the histogram of the number counts in the JH_{140} band. Since this is obtained from deep $J_{\rm TENIS}$ data (24.5 mag), the limiting factor will be the depth of the *BVR* selection band of MUSYC. The number counts increase linearly in log space up to $JH_{140} \sim 23.5$, and we therefore adopt this value for the selection. Since this limit is brighter than the one we set for the primary sample in 3D-*HST*, a fraction of the neighbors are missed. We correct for this by assigning to each MUSYC galaxy in Equation (1) a weight $w = 1.42$ that corresponds to the ratio of the cumulative luminosity function at $JH_{140} = 23.5$ and $JH_{140} = 24$ mag from the deeper 3D-*HST* catalog.

The most recent calculation of photometric redshifts in ECDFS is presented by Hsu et al. (2014). These authors combined the MUSYC photometry with TENIS and *HST*/CANDELS (Guo et al. 2013b) in the GOODS-S area. We match our catalog with their catalog based on MUSYC ID, and we find a match for each source. Hsu et al. (2014) also present a compilation of spectroscopic redshifts available in the literature, which we use whenever available. Photo-*z*s are computed using *LePhare* (Arnouts et al. 1999; Ilbert et al. 2006), and their accuracy depends primarily on the availability and depth of multiwavelength photometry. The GOODS-S area has deep *HST* coverage from CANDELS, but those galaxies are already present in our primary 3D-*HST* catalog. Therefore we are primarily interested in sources outside the CANDELS/3D-*HST* area. In the ECDFS footprint, which is not covered by *HST*, more than 30 photometric bands are available and photo-*z*s are quite accurate[15]: $\sigma_{\rm NMAD} \sim 3000\,(4000)$ km s^{-1} for galaxies with $H < 23\,(H > 23)$, respectively. These values degrade where continuum spectral features (e.g., Balmer break) are redshifted outside the range observed with medium band filters ($z > 1.5$), although low number statistics hamper a robust determination of the photometric redshift quality.

Stellar masses are computed using the photometric data and the redshift information by choosing the same grid of templates used by Skelton et al. (2014) for the 3D-*HST* fields. We assess the quality of the stellar masses by comparing to those from Skelton et al. (2014), where MUSYC and 3D-*HST* overlap, and we find a median offset of 0.01 dex and a scatter of 0.15 dex. The scatter is driven by the scatter in photometric redshifts in the two catalogs.

As a last step we remove from this catalog galaxies in the 3D-*HST* footprint that satisfy the selection criteria for the primary environment sample, to obtain a pure catalog that we use only for the edge corrections.

A.2. COSMOS

The entire COSMOS 2deg^2 field has been observed in 30 photometric bands from UV to medium infrared (including several medium bands; Sanders et al. 2007; Taniguchi et al. 2007; Erben et al. 2009; Bielby et al. 2012). Photometric

---

[15] We measure the photo-*z* accuracy using the normalized median absolute deviation (NMAD): $\sigma_{\rm NMAD} = 1.48 \times {\rm median}(|\Delta z|/(1 + z))$, where Δz is the difference between the spectroscopic and the photometric redshift.

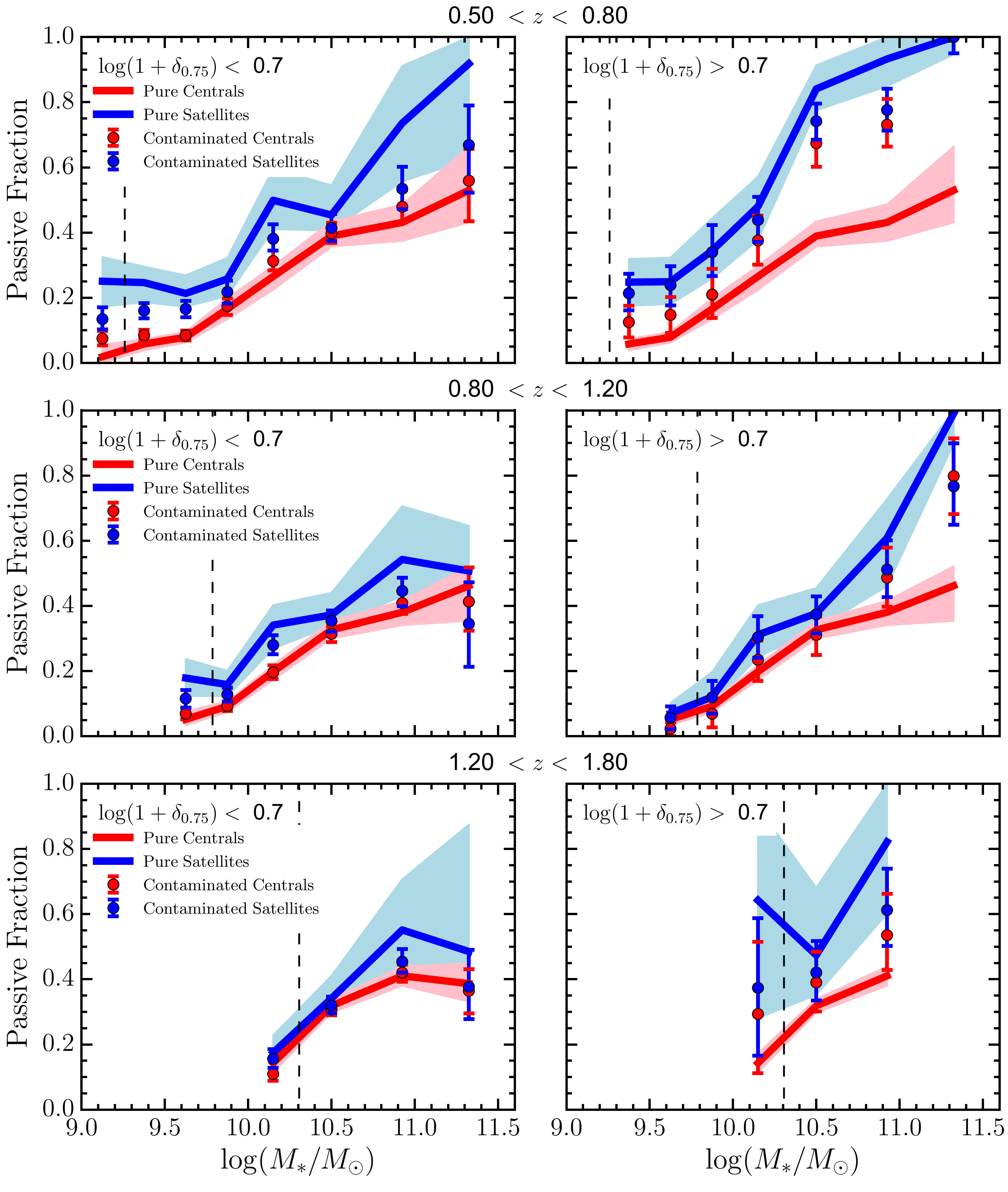

Figure 25. Passive fraction for central and satellite galaxies in bins of $M_{\rm star}$, density contrast $\log(1 + \delta_{0.75})$, and redshift. Data points are the observed passive fractions with uncertainties derived from Monte Carlo resampling of the mock sample. Thick blue and red lines are the "pure" passive fractions, with 1σ confidence intervals as shaded regions. The vertical dashed line marks the stellar mass of the volume limited sample.

redshifts are computed using *LePhare* and are presented by Ilbert et al. (2009) for sources with $i^+ < 25$ mag. We include spectroscopic redshifts from zCOSMOS-bright (Lilly et al. 2007), where available.

The photometric redshift uncertainty is evaluated by Ilbert et al. (2009), comparing photo-z to spec-z, and is $\sigma_{\rm NMAD} \sim 2100\,(9000)$ km s^{-1} for galaxies with $i^+ < 22.5\,(i^+ > 23)$, respectively. The latter value must be taken with caution, as it is calibrated using a small number of objects. We remake this comparison by using 3D-*HST* spec-z and grism-z as a reference (restricting our analysis to the 3D-*HST*/COSMOS field). We divide the sample into bright ($i^+ < 22.5$ mag) and faint ($i^+ \geqslant 22.5$ mag) for $0.5 < z \leqslant 1.5$, and irrespective of magnitude for $1.5 < z \leqslant 3.0$. We note that for faint sources the effective magnitude limit is that of the grism redshift extraction $JH_{140} < 24$ mag, and the comparison is limited by the degraded accuracy of grism redshifts for faint sources with no emission line detection (see Figure 1). The redshift accuracy is $\sigma_{\rm NMAD} \sim 3000$ (7500) km s^{-1} for the bright (faint) sample at low redshift and $\sigma_{\rm NMAD} \sim 8500$ km s^{-1} for the high redshift sample. Those values are consistent with the determination by Ilbert et al. (2009), and the reduced accuracy at high redshift is due to the lack of narrow bands in the NIR.

To overcome this limitation, the Newfirm Medium Band Survey (NMBS; Whitaker et al. 2011) observed the COSMOS field with five medium band filters in the J and H bands and a broadband filter in K. As a result the accuracy of photometric redshifts is significantly improved (see Section 5 in Whitaker et al. 2011), and we use these photo-z where they are available.

Deep J band magnitudes are provided by the UltraVISTA survey (McCracken et al. 2012). After matching their catalog via sky coordinates, we generate synthetic JH_{140} magnitudes as described in the previous section and using the best fit: $JH_{140} = 0.98 \times J_{\rm UltraVISTA} + 0.31$. The depth of our catalog is limited by the depth of the i^+ selection band from Ilbert et al. (2009). The number counts increase linearly in log space until $JH_{140} \sim 23.0$, and we therefore adopt this value for the selection limit. As for the MUSYC catalog, this limit is brighter than the one we set for the primary sample in 3D-*HST*; therefore we assign to each galaxy in Equation (1) a weight ($w = 2.06$). Stars are removed from the catalog by using the `type` flag from Ilbert et al. (2009).

We compute stellar masses as described in the previous section. The agreement with stellar masses from Skelton et al. (2014) is remarkable, with a median offset of 0.02 dex and a scatter of 0.20 dex. Lastly, we remove the primary 3D-*HST* sources from this edge correction sample.

A.3. UDS

The 3D-*HST* UDS field is part of a larger field known as UKIDSS UDS. This field features deep near-infrared J, H, and K observations with the UKIDSS telescope (O. Almaini et al. 2016, in preparation), complemented by optical and medium infrared data (Furusawa et al. 2008; Ashby et al. 2013).

The UDS/DR8 catalog selection is performed in the K band, and the completeness limit is $K \sim 24.6$ mag. As for the previous fields, we exclude stars and we compute synthetic JH_{140} magnitudes using the best fit relation: $JH_{140} = 0.98 \times J_{\rm UKIDSS} + 0.19$. The depth of our catalog matches the limiting magnitude for the primary 3D-*HST* sample; thus we do not apply any statistical weight for the UKIDSS UDS galaxies when computing the density.

Photometric redshifts (W. Hartley 2016, private communication) have a typical accuracy of $\sigma \sim 9000$ km s^{-1} due to the lack of narrow- or medium band photometry in this field. As for the other fields, we compute stellar masses using the FAST code and find a good agreement with the values from Skelton et al. (2014) for the 3D-*HST*/UDS field, with an offset of −0.03 dex and a scatter of 0.22 dex. Again, the last step is to remove the 3D-*HST* primary sources via positional matching with the Skelton et al. (2014) catalog.

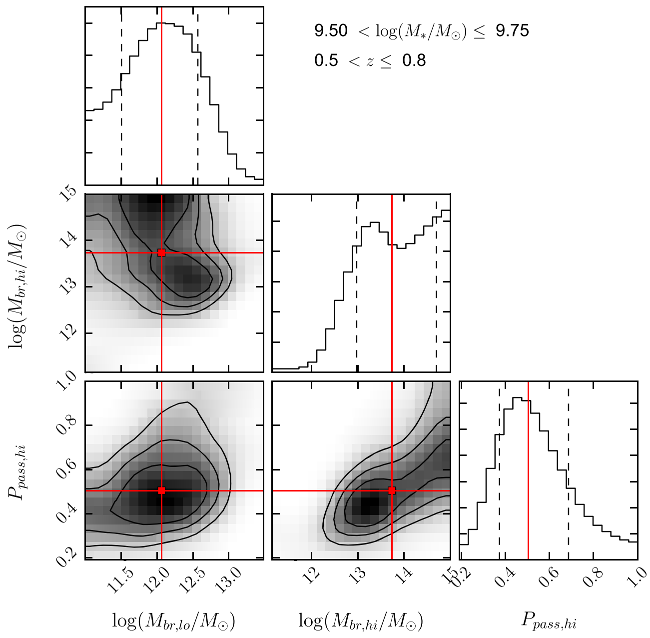

Figure 26. Marginalized likelihood distributions for individual model parameters (panels along the diagonal) and marginalized maps for pairs of parameters, for the stellar mass bin $9.50 < \log(M_*/M_\odot) \leqslant 9.75$ and redshift bin $0.5 < z \leqslant 0.8$. The red lines show the median value for each parameter (which may be distinct from the global maximum likelihood value). The vertical dashed lines in the histograms show the 1σ confidence intervals. The black contours in the two-dimensional maps show the 1σ, 1.5σ, and 2σ confidence intervals.

Appendix B
Passive Fraction as a Function of Density

Halo mass is the parameter that most easily allows the interpretation of environmental effects across cosmic time. It also allows for easier and less biased comparisons across different works. Moreover, it can be directly linked to models (either semi-analytic or hydrodynamical), allowing a better understanding of which physical processes are most relevant at different halo masses. Density, on the other hand, depends on the depth (and to some extent the observing strategy) of each survey. Detailed and quantitative comparisons are also made difficult by different approaches to density (e.g., Haas et al. 2012; Muldrew et al. 2012; Etherington & Thomas 2015). However, it is a parameter directly obtained from the observed redshift space coordinates of the population of galaxies under investigation. In this respect, it is less sensitive to the quality and uncertainties in the calibration of halo mass.

In this appendix we derive the passive fraction of galaxies in two bins of density and compare them to those obtained in Figure 17 using halo mass. The observed fractions of passive centrals and satellites in bins of M_* and density contrast $\log(1 + \delta_{0.75})$ are given by

$$f_{\rm pass|ty} = \frac{\sum_i (\delta_{\rm pass,i} \times \delta_{M_*,\rm i} \times \delta_{\log(1+\delta_{0.75}),i} \times P_{\rm ty,i})}{\sum_i (\delta_{M_*,\rm i} \times \delta_{\log(1+\delta_{0.75}),i} \times P_{\rm ty,i})}, \quad (19)$$

where ty refers to a given type (centrals or satellites), $\delta_{\rm pass,i}$ is 1 if a galaxy is UVJ passive and 0 otherwise, $\delta_{M_*,\rm i}$ is 1

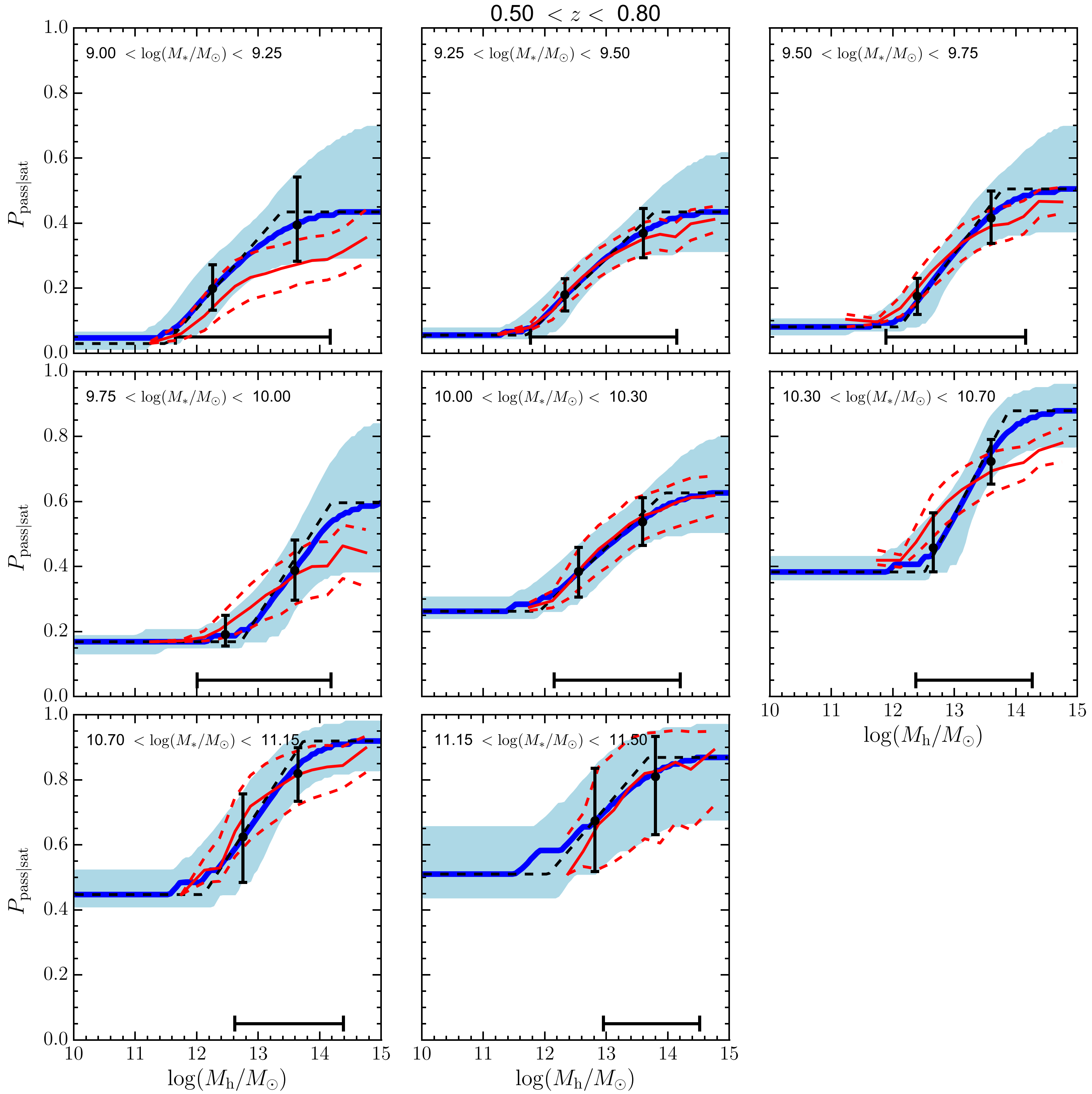

Figure 27. Median (thick blue lines) and 1σ confidence intervals (shaded areas) of the probability that a satellite galaxies is passive ($P_{\rm pass|sat}$) as a function of halo mass from our fitting method in different stellar mass bins at $0.5 < z \leqslant 0.8$. The black dashed line is the best fit model with values obtained from the marginalized distributions in each parameter. The horizontal black lines show the halo mass range that includes 90% of the satellites in each stellar mass bin. The black points with errorbars show the average value of $P_{\rm pass|sat}$ (and its 1σ uncertainty) for galaxies in halos above and below $10^{13} M_\odot$. The red lines are the median prediction (solid) and 1σ confidence intervals (dashed lines) for $P_{\rm pass|sat}$, under the assumption of a quenching timescale independent of halo mass. In most of the stellar mass bins, this assumption well reproduces the best fit of $P_{\rm pass|sat}$.

if a galaxy is in the stellar mass bin and 0 otherwise, $\delta_{\log(1+\delta_{0.75}),i}$ is 1 if a galaxy is in the density bin and 0 otherwise, and $P_{\rm ty,i}$ is the probability that a galaxy is of a given type. In this equation the only uncertain property for each object is its central/satellite status, while the cross-talk between multiple density bins is not present (as it was for halo mass).

We therefore perform a simpler decontamination procedure. For each density, stellar mass, and redshift bin, we assign to real centrals in the mocks a probability of being passive equal to the passive fraction of the pure sample of observed central galaxies $f_{\rm pass|cen,pure}\,(M_*,\,\delta_{0.75})$, while the passive fraction of satellites $f_{\rm pass|sat,pure}\,(M_*,\,\delta_{0.75})$ is a free parameter. Then we use Equation (19) to compute the observed passive fractions for mock galaxies (therefore contaminating the "pure" values). We solve for $f_{\mathrm{pass|sat,pure}}$ (M_*, $\delta_{0.75}$) by maximising the likelihood that the contaminated passive fractions for mock galaxies match the observed passive fractions (jointly for centrals and satellites). This procedure is repeated 500 times in a Monte Carlo fashion in order to propagate the uncertainties on the data points to the "pure" (decontaminated) passive fractions.

The decontaminated values of the passive fraction for centrals and satellites shown in Figure 25 are qualitatively similar to those obtained in bins of halo mass in the same redshift slices (see Figure 17).

We conclude that the dependence of environmental quenching when binned on local density is similar to that in bins of halo mass, where density is a more directly observed quantity.

Appendix C
An Example of the Fitting Procedure to Recover the Passive Fraction of Pure Satellites

In this Appendix we illustrate the results of the fitting process described in Section 7.2 for a single redshift bin.

Figure 26 presents the constraints on the model parameters (marginalized over the nuisance parameter $P_{\mathrm{pass|cen}}$) for a single stellar mass and redshift bin. The panels along the diagonal show the marginalized posterior distributions for each for the three parameters ($M_{\mathrm{br,lo}}$, $M_{\mathrm{br,hi}}$, $P_{\mathrm{pass,hi}}$). The red solid lines show the median value of each parameter, and the black dashed lines show the 1σ confidence intervals. The off-diagonal panels show the marginalized posterior distributions for a pair of model parameters. The black contours show the 1σ, 1.5σ, and 2σ confidence intervals. The fits for the other stellar mass bins give qualitatively similar results.

Figure 27 shows the median value (thick blue lines) of $P_{\mathrm{pass|sat}}$ as a function of log halo mass and 1σ confidence intervals in each stellar mass bin. Despite the significant covariance of the model parameters, the shape of the passive fraction models for satellites is well determined. The horizontal black lines show the halo mass range that includes 90% of the satellites in each stellar mass bin.

The average passive fractions in the two halo mass bins above and below $10^{13}M_\odot$, presented as the thick blue lines in Figure 17, are shown for each stellar mass bin in Figure 27 by the black points.

We add in Figure 27 an additional test of the result presented in Section 7.4 that the quenching time is largely independent of halo mass. We compute a single quenching time per stellar mass bin without binning the data in halo mass. Then we compute which fraction of mock galaxies have $T_{\mathrm{sat}} > T_{\mathrm{quench}}$ as a function of halo mass. This is converted in a probability of being passive as a function of halo mass, which we show as solid red lines (with 1σ confidence intervals as dashed lines) in Figure 27. The agreement with the best fit values of $P_{\mathrm{pass|sat}}$ is remarkable in most of the stellar mass bins, further supporting the result of a quenching timescale that is independent of halo mass.

Appendix D
A $z = 0$ Sample from SDSS

D.1. Observational Data

The $z = 0$ points in Figures 20 and 21 are obtained from a sample of galaxies in the local universe selected from the SDSS (York et al. 2000) survey. We use the data from the SDSS DR8 database (Aihara et al. 2011), cross correlated with an updated version of the multi-scale density catalog from Wilman et al. (2010; with densities computed according to Equation (1); updated DR8 catalog as used by Hirschmann et al. 2014; Phleps et al. 2014). SDSS DR8 includes five-color *ugriz* imaging of 14,555 square degrees. The spectroscopic part of the survey provides redshifts for 77% of objects brighter than a limit of $r = 17.77$ across 8032 square degrees. Our sample is derived from the spectroscopic database. Luminosities are computed by k-correcting and adding the distance modulus to the Petrosian r-band magnitude. k-corrections are performed using the K-CORRECT IDL tool (Blanton & Roweis 2007). We select as primary galaxies those with $M_r < -18$ mag and $0.015 < z < 0.08$. In contrast to the method we use at high redshift, the sample of neighbors (galaxies used to calculate the density in Equation (1)) is restricted to $M_r < -20$ mag. This ensures a volume limited sample for the neighbors in this redshift range, while for the primary galaxies we correct for volume incompleteness using V_{max} corrections. The primary sample numbers $\sim 3 \times 10^5$ galaxies. Stellar masses and star formation rates are obtained from the JHU-MPA[16] catalogs updated to DR7 (Kauffmann et al. 2003; Brinchmann et al. 2004).

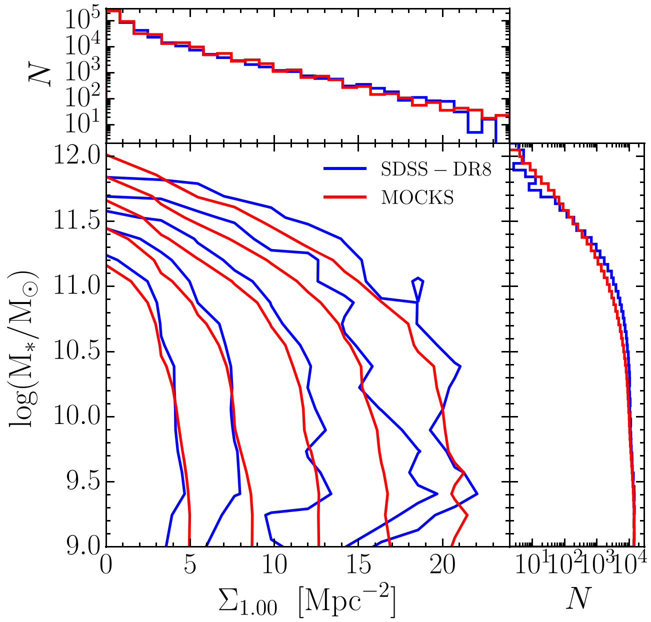

Figure 28. Main panel: bivariate distribution of density on the 1.00 Mpc scale and stellar mass for the SDSS sample (blue) and the mock sample (red). The mock contours have been scaled to account for the ratio of volumes between the simulation box and the data. The contours are logarithmically spaced with the outermost contour at 4 objects per bin and the innermost at 300 objects per bin. Upper panel: marginalized distributions of density on the 1.00 Mpc scale for the SDSS and the mock samples. The counts refer to the SDSS sample, while the mock histogram has been normalized by the ratio of the volumes. Right panel: same as given previously but marginalized over the stellar mass.

For this work, we use the density computed on a fixed scale of 1 Mpc, with a velocity cut of $dv = \pm 1000$ km s^{-1}. This scale is larger than what we use in the 3D-*HST* sample in order to take into account the growth of structure with cosmic time. We stress that our results do not significantly depend on the scale chosen, because the halo mass calibration is performed

---

[16] http://www.mpa-garching.mpg.de/SDSS/DR7/

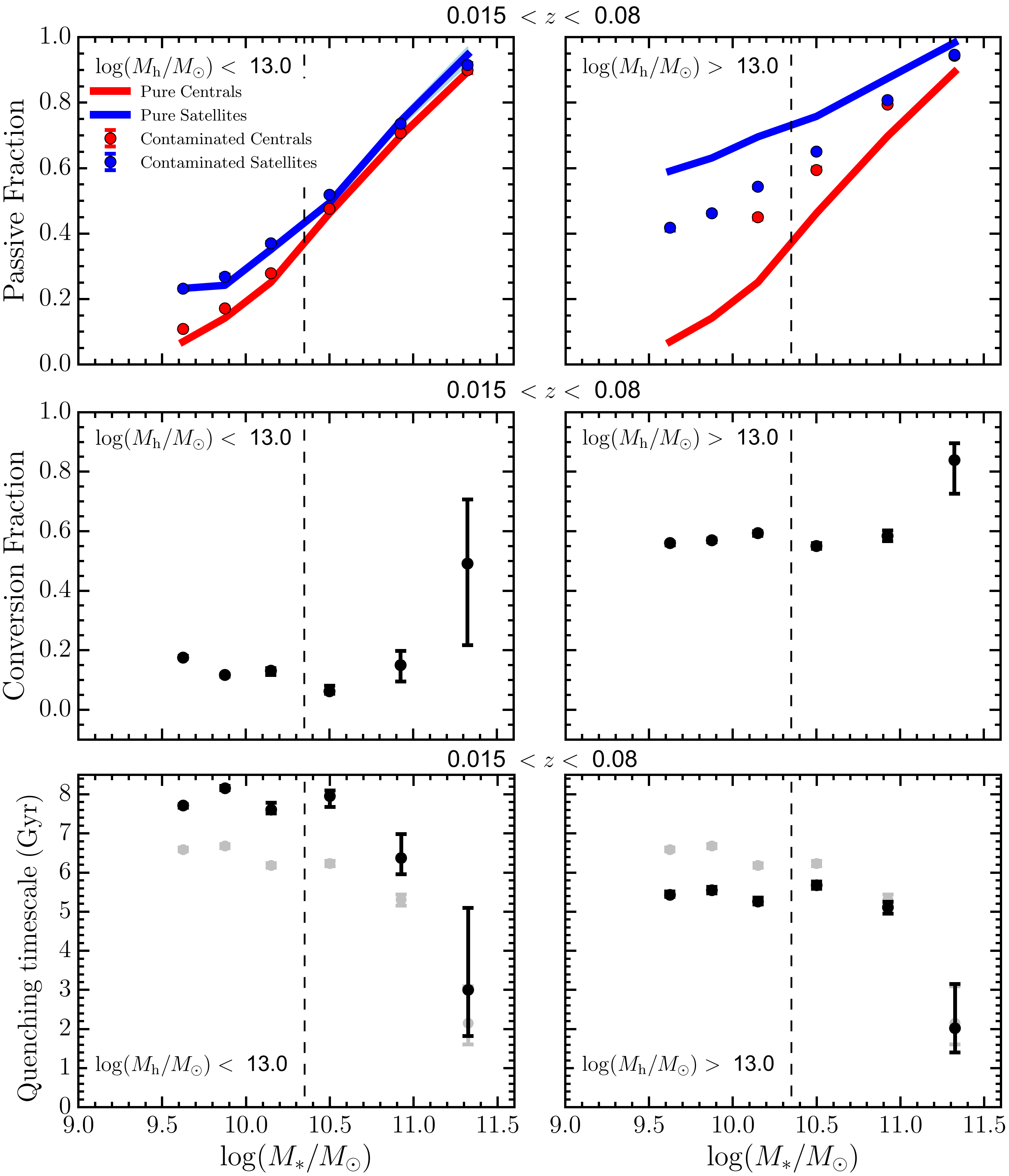

Figure 29. Top panels: passive fraction for central and satellite galaxies in bins of M_* and $M_{\rm halo}$ for the SDSS sample. The median (log) halo masses for satellites are 12.39 and 13.77 for the lower and higher halo mass bin, respectively. Points and lines are color coded as in Figure 17. Middle panels: conversion fractions for satellite galaxies in bins of M_* and M_h obtained from Equation (17) for the SDSS sample. Bottom panels: quenching times for satellite galaxies in bins of M_* and M_h for the SDSS sample.

self consistently and we only compare calibrated quantities across the two samples. We have further computed stellar mass ranks for each primary galaxy in the adaptive aperture, as described in Section 6.1.

One limitation of the SDSS spectroscopic strategy is that not all the spectroscopic targets can be actually observed because two fibers cannot be placed closer than 55″ on the sky, and each patch of the sky is only observed once (although with

Table 2
Example of the Environmental Catalog Table Made Available with this Work

Field (1)	ID (2)	$f_{\rm area,0.75}$ (3)	$\Sigma_{0.75}$ (4)	$\delta_{0.75}$ (5)	$M_{\rm rank}$ (6)	$P_{\rm CEN}$ (7)	$P_{\rm SAT}$ (8)	$M_{h,16\|\rm CEN}$ (9)	$M_{h,50\|\rm CEN}$ (10)	$M_{h,84\|\rm CEN}$ (11)	$M_{h,16\|\rm SAT}$ (12)	$M_{h,50\|\rm SAT}$ (13)	$M_{h,84\|\rm SAT}$ (14)
COSMOS	22162	1.00	3.96	0.984	1	0.911	0.089	11.968	12.195	12.524	12.428	12.753	13.134
UDS	19166	1.00	18.67	7.937	5	0.199	0.801	11.773	11.967	12.398	13.167	14.049	14.251
AEGIS	19285	1.00	2.83	1.077	4	0.544	0.456	11.867	12.087	12.510	12.536	12.917	13.352

small overlaps between adjacent spectroscopic plates). As a result the spectroscopic catalog does not contain all the sources detected in the imaging. Spectroscopic incompleteness is taken into account in the computation of the densities, as described by Wilman et al. (2010), and we further consider it when we match to the mock galaxy sample. Passive galaxies are selected using the specific star formation rate (sSFR) as a tracer. For consistency with previous studies (e.g., Hirschmann et al. 2014), we define passive galaxies as those with sSFR $< 10^{-11}\,{\rm yr}^{-1}$. We note that this corresponds to a $\sim$1 dex offset from the main sequence of star-forming galaxies at $z = 0$, which is consistent with the division of UVJ star-forming from UVJ passive galaxies adopted in Section 7.1.

D.2. The Model Sample

We generate a model galaxy sample that matches the stellar mass and density distributions of the SDSS observational catalog. To do so, we take the SAM from Henriques et al. (2015) at the $z = 0$ snapshot of the Millennium simulation. In this case we do not use light cones but a three-dimensional box because of the large area covered by SDSS and the single redshift bin. Densities are computed by projecting one of the axes of the box into a redshift axis, as described in Fossati et al. (2015). We set an aperture size of 1 Mpc, a velocity cut $dv = \pm 1000\,{\rm km\,s}^{-1}$, and we compute densities according to Equation (1).

The model sample does not suffer from spectroscopic incompleteness; on the other hand, the distribution of r-band magnitudes does not perfectly match the one obtained from the observations. To overcome both those issues at once, we employ a method that iterates on the magnitude limits for the primary and the neighbors samples until the number density and the density distribution of the selected sample match the observational data. Before doing that, we need to derive the total number of photometric galaxies in the SDSS DR8 footprint (more precisely in the area followed up by spectroscopy) that would have been observed if fiber collisions were not a limitation. We query the SDSS database for the number of galaxies in the spectroscopic database and the number of galaxies in the photometric database that would satisfy the criteria for spectroscopic follow-up. The ratio of those values is 0.769. Therefore the number density of mock galaxies needs to be $\rho_{\rm mod} = 1.3 \times \rho_{\rm SDSS,sp}$, where $\rho_{\rm SDSS,sp}$ is the number density of primary galaxies in our observational catalog once we account for $V_{\rm max}$ corrections. The absolute magnitude cuts we set in the models using this iterative method are $M_r < -17.6$ mag and $M_r < -19.0$ mag for the primary and the neighbor samples, respectively. We note that these cuts are up to 1 mag deeper than those used in the SDSS sample. This difference arises in a non-perfect match of the r-band luminosity function, while stellar mass functions are better matched between the SAM and the SDSS data. Figure 28 shows that, with this choice of magnitude limits, both the density and the stellar mass distributions are well matched. This is a critical step to trust our Bayesian approach to halo mass and central/satellite status.

As a last step we assign to each SDSS galaxy (and to model galaxies) a probability that it is central ($P_{\rm cen}$) or satellite ($P_{\rm sat}$) and the halo mass PDFs $P_{M_h|\rm cen}$ and $P_{M_h|\rm sat}$, as described in Section 6.

Figure 29 shows the passive fraction for centrals and satellites, conversion fractions, and satellite quenching timescales derived for the SDSS sample, as described in Sections 7.1, 7.3, and 7.4. Section 7.5 contains the scientific discussion of these results in the context of the evolution of satellite quenching efficiency and timescales from $z = 0$ to $z \sim 2$.

Appendix E
Description of the Environment Catalog for the 3D-*HST* Sample

The environmental properties of 3D-*HST* galaxies are made available at http://dx.doi.org/10.5281/zenodo.168056. Conditional halo mass PDFs given that each galaxy is a central or a satellite and covering the range $10 < \log(M_h/M_\odot) < 15$ with 100 uniform bins are also available as separate tables in the same repository. Table 2 gives an example of the quantities provided in the catalog, and the description of the columns follows:

(1) 3D-*HST* field.

(2) 3D-*HST* photometric ID from Skelton et al. (2014).

(3) Fraction of the 0.75 Mpc aperture in the photometric catalog.

(4) Density of galaxies in an aperture of 0.75 Mpc radius (see Equation (1)).

(5) Overdensity of galaxies in an aperture of 0.75 Mpc radius (see Equation (2)).

(6) Stellar mass rank in the adaptive aperture.

(7) and (8) Probability that the galaxy is a central or a satellite.

(9), (10), and (11) 16th, 50th, and 84th percentile of the log halo mass cumulative PDF, given that the galaxy is a central.

(12), (13), and (14) 16th, 50th, and 84th percentile of the log halo mass cumulative PDF, given that the galaxy is a satellite.

References

Adami, C., Mazure, A., Ilbert, O., et al. 2005, A&A, 443, 805
Aihara, H., Allende Prieto, C., An, D., et al. 2011, ApJS, 193, 29
Arnouts, S., Cristiani, S., Moscardini, L., et al. 1999, MNRAS, 310, 540
Arnouts, S., Vandame, B., Benoist, C., et al. 2001, A&A, 379, 740
Ashby, M. L. N., Willner, S. P., Fazio, G. G., et al. 2013, ApJ, 769, 80
Baldry, I. K., Balogh, M. L., Bower, R. G., et al. 2006, MNRAS, 373, 469
Balogh, M., Eke, V., Miller, C., et al. 2004, MNRAS, 348, 1355
Balogh, M. L., McGee, S. L., Mok, A., et al. 2014, MNRAS, 443, 2679
Balogh, M. L., McGee, S. L., Mok, A., et al. 2016, MNRAS, 456, 4364
Balogh, M. L., Morris, S. L., Yee, H. K. C., Carlberg, R. G., & Ellingson, E. 1997, ApJL, 488, L75
Balogh, M. L., Navarro, J. F., & Morris, S. L. 2000, ApJ, 540, 113
Bell, E. F., Wolf, C., Meisenheimer, K., et al. 2004, ApJ, 608, 752
Bezanson, R., Wake, D. A., Brammer, G. B., et al. 2016, ApJ, 822, 30
Bielby, R., Hudelot, P., McCracken, H. J., et al. 2012, A&A, 545, A23
Blanton, M. R., & Moustakas, J. 2009, ARA&A, 47, 159
Blanton, M. R., & Roweis, S. 2007, AJ, 133, 734
Boselli, A., Boissier, S., Cortese, L., & Gavazzi, G. 2008, ApJ, 674, 742
Boselli, A., Cortese, L., Boquien, M., et al. 2014a, A&A, 564, A66
Boselli, A., Cuillandre, J. C., Fossati, M., et al. 2016, A&A, 587, A68
Boselli, A., & Gavazzi, G. 2006, PASP, 118, 517
Boselli, A., & Gavazzi, G. 2014, A&ARv, 22, 74
Boselli, A., Roehlly, Y., Fossati, M., et al. 2016, A&A, 596, A11
Boselli, A., Voyer, E., Boissier, S., et al. 2014b, A&A, 570, A69
Brammer, G. B., van Dokkum, P. G., & Coppi, P. 2008, ApJ, 686, 1503
Brammer, G. B., van Dokkum, P. G., Franx, M., et al. 2012, ApJS, 200, 13
Brinchmann, J., Charlot, S., White, S. D. M., et al. 2004, MNRAS, 351, 1151
Bruzual, G., & Charlot, S. 2003, MNRAS, 344, 1000
Byrd, G., & Valtonen, M. 1990, ApJ, 350, 89
Calzetti, D., Armus, L., Bohlin, R. C., et al. 2000, ApJ, 533, 682
Cardamone, C. N., van Dokkum, P. G., Urry, C. M., et al. 2010, ApJS, 189, 270
Chabrier, G. 2003, PASP, 115, 763
Conroy, C., Gunn, J. E., & White, M. 2009, ApJ, 699, 486
Cooper, M. C., Newman, J. A., Croton, D. J., et al. 2006, MNRAS, 370, 198
Croton, D. J., Springel, V., White, S. D. M., et al. 2006, MNRAS, 365, 11
Cucciati, O., Granett, B. R., Branchini, E., et al. 2014, A&A, 565, A67
Darvish, B., Mobasher, B., Sobral, D., et al. 2016, arXiv:1605.03182
De Lucia, G., & Blaizot, J. 2007, MNRAS, 375, 2
De Lucia, G., Boylan-Kolchin, M., Benson, A. J., Fontanot, F., & Monaco, P. 2010, MNRAS, 406, 1533
De Lucia, G., Poggianti, B. M., Aragón-Salamanca, A., et al. 2007, MNRAS, 374, 809
De Lucia, G., Weinmann, S., Poggianti, B. M., Aragón-Salamanca, A., & Zaritsky, D. 2012, MNRAS, 423, 1277
Dekel, A., & Birnboim, Y. 2006, MNRAS, 368, 2
Donley, J. L., Koekemoer, A. M., Brusa, M., et al. 2012, ApJ, 748, 142
Dressler, A. 1980, ApJ, 236, 351
Erben, T., Hildebrandt, H., Lerchster, M., et al. 2009, A&A, 493, 1197
Erfanianfar, G., Finoguenov, A., Tanaka, M., et al. 2013, ApJ, 765, 117
Erfanianfar, G., Popesso, P., Finoguenov, A., et al. 2016, MNRAS, 455, 2839
Etherington, J., & Thomas, D. 2015, MNRAS, 451, 660
Finoguenov, A., Guzzo, L., Hasinger, G., et al. 2007, ApJS, 172, 182
Finoguenov, A., Tanaka, M., Cooper, M., et al. 2015, A&A, 576, A130
Finoguenov, A., Watson, M. G., Tanaka, M., et al. 2010, MNRAS, 403, 2063
Fontanot, F., Springel, V., Angulo, R. E., & Henriques, B. 2012, MNRAS, 426, 2335
Fossati, M., Fumagalli, M., Boselli, A., et al. 2016, MNRAS, 455, 2028
Fossati, M., Gavazzi, G., Boselli, A., & Fumagalli, M. 2012, A&A, 544, A128
Fossati, M., Wilman, D. J., Fontanot, F., et al. 2015, MNRAS, 446, 2582
Franx, M., van Dokkum, P. G., Förster Schreiber, N. M., et al. 2008, ApJ, 688, 770
Fumagalli, M., Fossati, M., Hau, G. K. T., et al. 2014, MNRAS, 445, 4335
Furusawa, H., Kosugi, G., Akiyama, M., et al. 2008, ApJS, 176, 1
Gallazzi, A., & Bell, E. F. 2009, ApJS, 185, 253
Gavazzi, G., Boselli, A., Mayer, L., et al. 2001, ApJL, 563, L23
Gavazzi, G., Consolandi, G., Dotti, M., et al. 2015, A&A, 580, A116
Gavazzi, G., Fumagalli, M., Cucciati, O., & Boselli, A. 2010, A&A, 517, A73
Gavazzi, G., Fumagalli, M., Fossati, M., et al. 2013, A&A, 553, A89
Gawiser, E., van Dokkum, P. G., Herrera, D., et al. 2006, ApJS, 162, 1
Geach, J. E., Simpson, C., Rawlings, S., Read, A. M., & Watson, M. 2007, MNRAS, 381, 1369
Genzel, R., Tacconi, L. J., Lutz, D., et al. 2015, ApJ, 800, 20
Gilli, R., Cimatti, A., Daddi, E., et al. 2003, ApJ, 592, 721
Grogin, N. A., Kocevski, D. D., Faber, S. M., et al. 2011, ApJS, 197, 35
Gunn, J. E., & Gott, J. R., III 1972, ApJ, 176, 1
Guo, Q., White, S., Angulo, R. E., et al. 2013a, MNRAS, 428, 1351
Guo, Q., White, S., Boylan-Kolchin, M., et al. 2011, MNRAS, 413, 101
Guo, Y., Ferguson, H. C., Giavalisco, M., et al. 2013b, ApJS, 207, 24
Haas, M. R., Schaye, J., & Jeeson-Daniel, A. 2012, MNRAS, 419, 2133
Haines, C. P., Pereira, M. J., Smith, G. P., et al. 2015, ApJ, 806, 101
Henriques, B. M. B., White, S. D. M., Thomas, P. A., et al. 2015, MNRAS, 451, 2663
Henriques, B. M. B., White, S. D. M., Thomas, P. A., et al. 2016, arXiv:1611.02286
Hirschmann, M., De Lucia, G., Wilman, D., et al. 2014, MNRAS, 444, 2938
Hopkins, P. F., Cox, T. J., Kereš, D., & Hernquist, L. 2008, ApJS, 175, 390
Hsieh, B.-C., Wang, W.-H., Hsieh, C.-C., et al. 2012, ApJS, 203, 23
Hsu, L.-T., Salvato, M., Nandra, K., et al. 2014, ApJ, 796, 60
Ilbert, O., Arnouts, S., McCracken, H. J., et al. 2006, A&A, 457, 841
Ilbert, O., Capak, P., Salvato, M., et al. 2009, ApJ, 690, 1236
Isobe, T., Feigelson, E. D., Akritas, M. G., & Babu, G. J. 1990, ApJ, 364, 104
Kapferer, W., Sluka, C., Schindler, S., Ferrari, C., & Ziegler, B. 2009, A&A, 499, 87
Kauffmann, G., Heckman, T. M., Tremonti, C., et al. 2003, MNRAS, 346, 1055
Kauffmann, G., White, S. D. M., Heckman, T. M., et al. 2004, MNRAS, 353, 713
Kenney, J. D. P., Abramson, A., & Bravo-Alfaro, H. 2015, AJ, 150, 59
Kennicutt, R. C., Jr. 1998a, ARA&A, 36, 189
Kennicutt, R. C., Jr. 1998b, ApJ, 498, 541
Knobel, C., Lilly, S. J., Kovač, K., et al. 2013, ApJ, 769, 24
Kodama, T., Yamada, T., Akiyama, M., et al. 2004, MNRAS, 350, 1005
Koekemoer, A. M., Faber, S. M., Ferguson, H. C., et al. 2011, ApJS, 197, 36
Kovač, K., Lilly, S. J., Cucciati, O., et al. 2010, ApJ, 708, 505
Kovač, K., Lilly, S. J., Knobel, C., et al. 2014, MNRAS, 438, 717
Kriek, M., Shapley, A. E., Reddy, N. A., et al. 2015, ApJS, 218, 15
Kriek, M., van Dokkum, P. G., Labbé, I., et al. 2009, ApJ, 700, 221
Kurk, J., Cimatti, A., Daddi, E., et al. 2013, A&A, 549, A63
Kurk, J., Cimatti, A., Zamorani, G., et al. 2009, A&A, 504, 331
Larson, R. B., Tinsley, B. M., & Caldwell, C. N. 1980, ApJ, 237, 692
Le Fèvre, O., Tasca, L. A. M., Cassata, P., et al. 2015, A&A, 576, A79
Lehmer, B. D., Brandt, W. N., Alexander, D. M., et al. 2005, ApJS, 161, 21
Lilly, S. J., Carollo, C. M., Pipino, A., Renzini, A., & Peng, Y. 2013, ApJ, 772, 119
Lilly, S. J., Le Fèvre, O., Renzini, A., et al. 2007, ApJS, 172, 70
Marchesini, D., van Dokkum, P. G., Förster Schreiber, N. M., et al. 2009, ApJ, 701, 1765
Mastropietro, C., Moore, B., Mayer, L., et al. 2005, MNRAS, 364, 607
McCracken, H. J., Milvang-Jensen, B., Dunlop, J., et al. 2012, A&A, 544, A156
McGee, S. L., Balogh, M. L., Bower, R. G., Font, A. S., & McCarthy, I. G. 2009, MNRAS, 400, 937
McGee, S. L., Bower, R. G., & Balogh, M. L. 2014, MNRAS, 442, L105
McLean, I. S., Steidel, C. C., Epps, H. W., et al. 2012, Proc. SPIE, 8446, 84460J
Mendel, J. T., Saglia, R. P., Bender, R., et al. 2015, ApJL, 804, L4
Mendel, J. T., Simard, L., Palmer, M., Ellison, S. L., & Patton, D. R. 2014, ApJS, 210, 3
Merluzzi, P., Busarello, G., Dopita, M. A., et al. 2013, MNRAS, 429, 1747
Merritt, D. 1983, ApJ, 264, 24
Mok, A., Balogh, M. L., McGee, S. L., et al. 2013, MNRAS, 431, 1090
Mok, A., Balogh, M. L., McGee, S. L., et al. 2014, MNRAS, 438, 3070
Momcheva, I. G., Brammer, G. B., van Dokkum, P. G., et al. 2016, ApJS, 225, 27
Moore, B., Lake, G., & Katz, N. 1998, ApJ, 495, 139
Moy, E., Barmby, P., Rigopoulou, D., et al. 2003, A&A, 403, 493
Muldrew, S. I., Croton, D. J., Skibba, R. A., et al. 2012, MNRAS, 419, 2670
Muzzin, A., Marchesini, D., Stefanon, M., et al. 2013, ApJ, 777, 18
Muzzin, A., van der Burg, R. F. J., McGee, S. L., et al. 2014, ApJ, 796, 65
Muzzin, A., Wilson, G., Yee, H. K. C., et al. 2012, ApJ, 746, 188
Nelson, E. J., van Dokkum, P. G., Förster Schreiber, N. M., et al. 2016, ApJ, 828, 27
Noeske, K. G., Weiner, B. J., Faber, S. M., et al. 2007, ApJL, 660, L43
Oemler, A., Jr. 1974, ApJ, 194, 1
Oke, J. B. 1974, ApJS, 27, 21
Paccagnella, A., Vulcani, B., Poggianti, B. M., et al. 2016, ApJL, 816, L25
Papovich, C., Momcheva, I., Willmer, C. N. A., et al. 2010, ApJ, 716, 1503
Peng, Y.-j., Lilly, S. J., Kovač, K., et al. 2010, ApJ, 721, 193
Peng, Y.-j., Lilly, S. J., Renzini, A., & Carollo, M. 2012, ApJ, 757, 4

Perlmutter, S., Aldering, G., Goldhaber, G., et al. 1999, ApJ, 517, 565
Phleps, S., Wilman, D. J., Zibetti, S., & Budavári, T. 2014, MNRAS, 438, 2233
Planck Collaboration, Ade, P. A. R., Aghanim, N., et al. 2014, A&A, 571, A16
Poggianti, B. M., Bridges, T. J., Komiyama, Y., et al. 2004, ApJ, 601, 197
Quadri, R. F., Williams, R. J., Franx, M., & Hildebrandt, H. 2012, ApJ, 744, 88
Raichoor, A., & Andreon, S. 2012, A&A, 543, 19
Roediger, E., & Hensler, G. 2005, A&A, 433, 875
Rudnick, G., von der Linden, A., Pelló, R., et al. 2009, ApJ, 700, 1559
Saintonge, A., Kauffmann, G., Wang, J., et al. 2011, MNRAS, 415, 61
Salimbeni, S., Castellano, M., Pentericci, L., et al. 2009, A&A, 501, 865
Sanders, D. B., Salvato, M., Aussel, H., et al. 2007, ApJS, 172, 86
Schawinski, K., Urry, C. M., Simmons, B. D., et al. 2014, MNRAS, 440, 889
Schmidt, M. 1959, ApJ, 129, 243
Scoville, N., Aussel, H., Benson, A., et al. 2007, ApJS, 172, 150
Sharples, R., Bender, R., Agudo Berbel, A., et al. 2013, Msngr, 151, 21
Shattow, G. M., Croton, D. J., Skibba, R. A., et al. 2013, MNRAS, 433, 3314
Silk, J., & Rees, M. J. 1998, A&A, 331, L1
Skelton, R. E., Whitaker, K. E., Momcheva, I. G., et al. 2014, ApJS, 214, 24
Solanes, J. M., Manrique, A., García-Gómez, C., et al. 2001, ApJ, 548, 97
Springel, V., White, S. D. M., Jenkins, A., et al. 2005, Natur, 435, 629
Springel, V., White, S. D. M., Tormen, G., & Kauffmann, G. 2001, MNRAS, 328, 726
Sun, M., Donahue, M., & Voit, G. M. 2007, ApJ, 671, 190
Tacconi, L. J., Neri, R., Genzel, R., et al. 2013, ApJ, 768, 74
Tal, T., Dekel, A., Oesch, P., et al. 2014, ApJ, 789, 164
Tanaka, M., Finoguenov, A., & Ueda, Y. 2010, ApJL, 716, L152
Taniguchi, Y., Scoville, N., Murayama, T., et al. 2007, ApJS, 172, 9
Tasca, L. A. M., Le Fevre, O., Ribeiro, B., et al. 2016, arXiv:1602.01842
Taylor, E. N., Franx, M., van Dokkum, P. G., et al. 2009, ApJS, 183, 295
Tonnesen, S., & Bryan, G. L. 2010, ApJ, 709, 1203
Trevese, D., Castellano, M., Fontana, A., & Giallongo, E. 2007, A&A, 463, 853
van den Bosch, F. C., Aquino, D., Yang, X., et al. 2008, MNRAS, 387, 79
van der Burg, R. F. J., Muzzin, A., Hoekstra, H., et al. 2013, A&A, 557, A15
Vollmer, B., Cayatte, V., Balkowski, C., & Duschl, W. J. 2001, ApJ, 561 708
Vollmer, B., Huchtmeier, W., & van Driel, W. 2005, A&A, 439, 921
Wang, J., De Lucia, G., Kitzbichler, M. G., & White, S. D. M. 2008, MNRAS, 384, 1301
Weiner, B. J., Phillips, A. C., Faber, S. M., et al. 2005, ApJ, 620, 595
Wetzel, A. R., Tinker, J. L., & Conroy, C. 2012, MNRAS, 424, 232
Wetzel, A. R., Tinker, J. L., Conroy, C., & van den Bosch, F. C. 2013, MNRAS, 432, 336
Whitaker, K. E., Franx, M., Leja, J., et al. 2014, ApJ, 795, 104
Whitaker, K. E., Labbé, I., van Dokkum, P. G., et al. 2011, ApJ, 735, 86
White, S. D. M., & Frenk, C. S. 1991, ApJ, 379, 52
White, S. D. M., & Rees, M. J. 1978, MNRAS, 183, 341
Williams, R. J., Quadri, R. F., Franx, M., van Dokkum, P., & Labbé, I. 2009, ApJ, 691, 1879
Wilman, D. J., Balogh, M. L., Bower, R. G., et al. 2005, MNRAS, 358, 71
Wilman, D. J., Zibetti, S., & Budavári, T. 2010, MNRAS, 406, 1701
Wisnioski, E., Förster Schreiber, N. M., Wuyts, S., et al. 2015, ApJ, 799, 209
Yagi, M., Yoshida, M., Komiyama, Y., et al. 2010, AJ, 140, 1814
York, D. G., Adelman, J., Anderson, J. E., Jr., et al. 2000, AJ, 120, 1579